Radiative transitions in InGaN quantum-well structures

by

Noad Asaf Shapiro

B.S. (University of California, Berkeley) 1997
M.S. (University of California, Berkeley) 2000

A dissertation submitted in partial satisfaction of the

requirements for the degree of

Doctor of Philosophy
in

Engineering - Materials Science and Mineral Engineering

in the

GRADUATE DIVISION

of the

UNIVERSITY OF CALIFORNIA, BERKELEY

Committee in charge:

Professor Eicke R. Weber, Chair
Professor Eugene E. Haller
Professor Peter Yu

Fall 2002

Radiative transitions in InGaN
quantum-well structures

Copyright (2002)

by

Noad Asaf Shapiro

Abstract

Radiative transitions in InGaN quantum-well structures

by

Noad Asaf Shapiro

Doctor of Philosophy in

Engineering - Materials Science and Mineral Engineering

University of California, Berkeley

Professor Eicke R. Weber, Chair

InGaN based light emitting devices demonstrate excellent luminescence properties and have great potential in lighting applications. Though these devices are already being produced on an industrial scale, the nature of their radiative transition is still not well understood. In particular, the role of the huge (>1MV/cm), built-in electric field in these transitions is still under debate. The luminescence characteristics of InGaN quantum well structures were investigated as a function of excitation power, temperature, and biaxial strain, with an intent of discerning the effects of the electric field and inhomogenous indium distribution in the QW on the radiative transition.

It was found that the luminescence energy did not scale only with the indium concentration but that the QW thickness must also be taken into account. The thickness affects the transition energy due to quantum confinement and carrier separation across a potential drop in the QW. The luminescence peak width was shown to increase with increased indium fraction, due to increased indium inhomogeneity. The carrier lifetime

increased exponentially with QW thickness and luminescence wavelength, due to increased carrier separation.

Measuring the luminescence energy and carrier lifetime as a function of excitation density showed that the electric field can be screened by strong excitation and, as a consequence, the carrier separation reduced. The temperature dependence of the luminescence showed evidence for bandtails in the density of states, a phenomenon that has been previously related to transition in indium-rich nano-clusters, yet could be accounted for by fluctuations in other parameters that affect the transition energy. Room temperature luminescence efficiency was shown to weakly decrease with increased QW thickness.

The application of biaxial strain resulted in either a redshift or blueshift of the luminescence, depending on the sample. The direction and magnitude of the shift in luminescence energy is interpreted in terms of a newly introduced parameter L_r, which can be regarded as the effective separation of electrons and holes participating in the luminescence transition. Strong carrier separation due to the built-in electric field usually results in a blueshift and L_r close to the QW width, L_w, whereas weak carrier separation usually can be a redshift. The carrier lifetime decreases with applied strain, indicating a reduction of the effective electron-hole (e-h) separation achieved by the strain-induced field-reduction in the well.

This method is used to evaluate the effective e-h separation in several structures with varying QW thickness, indium concentration, and doping. L_r increases with QW thickness, decreases with indium content, and decreases with heavy doping in the active region. The decrease associated with indium content might be due either to an increase

2

of "carrier trapping" in indium-rich nano-clusters or to an effective reduction of the QW thickness due to interface diffusion. The decrease of L_r associated with heavy doping is probably due to quenching of the electric field by the free carriers.

The results also show that despite the reduced radiative transition rate associated with the carrier separation, the structures still exhibit efficient luminescence behavior and a low non-radiative recombination rate. This suggests that while the carriers are separated along the direction of the electric field, they are localized in the perpendicular direction such that they are not interacting with non-radiative centers associated with the high density of threading dislocations in the structure.

Table of Contents

Acknowledgments

I appreciate greatly the support given to me by my family during this time, especially my grandparents and parents who encouraged me to continue in my education. My friends were also instrumental in keeping me sane during this time, and I would like to thank them for their prayers and unconditional love. To my beloved wife, Sharyn, I cannot thank enough. Without her support, I would have been hard pressed to get much done. I love you, and hope that you are proud of my accomplishments.

Finally, I would like to thank Him who made me and gave me all that I have, and who has redeemed me unto Himself by His grace and His love.

Chapter 1: Introduction

1.1 Introduction to InGaN QW structures

In the past few decades, the world has seen an astonishing emergence in the importance of semiconductor materials. Their most important impact has been felt in the electronic industry where semiconductor transistors have been used to miniaturize electronic circuits by several orders of magnitude. But their contribution to electronic circuits is only one of the many applications of semiconductors. Among these applications are the Light Emitting Diode (LED) and the Laser Diode (LD). These are devices that convert electrical power into light at high efficiency. LEDs are commonly used in visual displays anywhere from phones to huge billboards. They have been used lately to replace traffic signals, and may soon be used to replace the common light bulb. LDs on the other hand are used in memory storage applications such as DVDs and for image definition in printers.

The III-nitrides are a new and exciting class of semiconductors to be used in science and technology. Its members are AlN, GaN, InN, and any alloy composed of the mix: (In, Ga, Al)N. The great interest in the III-Nitride system stems from the possibility of engineering an alloy with a band gap anywhere from more than 6 eV (AlN) to less than 1 eV (InN). This range spans from the near infrared to the near ultraviolet region. The lattice parameters and energy gaps of AlN, GaN and InN are shown in Figure 1. Another advantage of all alloys of the III-nitride system is that they have a direct band gap. This means that electrons at the minimum of the conduction band and holes at the maximum of the valence band have the same crystal momentum. This allows for an

efficient, direct radiative transition process to occur. Since the III-N system has a direct band gap the magnitude of which can be varied greatly through changing the concentration of Al, Ga, and In, it forms an ideal system for LED and LD devices.

$In_xGa_{1-x}N$ has emerged in the past few years as the most important material for short-wavelength optoelectronics. The successful application of this material in the active layers of LEDs and LDs[1] demonstrated convincingly the enormous potential of the group III-nitrides. A schematic of an LED device based on an $In_xGa_{1-x}N$ quantum well is shown in Figure 2. Devices based on this material are already available on the open market, yet the nature of the radiative transitions that occur in these devices is still under debate[2]. Luminescence properties that still require a consistent explanation are: efficient luminescence in the presence of high dislocation density[1], the very large Stokes shift between the energy gap and the emission energy[3], the strong dependence of the emission energy on the excitation power[4], and its anomalous temperature[5] and pressure[6,7] dependencies. Some devices exhibit a number of these luminescence characteristics while others do not. These characteristics cannot be explained within the framework of standard interband transitions. In order to explain these unusual properties, it is necessary to consider the unusual material properties of the InGaN system.

1.2 Material issues related to the radiative transition

1.2.1 Indium segregation

It has been predicted theoretically[8], and demonstrated experimentally[9] that InN and GaN are not completely soluble in one another, even at the highest thin film growth temperatures. Figure 3 shows the miscibility gap between GaN and InN. Therefore, if a

quantum well contains indium at concentrations greater than this solubility limit, phase

separation is likely to ensue. In Figure 4, a high-resolution transmission electron

microscope (HR-TEM) generated image shows indium inhomogeneity in an InGaN

double QW structure.[10] So far, the extent of phase separation is still under debate. While

some believe that the separation is so complete that the resulting precipitates are almost

pure InN[11], HR-TEM experiments usually show only moderate spatial fluctuation of the

indium concentration, of a size comparable to the thickness of the quantum well.[12] Either

way, it is probable that at least some spontaneous redistribution of indium in the layer

occurs during or after the growth in layers with indium fractions greater than 0.1-0.2. To

avoid giving the image of pure indium quantum dots, we generally refer to the regions of

higher indium content as "indium-rich nano-clusters."

1.2.2 Strong polarization

Another peculiarity in this material system results from the polar axis of the

wurtzite crystal structure and the strong polarity of the III-N bonds. All group-III nitrides

in the wurtzite phase have strong spontaneous macroscopic polarization and large

piezoelectric coefficients. This has been found from *ab initio* calculations,[13,14] and is

consistent with much experimental work. The importance of this polarization to the

radiative transition stems from the large, polarization induced electric fields present in the

QW.

The conservation of the dielectric displacement field (*D*) perpendicular to the

interface between the barrier and well requires that

$$\vec{D}_w = \varepsilon_0 E_w + P_w(E_w) = \varepsilon_0 E_b + P_b(E_b) = \vec{D}_b \,, \qquad (1.1)$$

where ε_0 is the permittivity of free space, E_w (E_b) is the electric field in the well (barrier), and P_w (P_b) is the polarization in the well (barrier). The overall polarization is the sum of the zero field polarization and the response of the polarization to the electric field.

$$P(E) = P_0 + \varepsilon_0 \chi E , \tag{1.2}$$

where

$$P_0 = P^{sp} + P^{pz} , \tag{1.3}$$

where P^{sp} and P^{pz} are the spontaneous and piezoelectric polarizations, respectively, and χ is the dielectric susceptibility of the material. Substituting $\varepsilon = 1 + \chi$ into equation (1), we arrive at,

$$\varepsilon_0 \varepsilon_w E_w - \varepsilon_0 \varepsilon_b E_b = P_b - P_w , \tag{1.4}$$

where ε_w (ε_b) is the well (barrier) dielectric constant, and P_w (P_b) now represents the zero field polarization.

For a periodic superlattice, the boundary condition is commonly taken to be such that the potential drop across one period is equal to zero. That is,

$$L_w E_w + L_b E_b = 0 . \tag{1.5}$$

One argument for this assumption is that in the case of an infinite number of periods, a finite potential drop across one period results in nonphysical drop across the structure. Another argument is that during growth, impurity or defect charges are likely to distribute in such a way as to cancel the overall potential drop in the structure. Finally, even if the potential drop is not identically zero, the assumption is still valid in the limit in which the electric field across the whole structure is negligible with respect to the internal fields induced by the polarization.[15] Solving equations (4) and (5) leads to,

4

$$E_w = \frac{L_b(P_b - P_w)}{\varepsilon_0\varepsilon_b L_w + \varepsilon_0\varepsilon_w L_b}.$$ (1.6)

While this equation should hold true for any superlattice structure, it plays an especially important role in the group-III nitrides because of their large spontaneous polarizations and piezoelectric coefficients. Using the material constants shown in Table 1, we plot the electric field in the QW of a typical InGaN QW structure with L_w and L_b equal to 3nm and 10nm, respectively, as a function of indium content in the QW. This plot is shown in Figure 5. We use a linear interpolation between the material constants of GaN and InN is this calculation. The non-linearity arises from the change in the dielectric constant of the quantum well. From Figure 5 we see that that for a typical device, with an indium content of 10-20%, the expected electric field is more than 1MV/cm.

1.3 Radiative transition models

Figure 6 illustrates two distinct radiative transition models that have been suggested to explain the anomalous luminescence properties observed in InGaN structures. Figure 6a is based on the formation of indium-rich nano-clusters[16], while Fig. 6b is based on the presence of the large electric field in the quantum well.[17]

1.3.1 Carrier localization in indium-rich nano-clusters

As pointed out earlier, the miscibility gap between InN and GaN leads to the formation of indium-rich nano-clusters in the InGaN QW. The energy gap of an InGaN alloy is usually described by

$$E_g^{InGaN}(x) = (1-x)\cdot E_g^{GaN} + x\cdot E_g^{InN} - b\cdot x\cdot(1-x),$$ (1.7)

5

where *b* is the bowing parameter and *x* is the fraction of the group III metal sites in the crystal occupied by indium atoms. Since the energy gap for InN is smaller than that of GaN (and b is positive), the energy gap of the InGaN alloy decreases with increasing indium concentration. Thus the indium-rich nano-clusters will appear as potential minima for the electrons in the conduction band and holes in the valence band. If these potential minima are deep enough, the electrons and holes will be trapped inside, and the resulting transition will resemble that shown in Fig. 6a.

This transition has been proposed as an explanation for many of the anomalous luminescence properties of InGaN. If the carriers are localized in these potential minima, they are protected from the non-radiative recombination centers (such as dislocations). This would help to explain the efficient luminescence observed in these devices in the presence of very high densities ($\sim 10^{10}$cm^{-3}) of threading dislocations. O'Donnell et al[18] explained the trend of increasing Stokes shift with increasing indium content in these structures by assuming clusters consisting of almost pure InN but varying in size. Perlin et al[6] proposed that the indium-rich nano-clusters form cubic inclusions to explain the anomalous pressure dependence observed in these devices. Shan et al[19] used the to localization of carriers in indium-rich nano-clusters to explained the relationship between the FWHM of the Photoreflectance (PR) and the FWHM of the Photoluminescence (PL) of InGaN epilayers.

1.3.2 Carrier separation induced by the electric field

The strong electric field resulting from the polarization of this structure has also been looked upon as the culprit behind the unusual luminescence properties of InGaN QW structures. In the presence of an electric field, the electrons and holes are pulled in

opposite directions. This leads to a spatial separation of the electron and hole wavefunctions in the QW. In the illustration depicted in Fig. 6b, the electrons would gravitate towards the right hand surface of the QW, whereas the holes would gravitate to the left. This results in a smaller overlap of the electron and hole wave functions, and so it reduces the probability of radiative recombination. A close look at Fig. 6b will reveal that the separation energy between the electrons (right side of QW) and holes (left side of QW) is reduced as compared to the energy gap. Thus the energy released in the radiative transition is reduced and the luminescence redshifts correspondingly.

This redshift of the luminescence as compared to the energy gap provides an alternate explanation for the large stokes shift in InGaN QW structures.[20] In addition, this transition model provides the best explanation for experiments showing an increased redshift of the luminescence and prolonged radiative lifetime with increasing well thickness.[21]

1.4 Purpose

The purpose of this work is to achieve a better understanding of the nature of the radiative transitions in InGaN QW structures. Both the "carrier localization" model and the "carrier separation" model may have some validity in this material system. Therefore, it is necessary to develop tools that discern which model plays a dominant role in a given device. For this purpose, Electroluminescence (EL), Photoluminescence (PL), and Time-Resolved Photoluminescence (TRPL) of InGaN QW structures are measured as a function of temperature, excitation density, and biaxial strain. The results are compared to expectations based on the two transition models in order to determine which model describes the transition in a given device. Finally, these tools are used to relate the

dominating transition type to structural device parameters, such as QW thickness and indium content.

The understanding of the basic transition mechanisms and their relation to certain structural properties allows the engineering of better devices. It is the hope of the author that the developed characterization tools, together with the improved understanding of the transition mechanism, will guide the design and processing of superior group-III nitride LEDs.
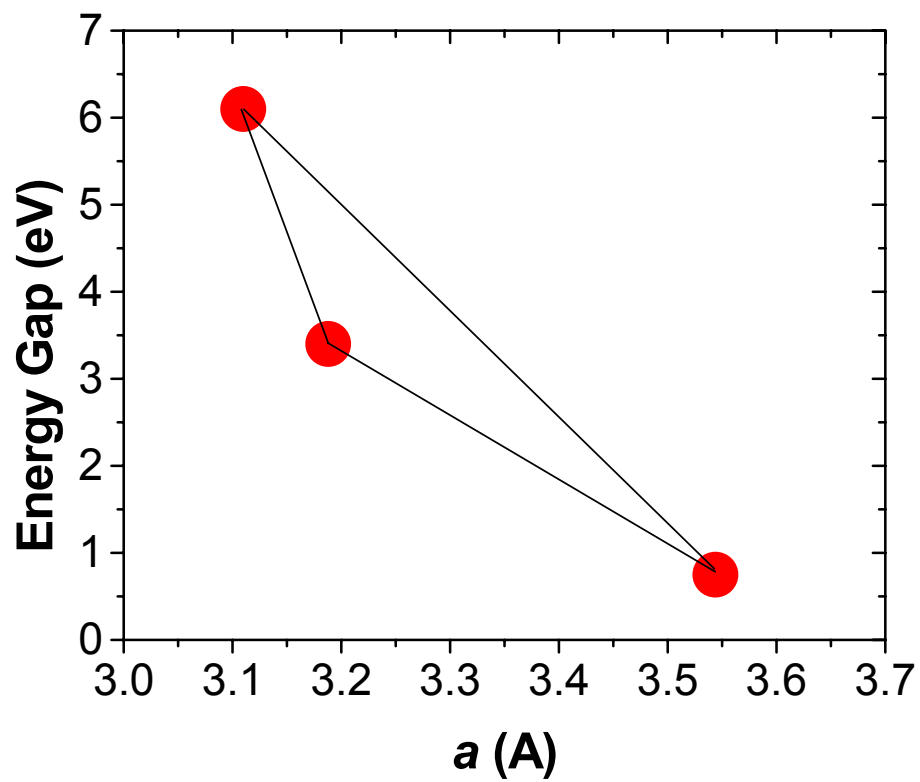
Figure 1: The *a*-lattice parameters and energy gaps of wurtzite AlN, GaN, and InN.

p-electrode

n-electrode

0.15 μm p-GaN $\longrightarrow$

60 nm p-Al$_{0.2}$Ga$_{0.8}$N $\longrightarrow$

3 nm In$_{0.45}$Ga$_{0.55}$N $\longrightarrow$
(Active Layer)

5 μm n-GaN $\longleftarrow$

30 nm GaN buffer layer $\longleftarrow$

Sapphire Substrate
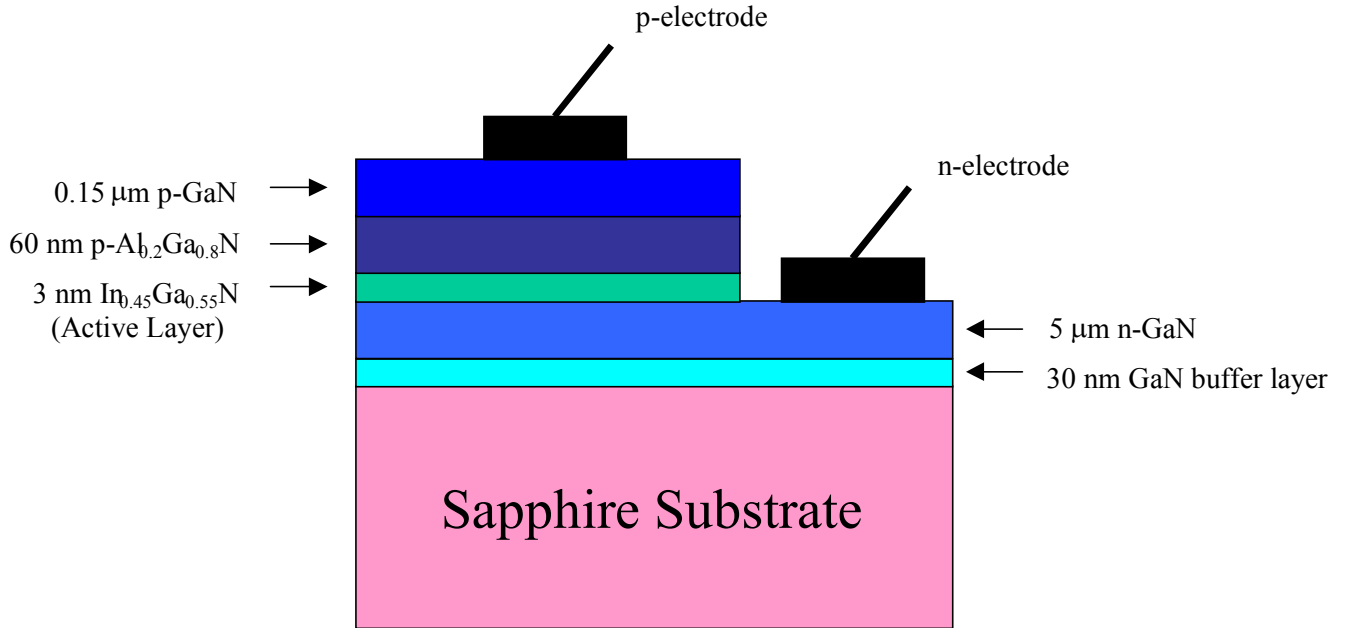
Figure 2: Schematic of an LED based on an In$_x$Ga$_{1-x}$N quantum well[22]. The 3nm InGaN active layer is surrounded on the top by p-type layers for the injection of holes, on the bottom by n-type layers for injection of electrons. As the sapphire substrate is insulating, both contacts have to be formed from the top. A GaN buffer layer grown at low temperature is necessary for improved structural quality due to significant material differences between GaN and Sapphire. The AlGaN layer is used for enhanced carrier confinement.
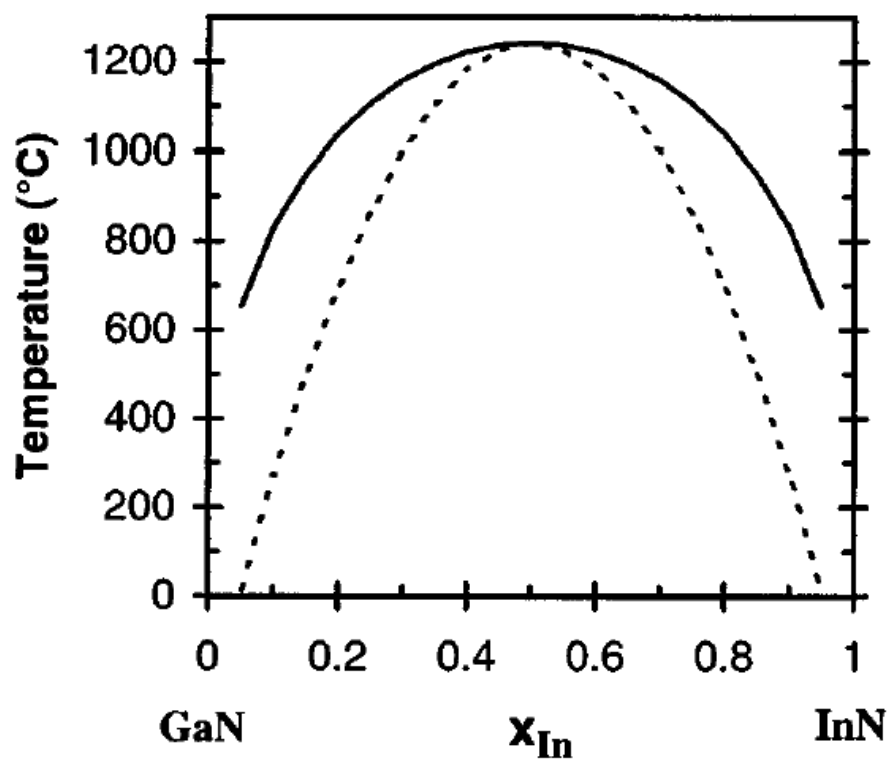
Figure 3: Theoretical miscibility gap between GaN and InN.[8]
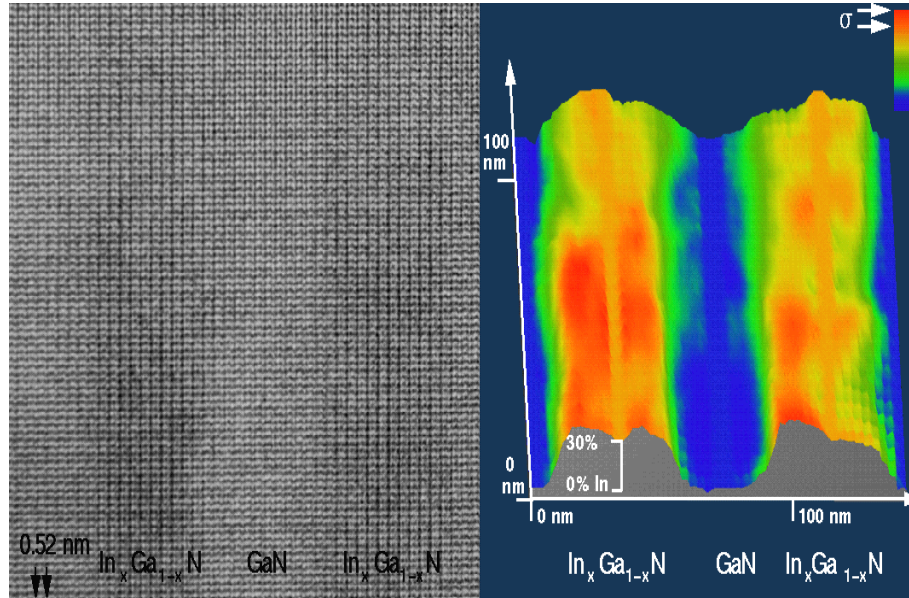
Figure 4: HR-TEM image showing indium inhomogeneity in an InGaN/GaN double heterostructure. On the left is the lattice image, and on the right is the concentration of indium as determined from quantitative analysis of the image on the left.[10]
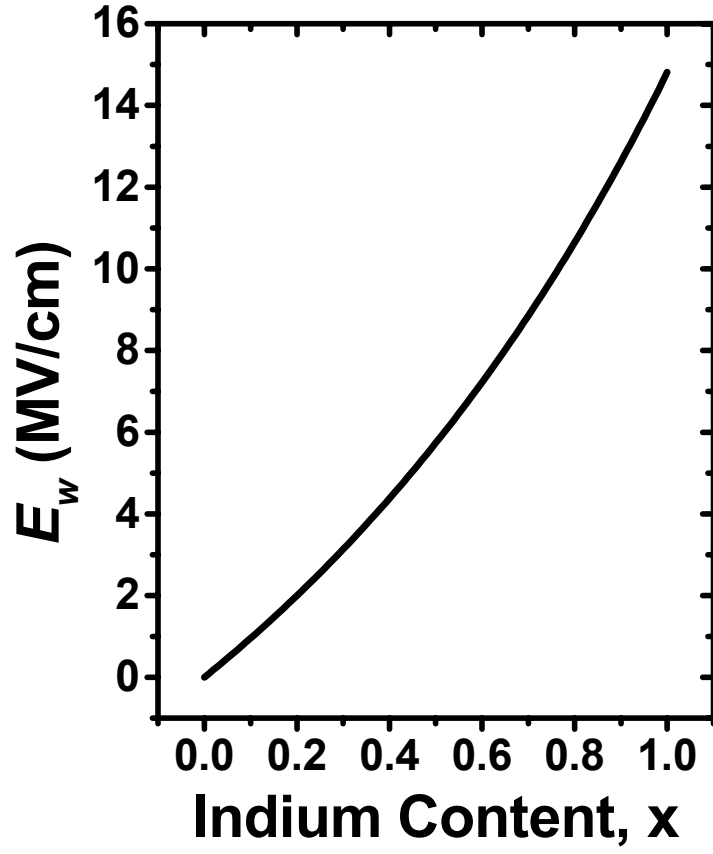
Figure 5: the electric field in the QW of a typical InGaN QW structure with L_w and L_b equal to 3nm and 10nm, respectively, as a function of indium content in the QW.

(a)   (b)
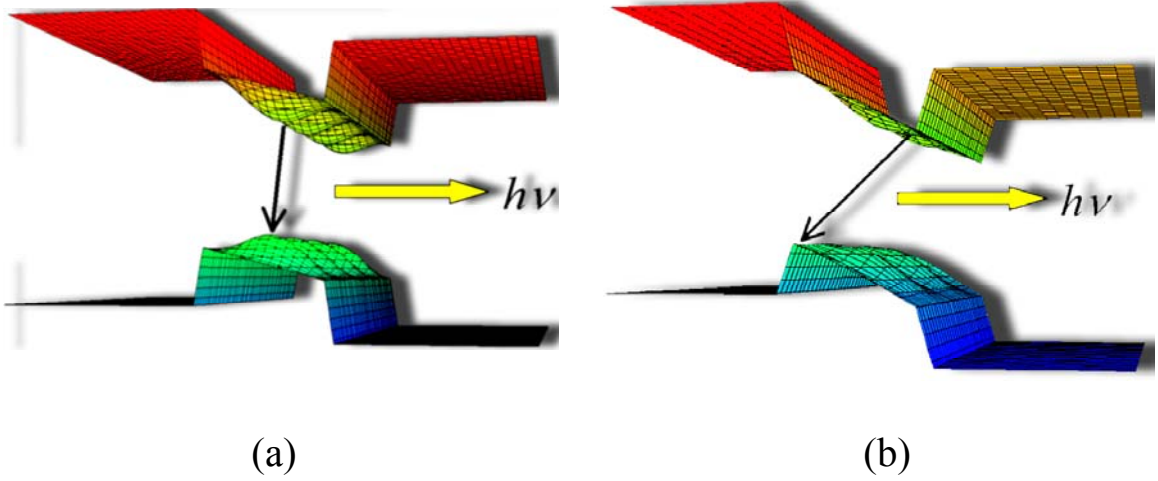
Figure 6: Possible transitions in InGaN/GaN QW structures. (a) Transition between carriers localized in indium-rich nano-clusters. (b) Transition between carriers separated across the QW by an electric field.

1.6 Tables

Table I: Properties of GaN and InN

Property:	GaN	InN
a-lattice parameter (A)	3.188	3.544
c-lattice parameter (A)	5.185	5.718
C_{11}(Gpa)[23]	390	
C_{12}(Gpa)[23]	145	
C_{13}(Gpa)[23]	106	
C_{33}(Gpa)[23]	398	
C_{44}(Gpa)[23]	105	
C_{66}(Gpa)[23]	123	
S_{11}(Gpa^{-1})[23]	3.09×10^{-3}	
S_{12}(GPa^{-1})[23]	-9.96×10^{-4}	
S_{13}(GPa^{-1})[23]	-5.67×10^{-4}	
S_{33}(GPa^{-1})[23]	2.81×10^{-4}	
S_{44}(GPa^{-1})[23]	9.52×10^{-3}	
S_{66}(GPa^{-1})[23]	8.13×10^{-3}	
e_{13} (C/m^2)[24]	-0.34	-0.41
e_{33} (C/m^2)[24]	0.67	0.81
P_{sp} (C/cm^2)[24]	-0.034	-0.042
a_{cz}-D_1 (eV)[25]	-8.16	
a_{ct}-D_2 (eV)[25]	-8.16	
D_3 (eV)[25]	-1.44	
D_4 (eV)[25]	0.72	
E_g (eV)	3.39[26]	~0.8[27,28]
β (K)[29]	770	
γ (eV/K)[29]	9.4×10^{-4}	
a_λ^{E2} (cm^{-1})[30]	-818	
b_λ^{E2} (cm^{-1})[30]	-797	
ε^{31}	10.28	14.61

1.7 References

[1] S. Nakamura and G. Fasol, *The Blue Laser Diode* (Springer, Berlin, 1997).

[2] S.J. Pearton, J.C. Zolper, R.J. Shul and F. Ren, Appl. Phys. Rev. **86**, 1 (1998).

[3] R.W. Martin, P.G. Middleton and K.P. O'Donnell, Appl. Phys. Lett. **74**, 263 (1999).

[4] P. Perlin, C. Kisielowski, V. Iota, B.A. Weinstein, L. Mattos, N.A. Shapiro, J. Krueger, E.R. Weber, J. Yang, Appl. Phys. Lett. 73 , 2778 (1998).

[5] P.G. Eliseev, P. Perlin, Lee Jinhyun and M. Osinski, Appl. Phys. Lett. **71**, 569 (1997).

[6] P. Perlin, V. Iota, B.A. Weinstein, P. Wisniewski, T. Suski, P.G. Eliseev, and M. Osinski, Appl. Phys. Lett. 70, 2993 (1997).

[7] W. Shan, J.W. Ager III, W. Walukiewicz, E.E. Haller, M.D. McCluskey, N.M Johnson and D.P. Bour, Phys. Rev. B. **58**, 10191 (1998).

[8] I. Ho and G.B. Stringfellow, Appl. Phys. Lett. **69**, 2701 (1996).

[9] L.T. Romano, M.D. McCluskey, B.S. Krusor, D.P. Bour, C. Chua, S. Brennan and K.M. Yu, J. of Crystal Growth **189/190**, 33 (1998).

[10] C. Kisielowski, Semiconductors and Semimetals **57** (1999).

[11] K.P. O'Donnell, R.W. Martin and P.G. Middleton, Phys. Rev. Lett. **82**, 237 (1999).

[12] C. Kisielowski, Z. Liliental-Weber and S. Nakamura, Jpn. J. Appl. Phys. **36**, 6932 (1997).

[13] F. Bernardini, V. Fiorentini, and D. Vanderbilt, Phys. Rev. B **56**, R10024 (1997).

[14] K. Shimada, T. Sota, and K. Suzuki, J. Appl. Phys. **84**, 4951 (1998).

[15] V. Fiorentini, F. Bernardini, F. D. Sala, A. D. Carlo, and P. Lugli, Phys. Rev. B **60**, 8849 (1999)

[16] Y. Narukawa, Y. Kawakami, S. Fujita and S. Fujita, Phys. Rev. B **55,** R1938 (1996).

[17] T. Takeuchi, S. Sota, M. Katsuragawa, M. Komori, H. Takeuchi, H. Amano and I. Akasaki, Jpn. J. Appl. Phys **36**, L382 (1997).

[18] K. P. O'Donnell, R. W. Martin, and P.G. Middleton, Phys. Rev. Lett. **82**, 237 (1999).

[19] W. Shan, W. Walukiewicz, E.E. Haller, B.D. Little, J.J. Song, M.D. McCluskey, N.M. Johnson, Z.C. Feng, M. Schuman and R.A. Stall, J. Appl. Phys. **84**, 4452, (1998).

[20] E. Berkowicz, D. Gershoni, G. Bahir, E. Lakin, D. Shilo, E. Zolotoyabko, A. C. Abare, S. P. Denbaars, and L. A. Colden, Phys. Rev. B **61**, 10994 (2000).

[21] A. Hangleiter, J. Seo Im, H. Kollmer, S. Heppel, J. Off, Ferdinand Scholz, MRS Internet J. Nitride Semicond. Res. 3, 15 (1998).

[22] T. Mukai, M. Yamada and S. Nakamura, Jpn. J. Appl. Phys. **38**, 3977 (1999).

[23] A. Polian, M. Grimsditch and I. Grzegory, J. Appl. Phys. **79**, 3343 (1996).

[24] A. Zoroddu, F. Bernardini, P. Ruggerone, and V. Fiorentini, Phys. Rev. B **64**, 045208 (2001).

[25] M. Tchounkeu, O. Briot, B. Gil, J.P. Alexis and R.L. Aulombard, J. Appl. Phys. **80**, 5352 (1996).

[26] B. Monemar, Phys. Rev. B **10**, 676 (1974).

[27] V. Yu. Davydov, A. A. Klochikhin, R. P. Seisyan and V. V. Emtsev, et. al., phys. stat. sol. (**b**), **229**, R1 (2002)

[28] J. Wu, W. Walukiewicz, K.M. Yu, J.W. Ager III, E.E. Haller, Hai Lu, William J. Schaff, Yoshiki Saito and Yasushi Nanishi, Appl. Phys. Lett., ID 015222APL, in press.

[29] H. Teisseyre, P. Perlin, T. Suski, I. Grzegory, S. Porowski and J. Jun, J. Appl. Phys. **76**, 2429 (1994).

[30] F. Demangeot, J. Frandon, M. A. Renucci, O. Briot, B. Gil, and R. L. Aulombard, Solid State Commun. **100**, 207 (1996).

[31] F. Bernardini, V. Fiorentini, and D. Vanderbilt, Phys. Rev. Lett. **79**, 3958 (1997).

Chapter 2: Samples and experimental techniques

2.1. Measuring luminescence

In order to study radiative transitions in InGaN QW structures, we make use of the luminescence observed from these structures. In particular, we use Electroluminescence (EL), Photoluminescence (PL), and Time-Resolved Photoluminescence (TRPL). All of these techniques are based on the following principles. First, some excitation mechanism is used to introduce excess electrons and holes into the conduction and valence bands, respectively. Since the electrons and holes naturally seek their lowest state of energy, they will return to their band extrema followed by some electron-hole recombination process that is energetically accessible and quantum mechanically allowed. If this process involves a radiative transition, a photon will be emitted. Then, some detection mechanism is used to detect and characterize this resulting luminescence.

2.1.1 Electroluminescence

In EL, we use the contacts on the LED structure (see Chapter 1, Fig. 1) to inject current directly into the device, thus feeding the conduction band with electrons and the valence band with holes. This experiment is only possible for samples that have an LED structure with contacts. The luminescence is then detected and analyzed by using a double grating, 0.85m Spex 1404 spectrometer with a GaAs photomultiplier. The resulting spectrum for a green Nichia LED is shown in Figure 1.

2.1.2 Photoluminescence

In PL, the 325-nm line of a He-Cd laser with 5-25mW power, focused onto a spot of about 30μm in diameter, is used to excite the photoluminescence. Electrons in the valence band absorb the incoming photons and are excited into the conduction band, leaving a hole in the valence band. They then relax via phonon scattering to their respective band minima and from there they recombine, emitting a photon. The luminescence photons are then analyzed and detected by using a double grating, 0.85m Spex 1404 spectrometer with a GaAs photomultiplier (same as EL). The resulting spectrum for another Nichia green LED is shown in Figure 2.

2.1.3 Time-resolved photoluminescence

TRPL is similar to PL in that a laser beam is used to excite electrons from the valence band to the conduction band. However, since the main purpose of the experiment is to study the time decay of the luminescence, a very short pulse must be used. In our setup, a 150fs pulse from a frequency-tripled mode-locked Ti:sapphire laser is used as the excitation source. The resulting luminescence was analyzed with a picosecond-resolution streak camera, enabling a simultaneous analysis of the emission spectrum and time decay. Figure 3 shows the results of a TRPL measurement of a LumiLeds LED structure. Figure 3(a) is the image obtained from the streak camera. Figure 3(b) shows the average decay of luminescence across the spectrum, and Figure 3(c) shows the average spectrum across the decay.

2.2 Luminescence as a function of system parameters

While the luminescence spectrum generated by the above methods yields interesting

information about the radiative transition in InGaN QW structures, it is even more

informative to study the luminescence response to changing system parameters, that is,

changing the environment where the transition is taking place. In this work, we study the

luminescence response to changes in the excitation density, temperature, and strain level

in the sample.

2.2.1 Excitation density

Changing the excitation density produces a change in the carrier concentration in the

region where the radiative transition takes place. This can cause interesting effects,

especially in the presence of large electric fields. The excitation density can be changed

in various ways, depending on the excitation source. In EL, one can change the current

entering the LED by using a current source. In our experiment we used a Keithley

Instruments 225 Current Source for this purpose. In PL this can be done in two ways. In

some systems, it is possible to control the laser power in a convenient way. This was true

in the TRPL set-up we used, where the internal alignment of the doubler or tripler

crystals had a strong effect on the power of the frequency-tripled beam, without affecting

the position of the laser significantly. A Coherent LaserMate-1 was used to measure the

incident power of the laser. The other way of controlling the incident power is to use

neutral density filters to reduce the beam power. Since the neutral density filters can be

calibrated independently, it is possible to go to laser powers below the sensitivity of the

power-meter. To find the excitation density, we divide the incident laser power by the

area of the laser spot on the sample. Using a laser power of up to 25 mW focused on a

spot 30μm in diameter, we can achieve the excitation densities from ~ 3kW/cm^2 to less than 1W/cm^2.

2.2.2 Temperature

There are two methods of varying the temperature. Most commonly the sample to be studied is placed inside a cryostat. Then, liquid nitrogen or liquid helium is added to the cryostat to lower the temperature to 77K or 4K, respectively. If the sample is attached to a heater, the temperature can be increased from there. In our set-up, the sample is attached by silver paste to the cold head of a closed-circuit helium cryostat where the temperature can be varied between 10K and 300K. In the case of EL, the LED device was de-capsulated and attached with directly to the cold-head of the cryostat to allow for the best possible thermal contact. Since the glue is not strong enough to strain the Sapphire substrate, the difference in thermal expansion coefficients does not result in mechanical strain. Nichia Chemicals provided additional special LEDs that were not encapsulated but bonded to a metallic holder to achieve a good thermal contact.

2.2.3 Biaxial Strain

The experimental apparatus was based on an earlier work by Trzeciakowski et al.[1] A sketch of the experimental set up can be seen in Figure 4. The sample to be measured is glued to cover an aperture of a pressure cell. Several glues were experimented with, and it was found that Elmer's Stix-All glue has the most desirable properties for our purpose. The glue provides a good seal, eliminating leaks, but is still flexible, allowing the edges to move. Mineral oil was used as the pressure medium. As the pressure in the cell is increased, the sample bends outward. This produces a tensile strain in the epilayer grown

on the substrate. In the simplest approximation, the strain at the center of the outer
surface of a circular window (radius r, thickness d) with supported edges, and subject to
cell pressure p, can be written as

$$\varepsilon_{xx} = \varepsilon_{yy} = -\frac{(1+b)Cd}{r^2},\tag{2.1}$$

$$\varepsilon_{zz} = \frac{2S_{13}\varepsilon_{xx}}{S_{11}+S_{12}},\tag{2.2}$$

where

$$C = \frac{p}{E}\left(\frac{r}{d}\right)^3 r\frac{3}{16}\left(1-v^2\right),\ b = \frac{5+v}{1+v},\tag{2.3}$$

and S_{ij} are the compliance coefficients, E is Young's modulus, and v is Poisson's ratio.[2]
Since the sapphire substrate accounts for at least 95% of the thickness of the sample, the
a-axis Young's modulus (425 GPa)[3] and Poisson's ratio (0.27)[4] of the sapphire were used
in the calculation. The compliance coefficients of GaN (see Table I, Chapter 1) were
used to calculate ε_{zz}.[5] The radius of the window was chosen to be 3.449, 3.175, or 1.588
mm, depending on the available sample area. The thickness of the sample was measured
using an optical microscope.

Figure 5 shows the calculated strain for a typical 400μm-thick sample in a
window diameter of 3.175 mm. The strain is tensile in the x-y plane of the sample and
compressive in the z-direction due to the Poisson effect. The strain varies linearly with
the applied pressure. A P23 SPX pump was used to pressurize the system, and mineral
oil was used as the pressure transmitting fluid. The applied pressure was measured using
an OMEGA general service gauge type S or an OMEGA PX602-10KGV pressure

transducer. Due to the experimental constraints associated with the pressure cell, all biaxial strain experiments were carried out at room temperature.

2.3 High-resolution transmission electron microscopy

The structure of some of the samples was determined through the use of high-resolution transmission electron microscopy (HRTEM). This work was done by Christian Kisielowski at the *National Center for Electron Microscopy, Lawrence Berkeley National Laboratory*. For HRTEM, the cross section samples were mechanically thinned and ion milled to electron transparency. A short etching procedure removed the surface damage produced by the milling process[6]. The Atomic Resolution Microscope was operated at 800 kV to produce lattice images. The digitized lattice images were exploited to measure local strain profiles using the following procedure. A search program determines the position of each individual "blob" in images with sub pixel accuracy. This position relates to atomic columns in the sample and can be used to measure the size of each structural unit cell. From these measurements, the a- and c-lattice parameters are determined on an atomic scale. The local strain is defined as the deviation of the local lattice parameter from that of the GaN matrix. Since the InGaN layer is epitaxially grown on GaN, the *a*-lattice parameter of the layer is constrained to equal that of the GaN matrix. The *c*-lattice parameter on the other hand, expands or contracts depending on the sign of the stresses. A calibration procedure and Vegard's law were used to relate this strain to local alloy concentration. Strain relaxation processes were minimized by producing images from areas that were 10-50 times thicker than the width of the wells. The electron acceleration voltage of 800 kV in the Atomic

Resolution Microscope was utilized for this purpose. Such methods were developed for strain profiling and mapping in cubic and hexagonal systems[7,8].

2.4 Samples and structural analysis

A hydride-vapor phase-epitaxy (HVPE) GaN layer grown on sapphire was used to provide a reference for the InGaN QW structures biaxial strain results. The thicknesses of the GaN epilayer and sapphire substrate were 17μm and 360μm, respectively. This sample was obtained from American Xtal Technology (AXT). Many InGaN QW structures from various sources were used in this work. Nichia Chemicals provided both commercial and non-encapsulated metal-organic chemical vapor deposition (MOCVD)-grown LED devices. Prof. I. Akasaki from the High-Tech Research Center and Department of Materials Science Engineering, Meijo University, provided a single MOCVD grown InGaN QW structure, as did J. W. Yang from APA Optics. Akasaki's sample is unique in that it was grown with very high ($5*10^{18}$ cm^{-3}) Si doping in the barrier layers. The sample from APA has 3 pairs of QWs, each with a different indium content and QW thickness. Hewlett-Packard (HP) also provided a single MOCVD-grown structure. This sample, with more than 30% indium in the QW, has the highest indium content of any samples we have measured.

More recently, N. Gardner from LumiLeds Lighting has provided us with a number of unprocessed MOCVD-grown LED structures. These samples are divided into two series. Samples 1-4 vary in emission wavelength from UV to yellow-green and are referred to as the "color-series." Samples 5-7 vary only in QW thickness and are referred to as the "L_w-series." The only difference in these last three samples is the growth time for the QW layer. Through the POLARIS MURI project, we have received 3 MBE-

grown InGaN QW structures from J. Speck, University of California at Santa Barbara (UCSB). These samples were grown on an MOCVD GaN-template under identical conditions except for the indium flux. This resulted in samples with varying indium concentration, but similar in all other aspects. Therefore they are referred to as the "*x*-series."

Various methods have been used to determine the structural parameters of the obtained samples. The indium content and well and barrier thicknesses of the samples we received from LumiLeds and UCSB were determined by high-resolution x-ray diffraction. Excellent agreement of experimentally observed profiles across the symmetric GaN(0002) reflection with simulations based on dynamical diffraction theory[9] allow us to extract the In content of the well and well and barrier thickness with high accuracy.

Four MOCVD-grown samples were analyzed in greater detail: the commercial green (sample 1) and blue (sample 2) LEDs manufactured by Nichia Chemicals, and the structures manufactured by APA Optics (sample 3) and HP (sample 4). Quantitative structural and chemical information was found through a combination of Secondary Ion Mass Spectrometry (SIMS), Rutherford Back Scattering (RBS), Electron Energy Loss Spectroscopy (EELS) and High Resolution Transmission Electron Microscopy (HRTEM).[10] The active region of sample 1 consists of a 2.5-nm thick InGaN layer ($x=0.22+/-0.03$). Sample 2 has the same indium content, but the quantum well thickness is 1.5 nm. The APA structure consists of a 1.85-μm thick GaN layer followed by a series of six quantum wells. Each quantum well consists of an approximately 5-nm thick InGaN layer sandwiched between two 20-nm thick GaN barriers and is repeated twice.

The average x values are 0.06, 0.1 and 0.15, for the first, second and third pairs of wells, respectively. The exact thickness of these wells is 3.5 nm, 4.5 nm and 5.3 nm, respectively. Sample 4 consists of a series of 10 quantum wells of thicknesses 1.5-1.7 nm and an average x value of 0.32+/-0.06. The structural details of all samples are shown in Table I.

Figure 6 summarizes essentials of the HRTEM analysis[6]. It depicts strain profiles across quantum wells recorded at a spatial resolution of 0.5 nm. These profiles were obtained by averaging local values of c-strain across a row in the HRTEM image. As previously discussed, these strain profiles correspond directly to the indium concentration profiles, which are also included in Figure 6. Thus, Figure 6 shows the shapes (thickness and depth) of the quantum wells in samples 1 through 4. The figure shows that the quantum well in sample 3 is significantly broader (~5 nm) and of lower indium concentration compared with the other samples. Sample 4 shows the highest indium concentration and a well thickness that is similar to that of the blue Nichia LED (sample 2, ~1.5 nm). The indium concentrations in the blue and the green Nichia LEDs (samples 1 & 2) are similar, but the well width in sample 1 is significantly broader (~2.5 nm). The inset depicts that in all cases blue and green emission was observed that does NOT scale with the indium concentration.

While Figure 6 shows the local *average strain* in the well, Figure 7 shows its *standard deviation*. Each data point in the figure corresponds to the analysis of an HRTEM image of a single layer. The standard deviation was calculated from the fluctuation of the strain along that layer. The standard deviation of the c-strain is interpreted in terms of indium concentration fluctuation in the well. The indium

fluctuation calculation is based on the previously made correlation between the indium fraction and c-strain. Figure 7 shows that as the average indium fraction increases, the indium concentration fluctuations also increase.

2.5 Summary

In the chapter we presented the basic experimental tools used for this work. In PL, a HeCd laser was used to excite the luminescence, while in EL, the built-in contacts were used to excite the luminescence by current injection. A 0.85-m spectrometer was used to measure the luminescence as a function of energy (wavelength). In TR-PL, a Ti:sapphire laser was used to generate 150fs pulses. The time-dependent luminescence was then measured with a streak camera.

This characterization is often done as a function of excitation density, temperature, and/or biaxial strain. The excitation density was varied by the use of filters for PL, injection current for EL, and tuning for TR-PL. The temperature was varied through the use of a closed-cycle He cryostat. The biaxial strain was produced through the use of a specially designed pressure cell. As pressure is applied, the sample, mounted as a window for the pressure cell, bends outward, inducing a tensile biaxial strain in the epilayer.

InGaN QW structures were obtained from various sources, including academic institutions, such as UCSB and Meijo University, and corporations in the LED industry, such as LumiLeds and Nichia Chemicals. The structural parameters of these samples were characterized by various techniques, such as HR-TEM and HR-XRD. Table 2.1 lists the samples and their structural parameters. HR-TEM studies reveal that the indium inhomogeneity increases with increased average indium concentration in the layer.
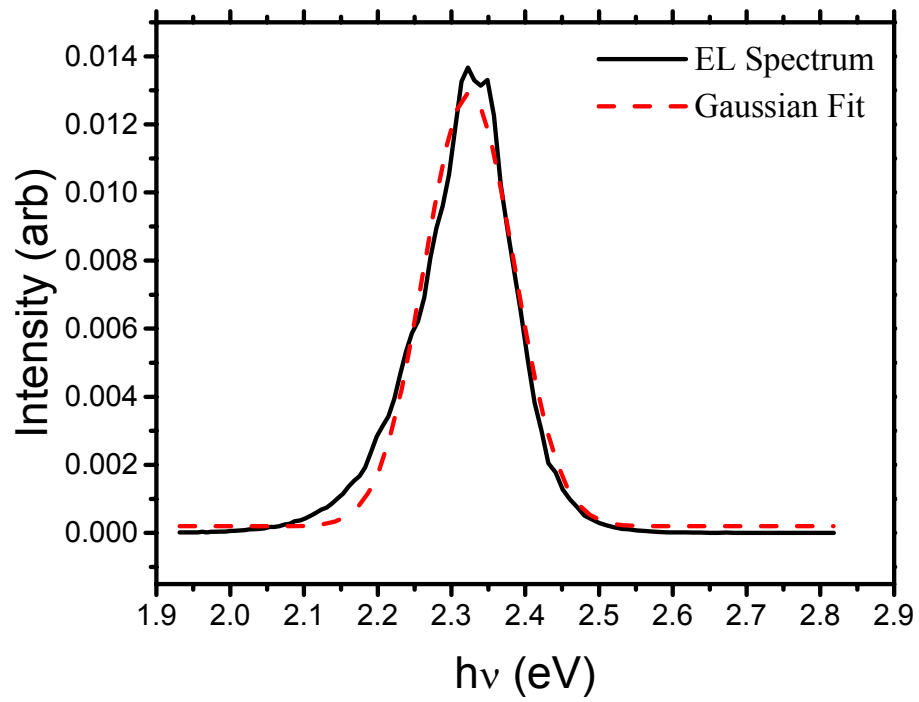
Figure 1: EL spectrum of a Nichia green LED (solid black line). A Gaussian fit of the data is also shown (dashed red line).
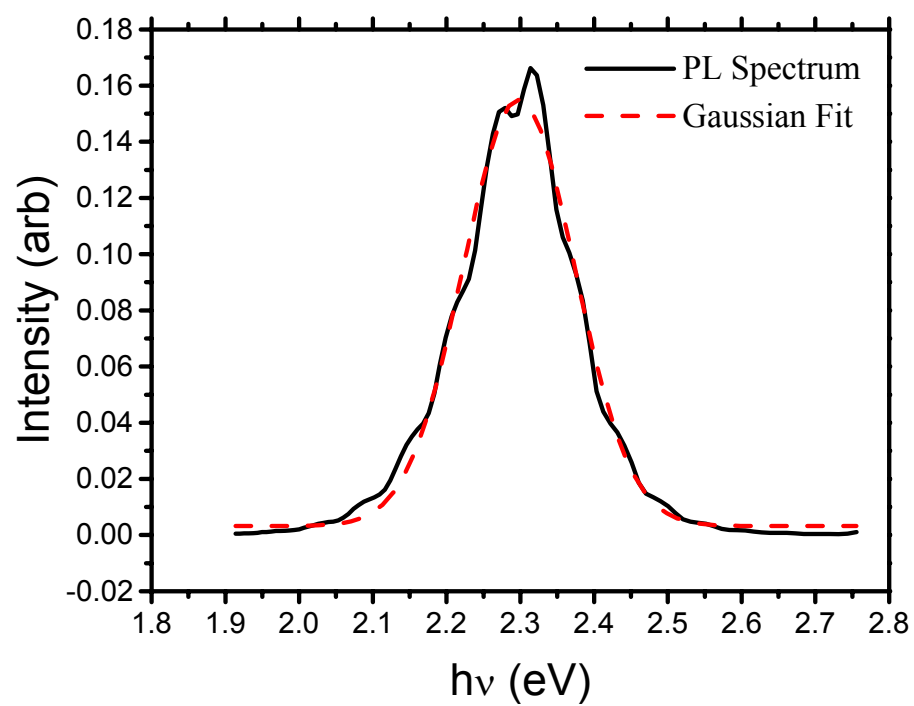
Figure 2: PL spectrum of a Nichia green LED (solid black line). A Gaussian fit of the

data is also shown (dashed red line).
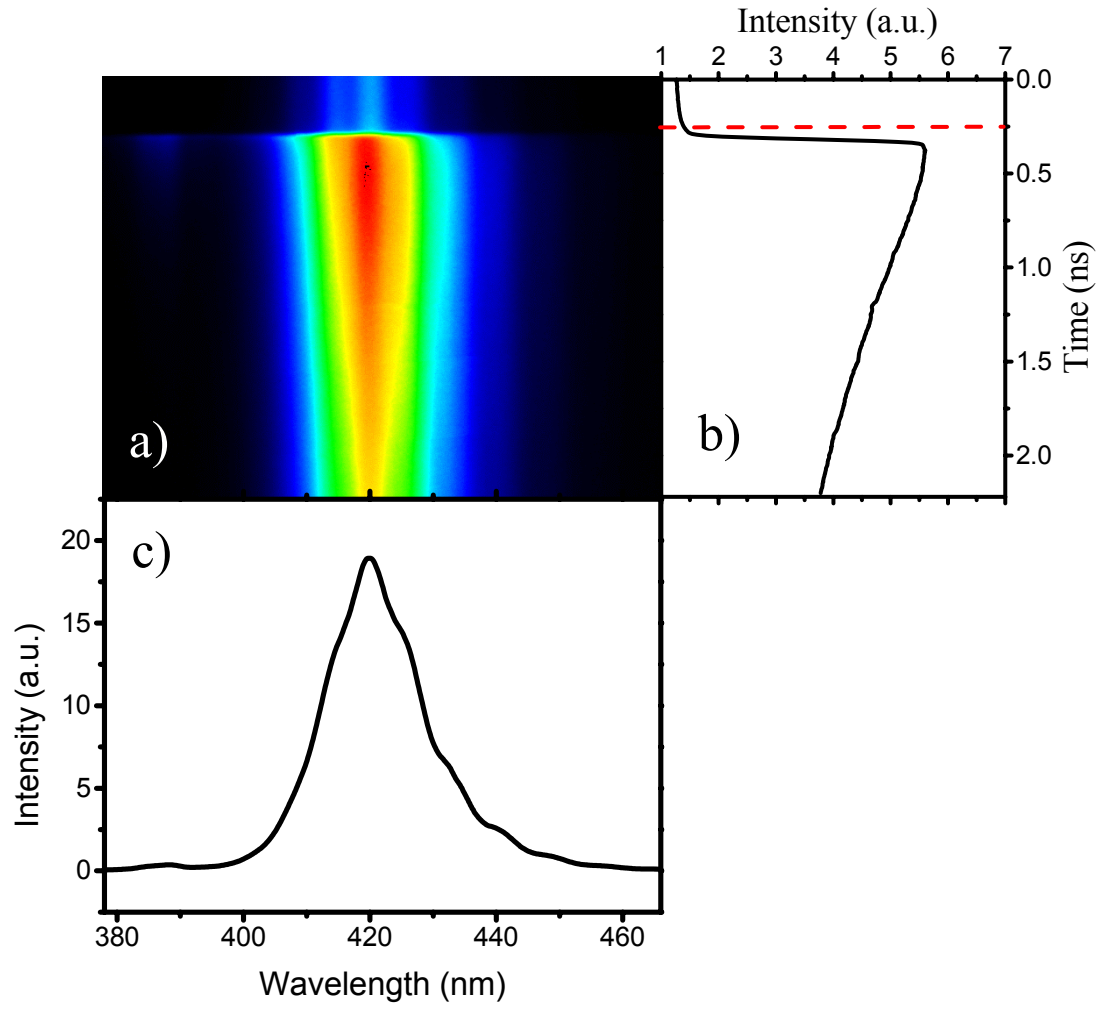
Figure 3: TRPL spectrum of InGaN QW structure, Lumileds #5. (a) Streak camera image. (b) Averaged decay across the spectrum. (c) Average spectrum across the decay.
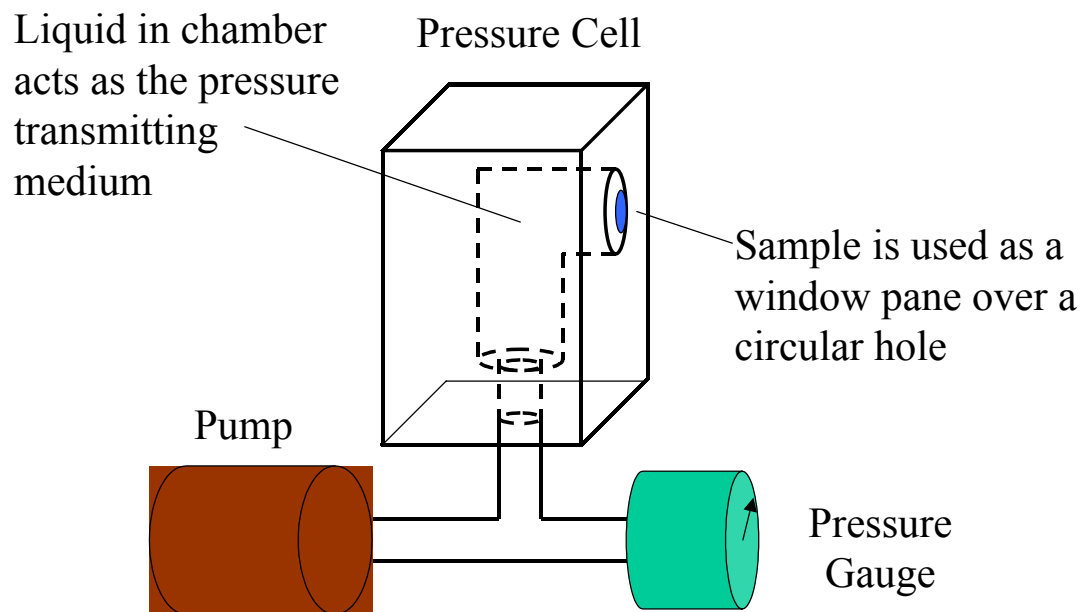
Figure 4: Diagram of the biaxial strain-inducing device.
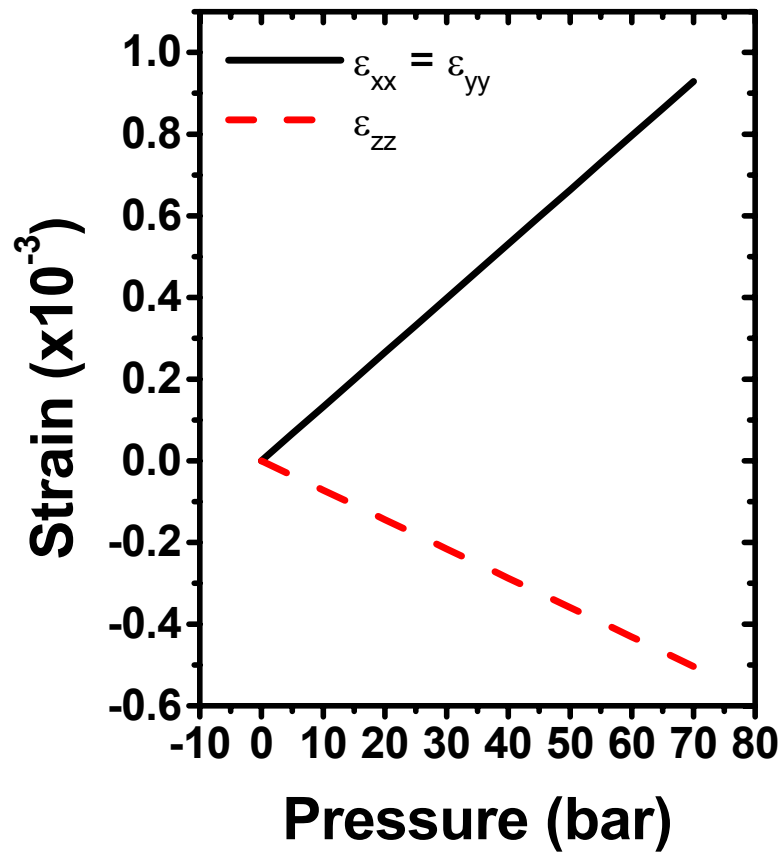
Figure 5: Strain induced on the outer surface of the sample, at the center of the window, as a function of pressure in the biaxial strain device.
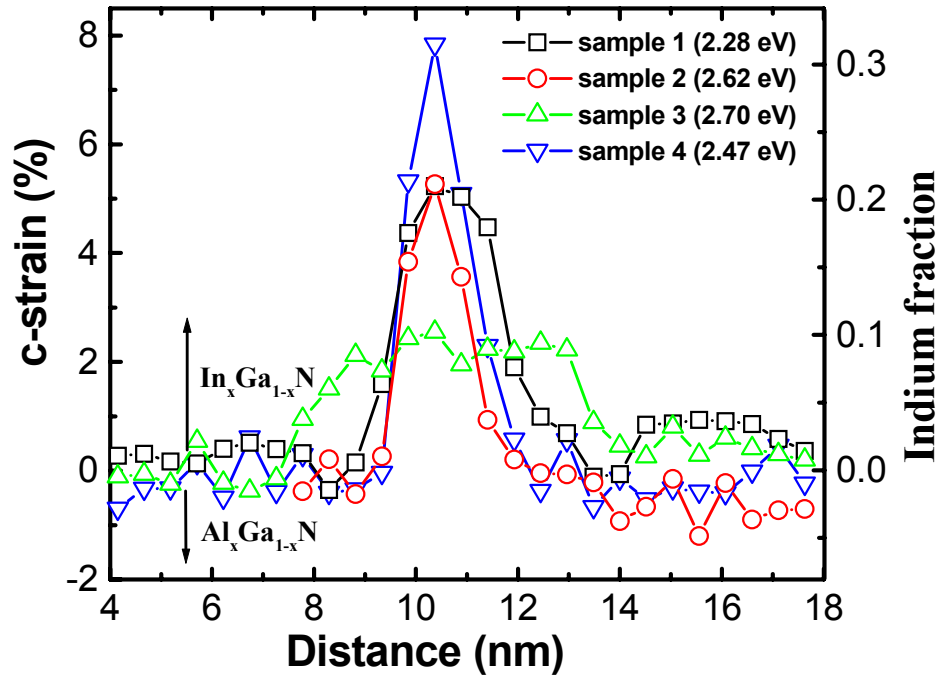
Figure 6. Average strain profiles across the active region of samples 1 through 4. Also shown is the indium fraction that corresponds to the *c*-strain. Light emission energies are indicated[6].
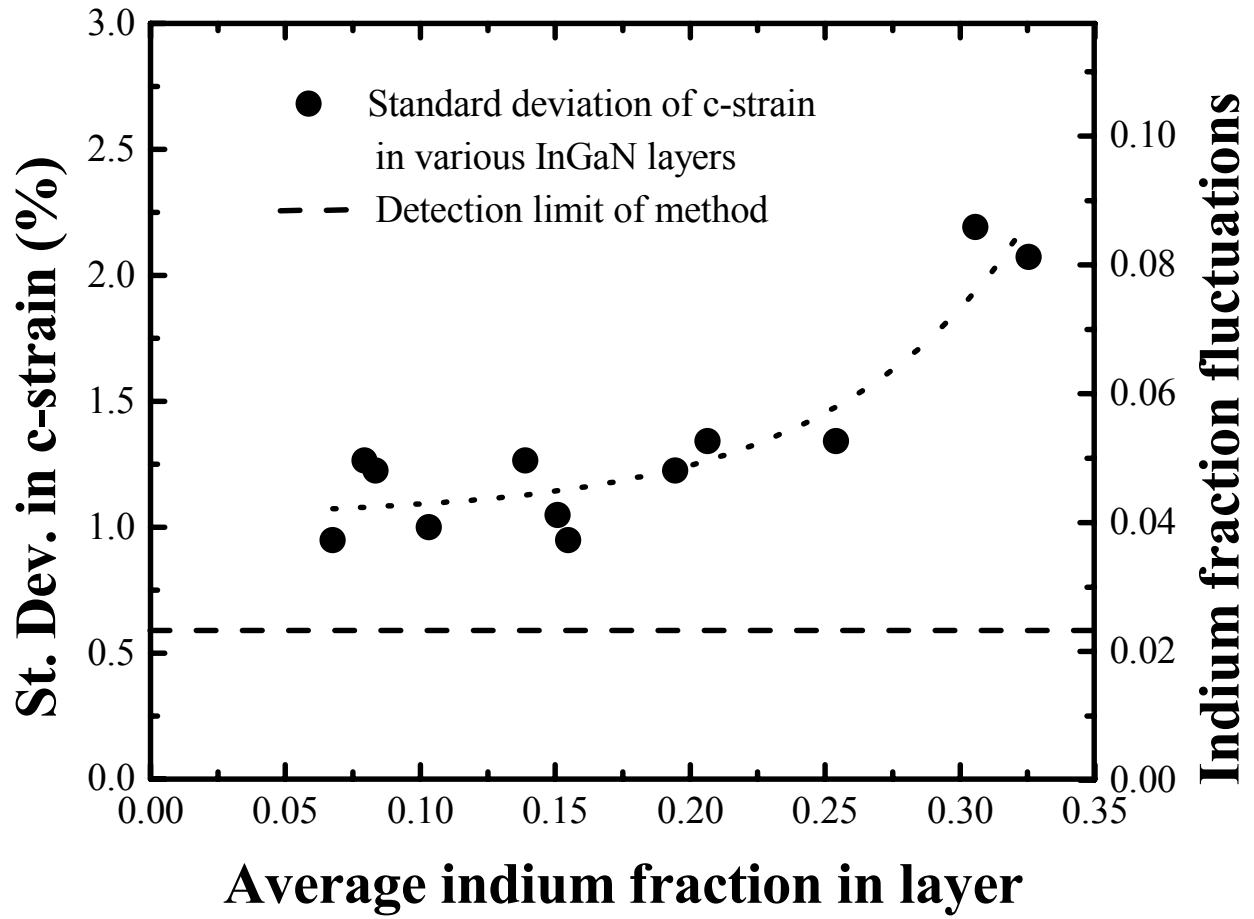
Figure 7: Standard deviation of the c-strain in InGaN layers with various indium fractions. Also shown are the indium fraction fluctuations that correspond to the c-strain fluctuations. The detection limit is the standard deviation of the c-strain in the surrounding GaN matrix[6].

2.7 Tables

Table 2.1: InGaN QW Structures

Sample names	# of wells	L_w (nm)	L_b (nm)	Indium content, x	Thickness (μm)	$h\nu_{peak}$ (eV)
#1:	1	2.5		0.22 +/- 0.03		2.30
#2:	1	1.5		0.22 +/- 0.03		2.62
#3:	2	3.5	20	0.06	610	2.6-8
	2	4.5		0.1		
	2	5.3		0.15		
#4:	10	1.5-1.7		0.32 +/-0.06		2.51
LumiLeds 1	4	2.45	11	0.089	425	2.97
LumiLeds 2	4	3.02	11	0.12	435	2.66
LumiLeds 3	4	3.02	11	0.159	425	2.43
LumiLeds 4	4	3.36	11	0.154	415	2.30
LumiLeds 5	4	1.76	11	0.11	425	2.95
LumiLeds 6	4	3.24	11	0.11	395	2.75
LumiLeds 7	4	2.71	11	0.11	395	2.81
Akasaki	3	3	10	0.12	365	3.05
UCSB 1	13	4.2	7.3	0.119	395	2.58
UCSB 2	13	4.2	7.3	0.085	385	2.75
UCSB 3	13	4.2	7.3	0.025	390	3.13

2.9 References

[1] W. Trzeciakowski and T. P. Sosin, J. Phys. Chem. Solids **56**, 649 (1995).

[2] S. P. Timoshenko, *Theory of Plates and Shells* (McGraw-Hill, New York 1959).

[3] H. N. G. Wadley, Y. Lu, and J. A. Goldman, J. of Nondest. Eval. **14**, 31 (1995).

[4] S. Sakaguchi, N. Murayama, Y. Kodama, and Fumihiro Wakai, J. Mat. Sci. Lett. **10**, 282 (1991): $\nu = 0.26$. Sapphire provider, Saphikon: $\nu = 0.27\text{-}0.30$.

[5] A. Polian, M. Grimsditch, and I. Grzegory, J. Appl. Phys. **79**, 3343 (1996).

[6] C. Kisielowski, in *Proceedings of the 2nd International Symposium of Blue Laser and Light Emitting Diodes* (Ohmasha Ltd., 1998), p.321.

[7] H. Seitz, M. Seibt, F.H. Baumann, K. Ahlborn et al. phys. stat. sol. (a) **150**, 625 (1995).

[8] C. Kisielowski, O. Schmidt, J. Yang, MRS Symposium Proceedings **482**, 369 (1998).

[9] O. Brandt, P. Waltereit, and K. H. Ploog, Phys. Rev. B (submitted)

[10] P. Perlin, C. Kisielowski, V. Iota, B.A. Weinstein, L. Mattos, N.A. Shapiro, J. Krueger, E.R. Weber, J. Yang, Appl. Phys. Lett. **73**, 2778 (1998).

Chapter 3: Basic luminescence results

In studying the luminescence using the techniques mentioned in the previous chapter, we generally focus on the luminescence associated with the radiative transition in the QW. This peak usually dominates over other radiative transitions since mobile electrons and holes from the bulk layer become trapped in the lower potential of the QW and are confined, resulting in strong overlap of electron and hole wavefunctions. This results in an increased transition probability and strong luminescence from the QW.

The typical method we use to analyse the QW luminescence is by evaluating its peak energy, full width at half maximum (FWHM), Intensity, and carrier lifetime. Therefore, after collecting a spectrum using the methods outlined in the previous chapter, the raw data is plotted using Microcal Origin. The peak energy and FWHM are then found through fitting the raw data with a Gaussian curve, which usually describes the luminescence well. This is because the overall luminescence is the sum of emissions from distinct sites that vary from one another in their transition energy in a random fashion. Figure 1 shows an example of a luminescence spectrum together with a Gaussian fit. The peak intensity is found by integrating the actual PL spectrum associated with a given peak.

3.1 Peak energy

The energy of luminescence gives important clues about the radiative transition in InGaN QW structures. We demonstrate this fact through the study of Samples 1-4, whose structure has been studied to great detail (see Chapter 2).[1] The PL peak energies of Samples 1-4 are shown together with their average indium concentration in Figure 2.

A plot of the likely position of the energy gap, using Eq. 1.7 ($E_g^{InN} = 0.77$, $b = 1.43$)[2] is also shown in Fig. 2 as a reference. It is clear from Fig. 2 that the peak energy does not correlate well with the indium composition in the QW. Samples 1 & 2 emit at very different energies even though they have the same indium content, and Sample 4 emit at higher energies than Sample 1, even though it has significantly higher indium content.

As a cause for this poor correlation, we first consider quantum confinement, which has been shown to play an important role in quantum wells of comparable thicknesses.[3,4] Quantum confinement alters the lowest energy at which the electron may reside. Instead of residing in the minimum of the conduction band, an electron will reside in the lowest available quantized state. The holes in the valence band act in the same way. Thus, the transition energy is increased by the quantum confinement energies of the confined electrons and holes. The precise amount of change will depend on the depth, width, and shape of the quantum well. For the case of a square quantum well, of a thickness a and infinite potential barriers, the energy of recombination between the ground states in the conduction and valence bands is given by,

$$h\nu = E_g + \frac{\hbar^2 \pi^2}{2a^2}\left(\frac{1}{m_e} + \frac{1}{m_h}\right), \qquad (3.1)$$

where m_e and m_h are the effective masses of the electron and hole, respectively.

Using Equation (3.1) with a linear interpolation (between GaN and InN) of the effective masses of the holes and electrons predicts that a 1.5 nm well will emit at energy ~0.7 eV greater than a 2.5 nm quantum well. This value is certainly large enough to explain the difference in energies observed (~0.32eV). However, Eq. (3.1) also yields an overall confinement energy that is higher than the barriers themselves, where

confinement is no longer possible. The main reason behind this discrepancy is probably the fact that the barriers are far from infinite, as is assumed by Eq. (3.1).

Seeking for a better estimate of the confinement energy in these structures, we made use of a 1D Poisson/Schrödinger program, written by Greg Snider from the Department of Electrical Engineering, University of Notre Dame.[5,6] This program uses the method of finite differences to find the one-dimensional band diagram of a semiconductor structure. It then uses the results to calculate the quantized states. These more accurate calculations have yielded a more realistic difference of only ~0.18 eV between the 1.5 and 2.5 nm QWs. One should note that this value is smaller than the observed ~0.32 eV difference seen in Fig. 2.

According to the carrier separation model, the polarization induced electric fields leads to carrier separation and a redshift in the luminescence. Since a thicker QW would have a greater potential drop induced by a given electric field, we would expect the redshift of the luminescence to increase with the thickness of the QW. A rough estimate of the luminescence energy for this radiative transition gives:

$$h\nu \approx h\nu_0 - L_w E_w. \qquad\qquad (3.2)$$

Using Equation (1.6) we derive an electric field of ~3MV/cm for samples 1 & 2. The additional potential drop produced by increasing the thickness by 1nm would then reduce the luminescence energy by ~0.3 eV. This is precisely the difference we observe between these two samples.

From Fig. 2, it is apparent that the luminescence energy could be either larger or smaller than the energy gap of the average indium content of the QW, depending on the sample. While the carrier separation model can explain why the luminescence should

have a lower energy than the energy gap, it cannot account for the case where the energy is larger (i.e. Sample 4). Thus we believe that both the confinement energy and carrier separation model play important roles in influencing the transition energy in these devices.

3.2 Peak width

The FWHM of the luminescence may also give clues concerning the transition. We present the FWHM of the x-series, L_w-Series, and color-series in Figure 3. Figure 3(a) shows the FWHM of the x-series as a function of indium content. We find that the FWHM tends to increase with indium content. Figure 3(b) shows the FWHM of the L_w-series as a function of QW thickness. We find that the FWHM tends to increase with the thickness of the QW. Figure 3(c) shows the FWHM of the color-series as a function of luminescence energy. Here the general trend is an increase of the FWHM with redshift away from the GaN energy gap, which corresponds in general to increasing indium content and QW thickness.

One of the peculiar luminescence properties of InGaN QW structures is their consistently large luminescence FWHM ~ 100-200 meV at room Temperature. Even at low temperature the FWHM usually exceeds 50 meV. Various explanations have been offered for this phenomenon. It has been proposed that the source of the broad emission lies in inhomogeneities in the InN concentration, thickness, and/or strain in the InGaN QW. That is, the overall luminescence is a sum of photons produced at distinct sites in the structure's active layer. If one site varies from another in properties that affect the radiative transition energy (i.e. InN concentration, strain, and QW thickness), then the photons emitted from that site will have a different energy from the other. If there is a

random, continuous variation in these properties throughout the active region, the overall luminescence will be Gaussian-like, the width thereof depending on the magnitude of the variation.

One of the most common explanations for this variation is the inhomogenous indium distribution in the QW.[7] According to the carrier localization model, carriers are localized at indium-rich nano-clusters. Now, if these sites vary in indium content, they will vary in their energy gap, and so in the resulting radiative transition energy. Similarly, one could propose a variation in the size of the nano-clusters to be the source for variation in transition because different sizes would result in a difference in the confinement energy.

Another commonly proposed source for this variation is a variation in QW thickness. This does not require that the carrier localization transition be assumed. Even if the carriers are simply confined in the QW as opposed to the nano-clusters, they will experience varying confinement energy, and thus transition energy, based on the local QW thickness. A variation in the QW thickness would in addition greatly affect the transition energy in a structure where the carrier separation transition model dominates, since the redshift depends on the separation of the carriers, which in turn depends on the thickness of the QW.

The increase of the FWHM with increasing indium content is consistent with our expectation. As was shown in Figure 2.7, the indium inhomogeneity tends to increase with increasing indium content. This should translate to a wider distribution of sizes and indium concentrations in the indium-rich nano-clusters. This results in a larger

distribution in energy of radiative transitions emanating from these sites and thus, a larger FWHM.

There is no obvious explanation for the observed increase in FWHM with increasing QW thickness. One possibility is that as the average thickness increases there is an increased inhomogeneity in the overall thickness of the layer, allowing for a greater magnitude of fluctuation in the transition energy. The other explanation would be that that with increased QW thickness there is an increased inhomogeneity in indium distribution. Quantitative HR-TEM analysis could be used to establish which of the above hypotheses is correct.

The reason for the increase in FWHM as the LED color changes from UV to green-yellow is consistent with the earlier results. In order to shift the emission of the device from GaN (3.4eV) toward InN (1.9eV), the QW structure requires more indium in the QW and/or a thicker QW. Since the FWHM increases with indium content and QW thickness, it stands to reason it would increase with a color shift away from UV toward green.

3.3 Peak intensity

The peak intensity could also provide useful information because it roughly corresponds to the efficiency of converting the excited carriers to photons in the sample. That is, if one sample gives a stronger luminescence signal than another sample under identical conditions, then the sample with the stronger emission is probably more efficient in converting carriers excited either by laser (PL) or current (EL) into photons. This efficiency could be related to the radiative transition in the QW.

One of the peculiar properties of InGaN QW structures is their strong luminescence in the presence of a very high concentration of dislocations. It has been proposed that the localization of carriers in indium-rich nano-clusters protects the carriers from the non-radiative recombination centers that are usually associated with dislocations. Measuring the strength of the luminescence as a function of temperature may therefore provide some correlation with the depth of the potential depression caused by these indium-rich nano-clusters.

However, while this method is quick and convenient, it is not very precise, and great care must be taken in interpreting results. This is because many factors affect the observed luminescence intensity. Obvious variables are the excitation density (laser power/focus) and extraction efficiency (lenses position, slit width/focus). However, there are additional variables such as the spectrometer wavelength efficiency. That is, the spectrometer transmits some wavelengths more efficiently than others. For these reasons, we do not use this analysis to compare one sample with another. Rather, we use it to compare the luminescence of the same sample under different conditions such as temperature and excitation density. Such data will be presented in the following chapter.

3.4 Carrier lifetime

The decay of the luminescence obtained through TRPL also gives valuable information concerning the radiative transition. This is because the luminescence intensity is related to the overlap of the electron and hole wavefunctions. Therefore a decay of the luminescence translates into a decay of the excited carriers involved in the studied radiative transition.

The ideal method of calculating the lifetime is to fit the luminescence decay to a sum of exponentials with different time constants to allow for different processes involved in the decay. That is:

$$I(t) = I(0)\left(A_1 e^{-\frac{t}{\tau_1}} + A_2 e^{-\frac{t}{\tau_2}} + ... \right)$$ (3.3)

where I is the intensity, t is the time, and A_i and τ_i are the prefactors and time constants associated with the different decay processes. In a case where one decay process dominates over the others, the additional exponentials can be droped, and the decay becomes a single exponential.

One of the unusual luminescence properties of InGaN QW structures is a very long decay time, often of the order of tens of nanoseconds. When the lifetime is that long, it becomes difficult to fit an exponential to the data because the streak camera only gives us a 2 nanosecond window of the decay. Therefore, we use an alternative method to calculate the carrier lifetime in samples with large lifetimes (>5ns).

We assume that the decay is described by a single exponential to get,

$$\tau = \frac{t}{\ln\left(I(t) \middle/ I(0) \right)}.$$ (3.4)

We then take the peak intensity right after the excitation pulse to mark *I(0)* and the peak intensity right before to mark *I(t)*. Then, using the pulse repetition rate of 13ns, we can estimate the average carrier lifetime, τ.

It should be noted that, due to the long transition lifetimes, a significant fraction of the excited carriers remains when the next excitation pulse arrives. Thus the carrier density actually depends on the lifetime. If the carrier lifetime also depends on the carrier

density (Chapter 4), Eq. 3.4 will yield the lifetime that corresponds to the effective excitation density instead of the real one. This effect becomes more pronounced as the lifetime increases.

Figure 4 shows the carrier lifetime of the 7 LumiLeds QW structures as a function of luminescence peak energy. The figure shows a clear trend of increasing lifetime with decreasing luminescnece photon energy. This observation can be explained by using the carrier seperation model. According to Eq. 3.2, we expect that the luminescence peak position should decrease linearly with the carrier separation, $\sim L_w$. On the other hand, the carrier lifetime should increase roughly exponentially with increasing carrier separation.[8] Thus, at first approximation, the carrier separation model predicts an exponential increase of the carrier lifetime with decreasing luminescence energy. The confirmation of this relationship in Fig. 4 suggests that the carrier separation model is indeed descriptive of the radiative transition in these samples. In Chapter 4, we show that these lifetimes are not strongly dependent on the excitation power. Thus we do not anticipate the previously noted systematic error to affect greatly the results and interpretation of Fig. 4.

3.5 Summary

We have found that the luminescence energy does not always scale with indium composition in our samples. This suggests that additional structural parameters play a role in determining the transition energy besides the energy gap. In particular, we show that the thickness of the QW in particular does play an important role in determining the transition energy. Quantum confinement in very narrow wells increases the transition energy, while carrier separation, across the potential drop in the carrier separation model, reduces the transition energy.

We have found that the FWHM of the luminescence increased with indium composition, QW thickness, and luminescence wavelength. The increase of the FWHM with indium content is consistent with HR-TEM results that show an increase of indium fluctuations with an increase of the average indium content in the layer. The increase of FWHM with QW thickness may indicate an increase in QW thickness fluctuations or indium fluctuations with increased average QW thickness. The increase with luminescence wavelength simply follows the other two trends. Longer-wavelength emitting devices are generally achieved by increasing the indium concentration and/or QW thickness in the QW structure (see Table 2.1).

The exponential relationship between LED luminescence color and carrier lifetime for the LumiLeds samples was shown to be consistent with the carrier separation model. As the carrier separation increases, the luminescence redshifts due to the potential drop across the QW, and the carrier lifetime increases exponentially due to the reduced overlap of the electron and hole wavefunctions.
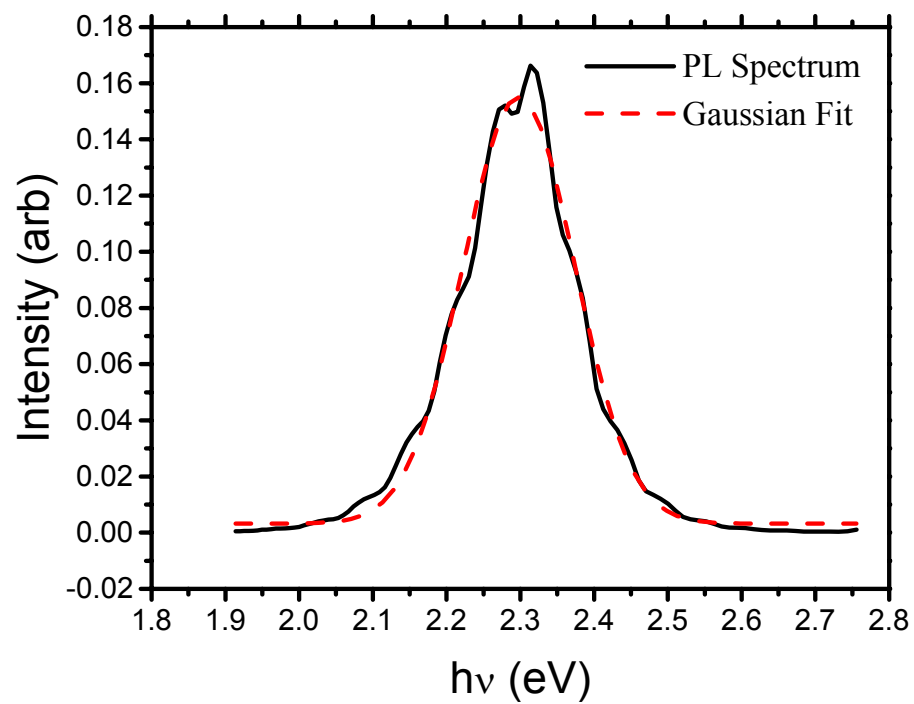
Figure 1: PL spectrum of a Nichia green LED (solid black line). A Gaussian fit of the data is also shown (dashed red line).
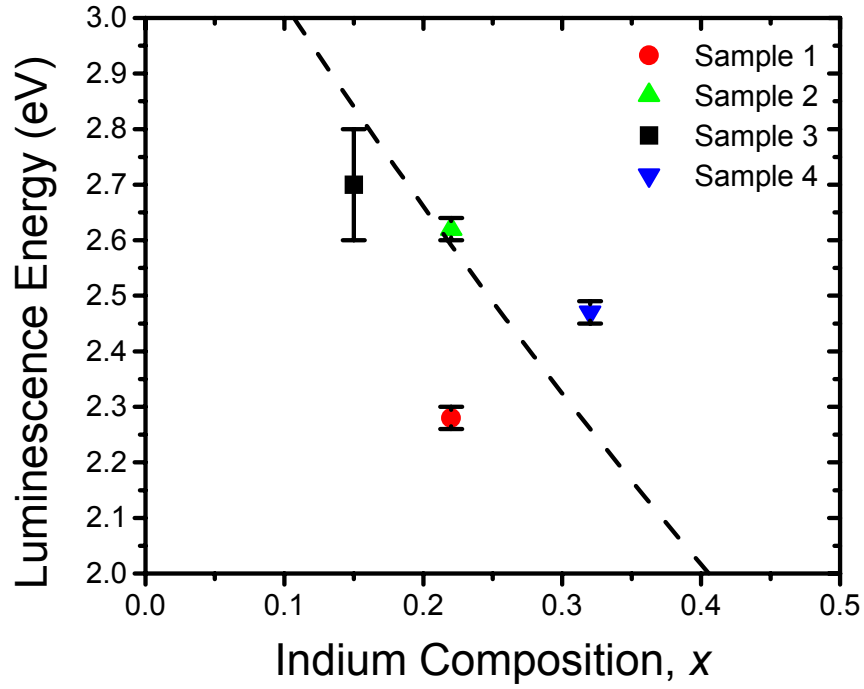
Figure 2: Room temperature luminescence energies of Samples 1-4 as a function of average indium fraction. Error bars represent the sensitivity of the luminescence energy on the excitation density (Fig. 4.1). The theoretical energy gap of InGaN (dashed line) is plotted as a function of indium fraction (see text).

Figure 3: The FWHM of the PL peak from various InGaN QW structures. (a) MBE grown samples with varying indium content in the QW. (b) MOCVD grown samples with varying QW thickness. (c) MOCVD grown sample emitting at various colors.

Figure 4: Carrier lifetime of MOCVD grown InGaN QW structures from LumiLeds as a function of luminescence peak energy.

3.7 References

[1] N. A. Shapiro, P. Perlin, C. Kisielowski, L. S. Mattos, J. W. Yang and E. R. Weber, MRS Internet J. Nitride Semicond. **5**, 1 (2000).

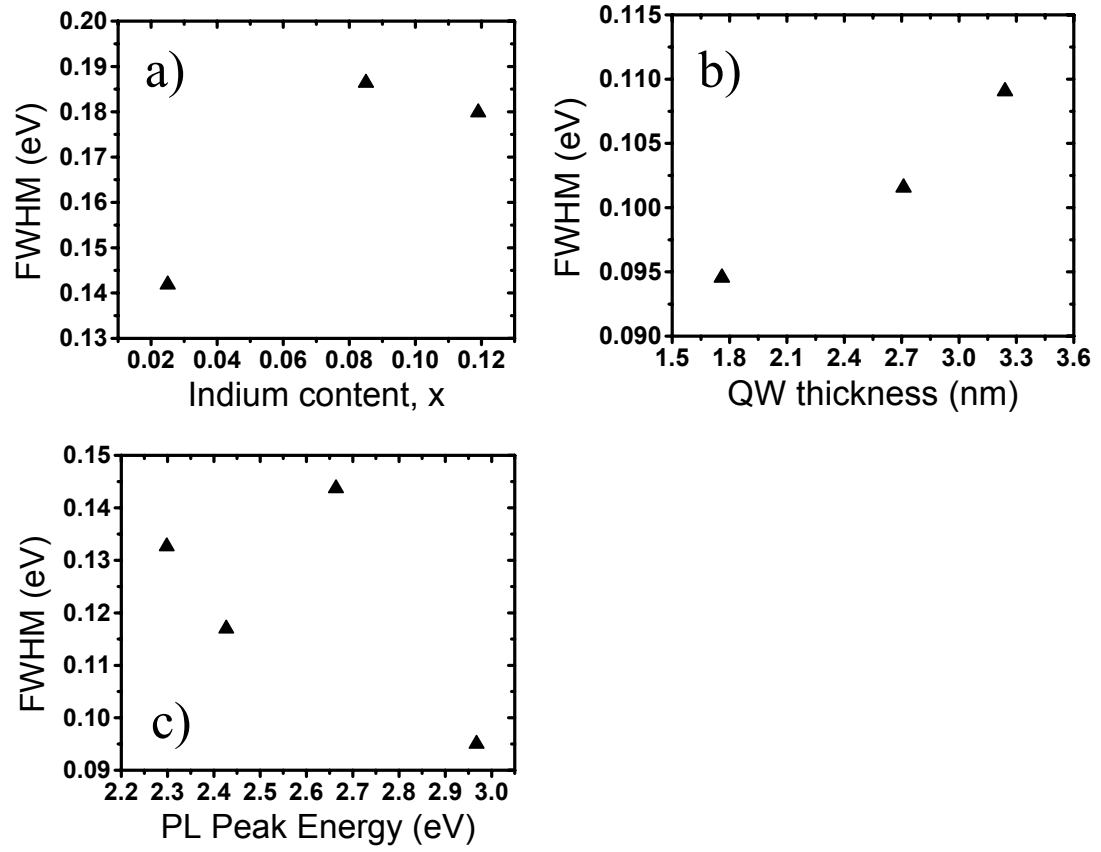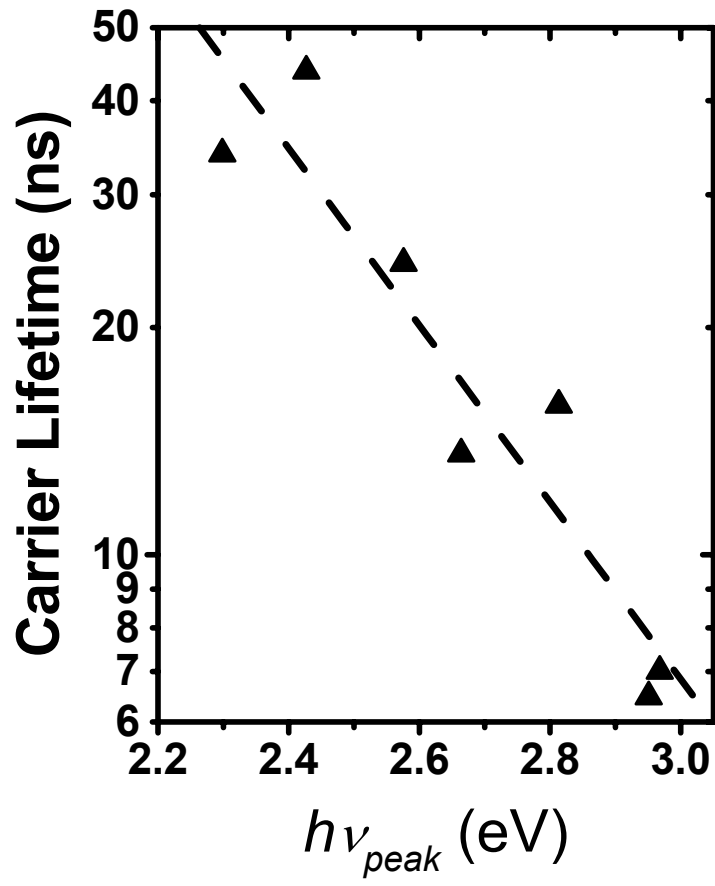[2] J. Wu, W. Walukiewicz, K.M. Yu, J.W. Ager III, E. E. Haller, Hai Lu, William J. Schaff, Appl. Phys. Lett. **80**, in press (2002).

[3] T. Takeuchi, S. Sota, M. Katsuragawa, M. Komori, H. Takeuchi, H. Amano and I. Akasaki, Jpn. J. Appl. Phys **36**, L382 (1997).

[4] A. Hangleiter, J. Seo Im, H. Kollmer, S. Heppel, J. Off, Ferdinand Scholz, MRS Internet J. Nitride Semicond. Res. **3**, 15 (1998).

[5] G.L. Snider, I.-H. Tan, and E.L. Hu, J. Appl. Phys. **68**, 2849 (1990)

[6] I.-H. Tan, G.L. Snider, and E.L. Hu, J. Appl. Phys. **68**, 4071 (1990)

[7] W. Shan, W. Walukiewicz, E.E. Haller, B.D. Little, J.J. Song, M.D. McCluskey, N.M. Johnson, Z.C. Feng, M. Schuman and R.A. Stall, J. Appl. Phys. **84**, 4452 (1998).

[8] E. Berkowicz, D. Gershoni, G. Bahir, E. Lakin, D. Shilo, E. Zolotoyabko, A. C. Abare, S. P. Denbaars, and L. A. Coldren, Phys. Rev. B **61**, 10994 (2000).

Chapter 4: Excitation power and temperature

A valuable method for studying radiative transitions is to measure the luminescence as a function of some variable in the environment where the transition takes place. This type of measurement reveals the dependence of the transition on that parameter, and thus can give clues concerning the nature of the transition. In this chapter, we show and discuss the results of luminescence studies as a function of excitation density and temperature.

4.1 Results

4.1.1 Luminescence energy and carrier lifetime as a function of excitation density

Photoluminescence experiments of Samples 1 through 4 were carried out for a range of excitation densities. The photoluminescence peak energies of all samples at room temperature are shown as a function of the excitation density in Figure 1. All of these samples show at least some increase in luminescence energy with excitation density (blueshift). This is expected because as the electrons and holes fill up their respective bands the average energy of transition increases. However, the increase of luminescence energy of sample 3 is much larger than that of the rest of the samples. Figure 2 shows the result of a similar experiment carried out on LumiLeds #3. Here we observe an actual decrease of emission energy (redshift) with increasing excitation density.

In order to investigate this phenomenon further, TRPL as a function of excitation density was also carried out on sample 3. Figure 3 shows both the luminescence peak energy and the carrier lifetime as a function of excitation density. Here again we see the large blueshift of the luminescence with increasing excitation density. However, we also

see that the excitation density drastically affects the carrier lifetime. In particular, the lifetime strongly decreases with increasing excitation density.

Figure 4 shows the TRPL results obtained with the 7 LumiLeds samples. None of these samples showed as drastic a reduction of the carrier lifetime with increasing excitation density. Figure 5 Shows the results obtained from Akasaki's sample. Since the luminescence decay was too fast and of non-exponential character at low excitation densities, instead of the usual method of calculating the carrier lifetime, we simply use the 1/e decay time. This is the time it takes the luminescence to decay to 1/e of its original value. As can be seen from Figure 5, the lifetime actually increases with increasing excitation power, instead of decreasing, as was the case for sample 3.

4.1.2 Luminescence energy and FWHM as a function excitation density and temperature

The EL peak energy of sample 1 (commercial green Nichia LED) is shown in Figure 6 as a function of the current for 50, 177 and 295 K. A pattern is seen in the temperature-current dependencies of the peak. Note that at low currents, the peak energy increases with increasing temperature even though the energy gap should be shrinking. The corresponding EL linewidths (FWHM) are shown in Figure 7 as a function of the current. At all temperatures and for low currents, the linewidth remains constant with increasing current. At higher currents, the peak becomes broader with increasing current. This broadening is most pronounced at the lowest measurement temperature of 50 K.

4.1.3 Luminescence intensity as a function of temperature

Valuable information can also be learned from studying the luminescence intensity as a function of temperature. This is because the luminescence intensity correlates with the efficiency of the conversion of excited carriers into luminescence in the structures. By comparing efficiencies between different samples, we may be able to understand the competition between radiative and non-radiative recombination in the QW structure.

Figures 8 and 9 show the change in PL integrated intensity for the 7 LumiLeds LED QW structures. Figure 8 contains the color-series (LumiLeds 1-4), and Figure 9 contains the L_w-series (LumiLeds 5-7). For all samples the intensity decreases as the temperature is increased. For the color series, we find that at room temperature the intensity tends to decrease with the redshift of the color. For the QW thickness series, we find that the intensity tends to decrease with increasing QW thickness.

4.2 Excitation density

4.2.1 Luminescence energy

The large "blueshift" of sample 3 with increasing excitation density agrees with predictions of the carrier separation model.[1] As the excitation density increases, the number of free carriers in the conduction and valence band also increases. These free carriers can act to screen the electric field in the quantum well. As the electric field is screened, the carrier separation and the potential drop across the QW are reduced. According to equation (3) in chapter 2, this would reduce the electric field induced "redshift", resulting in a blueshift of the luminescence.

The absence of this shift in samples 1, 2 and 4 should be explained. One explanation stems from the observation that sample 3 has the thickest well out of the 4 samples. The thicker the quantum well is, the greater is the spatial charge separation and potential drop across the well. Therefore the carrier separation results in a greater reduction of transition energy. Consequently, the excitation-induced blueshift is expected to be stronger in structures with thicker wells. However, rough calculations show that a 2.5-nm thick quantum well with x = 0.22 (sample 1) should still exhibit a polarization induced potential drop of about 70 % as compared with that of a 5.3 nm thick well with x = 0.15 (sample 3). Thus, we believe that an additional mechanism reduces the carrier separation related blueshift.

One explanation may be based on the presence of large potential fluctuations in the QW, like those produced by indium-rich nano-clusters. The carriers will reside in the local minima instead of separating to opposite sides of the well. Since the carriers are not separated, there should not be any blueshift. This explanation fits with the evidence from HR-TEM analysis performed by Christian Kisielowski, presented in Fig. 2.7. Samples 1, 2 and 4 have a higher average indium concentration than sample 3, and according to Fig. 2.7, the indium spatial fluctuation increases with increasing average indium concentration. It would stand to reason that in QWs with these large fluctuations the carriers will be localized in the minima created by these fluctuations instead of separating. Thus the radiative transition in sample 3, which has the lowest indium content, may be dominated by carrier separation, while the rest of the samples are not. Also, it is noteworthy that literature data show piezoelectric-effect dominated luminescence properties most convincingly for x values no greater than 0.15.[1,2]

One other possible explanation for the absence of the blueshift is the presence of doping related free carriers. GaN and InGaN usually have on the order of $\sim 10^{17}$ cm^{-3} n-type carriers in unintentionally doped layers. In addition, InGaN QW structures are frequently doped either to improve the luminescence properties or for device purposes. This is especially likely to be the case for the Nichia LEDs (samples 1 & 2). These samples are likely to have about $\sim 10^{18}$ cm^{-3} electrons in the QW before any excitation takes place. Thus, if the density of carriers excited by the laser is smaller than that produced by the Si donors, it would not increase the screening significantly, and no significant blueshift is expected.

Finally, one should consider competing effects that may shift the luminescence as a function of excitation density. As is seen in Figure 2, some samples actually exhibit a redshift with increased excitation density. This phenomenon is believed to be related to the many-body effect known as bandgap renormalization.[3] This effect is usually associated with high doping densities in semiconductors. Indeed, we have only observed it in samples intentionally doped with Si in the barrier layers. Thus, while a strong blueshift with increasing excitation density strongly suggests that the carrier-separation radiative transition play a dominant role in a given device, the absence of the blueshift does not prove that no carrier separation is taking place.

4.2.2 Carrier lifetime

As mentioned before, the TRPL reproduced the blueshift of sample 3 with increased excitation density (Figure 3). It also showed that this blueshift of the luminescence energy was accompanied by a strong decrease of the carrier lifetime. This

observation supports the earlier conclusion associating the blueshift with the carrier separation radiative transition model.

If the blueshift of the luminescence is indeed associated with a reduced potential drop across the QW due to increased screening of the electric field, the effective spatial separation between the electron and hole wavefunctions should also decrease. Since the probability of recombination is directly related to the overlap of the electron and hole wavefunctions, the carrier lifetime should also be reduced. Therefore we observe a reduction of the carrier lifetime with increasing excitation density.

Figure 4 shows the results obtained with a number of LED QW structures obtained from LumiLeds. None of these samples showed as drastic a reduction of the carrier lifetime with increasing excitation density. As mentioned earlier, there are two possible reasons. One is that that the carrier separation phenomenon is restricted by the presence of potential minima related to indium-rich nano-clusters. This explanation is not preferred because the rather low indium content in these samples (less than 15%) should not result in strong indium segregation effect. Also, other experiments, detailed in Chapters 3 & 6, suggest significant carrier separation in these structures. The alternative explanation, as was previously mentioned, is that the number of carriers excited by the laser is smaller than that which is already present in the QW due to doping. This explanation is supported in this case by the fact that the barriers in these QW structures have been intentionally doped with Silicon.

As is shown in Figure 5, Akasaki's sample showed a strong increase in carrier lifetime as a function of excitation density. This shift is in the opposite direction to that predicted by the carrier separation and so requires a different interpretation. A possible

explanation for this phenomenon follows. The very fast recombination that was observed at low excitation density suggests that the transition is of a non-radiative nature. Now, if there is a limited number of channels through which the non-radiative transition occurs, then, as we increase the excitation density, these channels will be saturated, limiting the rate of recombination. Therefore at the higher excitation density we expect a longer average carrier lifetime.

4.3 Electroluminescence as a function of excitation power and temperature

Eliseev et al[4] proposed that the radiative recombination in Nichia devices could be described as a transition between the density of tail states of the valence and conduction bands. Such tail states could result from indium inhomogeneity in the active layer, but they could also result from the inhomogeneity of other parameters that influence the transition energy. The model was used to explain the anomalous temperature dependence of the emission from Nichia LEDs. We now extend this model to explain both the temperature and the power induced shifts of the emission observed for sample 1.

The model assumes that the density of states (DOS) distribution of the tails can be described by the Gaussian functions

$$\rho_{e,h} = \rho_{0e,h} \exp\left[\frac{-\left(E - E_{0e,h}\right)^2}{2\sigma_{e,h}^2}\right], \tag{4.1}$$

where ρ_{0e}, ρ_{0h}, E_{0e}, E_{0h}, σ_{0e} and σ_{0h} are fixed parameters for band-tails of electron and hole states. ρ_{0e} and ρ_{0h} are the magnitudes for the normal densities of state for the ground state of a quantum well for the conduction and valence bands, respectively. They can be calculated by

$$\rho_{0e,h} = \frac{m^*_{e,h}}{\pi\hbar^2 d}, \tag{4.2}$$

where $m^*_{e,h}$ are the electron and hole effective mass, and d is the thickness of the quantum well. E_{0e} and E_{0h}, correspond to the normal energy gap edges, while σ_{0e} and σ_{0h} are the parameters that describe the width of the band tails.

Since E_{0e} and E_{0h} correspond to the band edges of the layer, the distance between them will vary with the band gap. Therefore,

$$E_{0e} - E_{0h} \cong E_g(T) = E_r - \frac{\gamma}{\beta+T} \cdot T^2, \tag{4.3}$$

where γ and β are material constants given in Table I and E_r is the distance between the band edges at 0 K. Since E_r is very difficult to calculate accurately, due to uncertainty in the bowing parameter and confinement energy, it is used as a fitting parameter in this simulation. Its value was set so that the simulated peak position at 295 K and low excitation levels would match with the experimental peak position at 295 K and low EL currents. A schematic of the DOS distribution in energy is shown in Fig. 10.

The band tails model also assumes that the tail states are localized enough to relax the momentum conservation rule. In this situation, an emission spectrum can be represented by the equation:

$$R_{sp}(h\upsilon) = \int \rho_e(E + h\upsilon)f_e(E + h\upsilon)\rho_h(E)f_h(E)dE, \tag{4.4}$$

where $f_e(E + h\upsilon)$ and $f_h(E)$ are the Fermi occupation functions for the two tails involved, each being characterized by a quasi-Fermi level. The magnitude of $R_{sp}(h\upsilon)$ corresponds to the likelihood that a radiative recombination event resulting in a photon of an energy $h\upsilon$ will occur. The integral was evaluated numerically for a spectrum of $h\upsilon$ at given

60

temperature and hole- and electron-quasi-Fermi energy levels that correspond to specific injected carrier concentrations. A Gaussian fit of each resulting set of calculations yielded the peak energy and a linewidth of the simulated spectrum. A background carrier concentration of 10^{18} cm^{-3} donors had to be assumed in order to reproduce the experimental results best. It may stem from the heavy n doping of the device. The tail parameters σ_{0e} and σ_{0h} were adjusted to obtain the right value of the emission peak linewidth for low excitation powers at room temperature. The best value for both parameters proved to be 49+/-1 meV.

The implication of the value obtained for σ is significant because σ describes the magnitude (standard deviation) of spatial fluctuation of the energy gap. Assuming that this fluctuation is mainly caused by indium fluctuations and using Eq. (1.7), a value $\sigma =$ 49 meV corresponds to an indium fluctuation of about 1.5 %. This value is smaller than the 4 % standard deviation of the indium concentration that was directly extracted for layers with x = 0.2 by HRTEM (Fig. 2). While this disagreement in values could be the result of systematic and statistical uncertainties in the experiments, it could also have other implications.

It is possible that the broadening of the luminescence peak is not due to indium fluctuations over the entire well (being measured by the HRTEM technique) but is rather due to fluctuations between the different recombination centers. This would mean that σ is a measure of the statistical distribution of the "dots" size and indium concentration rather than of the statistical distribution of indium concentration in the entire well. Obviously, the difference in recombination energy from one dot to another would be smaller than that between a dot and a "non-dot" region in the quantum well, and so the σ

61

derived from the bandtails model would be smaller than the fluctuation observed by HRTEM. This picture is consistent with the fact that in the recombination mechanism based on the localization model, almost all the radiative recombination occurs from the dots, rather than the rest of the layer.

The results of the simulation are included in Figures 6 and 7. The correlation of the simulated injected carrier concentration with the current for both figures is made through a best fit of the simulated peak energy with the experimental data. It is evident that the band-tail-recombination model describes closely the basic features of the luminescence properties of sample 1. The model reproduces the anomalous temperature dependence of the emission peak energies in the low current region and the crossover at higher currents.

The physics behind this model explains why the crossover in Fig. 6 occurs. Two temperature-induced luminescence-shifting effects compete with one another. The first is the well-known energy-gap shrinkage with increasing temperature that redshifts the energy with increasing temperature (Eq. (56)). The second effect is the shift of the excited electron (hole) distribution, $\rho_e(E)f_e(E)$ ($\rho_h(E)f_h(E)$), to higher (lower) energies with increasing temperature. This effect is due to the broadening of the Fermi function with temperature and the increase of the DOS with increasing (decreasing) energy and results in a blueshift with increasing temperature. At low excited carrier concentrations, when the carriers fill the states that are still far from the original band edges, the number of available states increases exponentially with energy. Therefore, the shift of the excited electron (hole) distribution to higher (lower) energies with increasing temperature (due to the Fermi function broadening) is large, and the increase in recombination energy due to

this effect dominates over the normal energy gap shrinkage. At high excited carrier concentration, the tails of the DOS become filled, and the number of available states does not increase so strongly with energy anymore. Consequently, the normal temperature-induced energy-gap shrinkage effect becomes dominant.

The model also reproduces the *trends* observed for the linewidths dependence on temperature and current (Fig. 7). It predicts the plateaus at low excitation powers, a slight decrease of the line widths for higher temperatures at moderate excitation levels and the merging of all temperature curves at the high injection currents.

However, the model seriously underestimates the line widths at low temperatures. This might be due to the fact that at low temperature the carriers are not always able to relax to the minimum of the bandtails. That is, they may not have the necessary kinetic energy (temperature) to overcome trapping in local minima in order to find the absolute minimum of the active region. As a result, the linewidth will not decrease as much as the model predicts at low temperatures.

It has been previously argued that the agreement between the experimental data and the band-tails simulation supports the assertion that the recombination mechanism in Sample 1 is dominated by indium fluctuations in the active layer.[5] While this may indeed be the case, it need not be so. Rather, the agreement between the bandtails simulation and the experimental findings supports the assertion that there are tail states like those portrayed in Fig. 10. However, as was previously mentioned, these tails states can result from other sources besides spatial indium fluctuations. Another likely candidate is fluctuations in the QW thickness. Such fluctuations also affect the transition energy via the confinement energy, or even the carrier separation model. Thus, care must be taken

in interpreting this data in terms of carrier localization vs. carrier separation transition models.

4.4 Luminescence intensity as a function of temperature

The general decrease of intensity with temperature observed in Figures 8 and 9 can be explained as follows. At low temperature, the energy available for the free carriers is small, and so the carriers are confined in local potential minima. The carriers are therefore protected from non-radiative recombination centers, such as dislocations, and the structure has a high internal quantum efficiency. As the temperature is raised, the carriers have more energy. Therefore they are less confined and less protected from the non-radiative recombination centers. The resulting internal quantum efficiency is lower, and the luminescence intensity is reduced.

The trend of efficiency as a function of structural parameters is more difficult to explain. One may suggest that the carrier separation may reduce the efficiency in these structures, since the transition rate is reduced. This agrees with the findings of other studies – that the carrier separation in the L_w-series increases with QW thickness (see Chapter 6). Therefore one may expect their efficiency at room temperature to follow the trend indicated in Fig. 8. The same can be said for the color-series, since the carrier separation increases with the redshift of the LED color (as shown in the previous chapter). However, this explanation does not address why at other temperatures this trend is not followed. In addition, while carrier separation reduces the radiative transition rate, it does not necessarily reduce the efficiency. This is because the non-radiative rate is also likely to be reduced by the reduced electron-hole wavefunctions overlap.

4.5 Summary

Usually the luminescence energy is found to increase with excitation density, though sometime a decrease is observed, depending on the sample. A strong increase in transition energy with excitation density is consistent with the carrier separation model, especially when accompanied by a strong reduction in carrier lifetime. This is because the increased carrier concentration screens the electric field in the QW. A weak increase could reflect either a lack of carrier separation, or the presence of a large concentration of doping related free carriers.

Measuring EL as a function of excitation density (current injection) and temperature showed unusual characteristic behavior, such as reversed temperature coefficients at low currents. We were able to reproduce these results using the bandtails model, extending the DOS into the forbidden gap. While this model was originally based on inhomogenous indium distribution in the active layer, it would be valid for any inhomogeneity in properties that affect the transition energy.

The change in luminescence intensity with temperature for the LumiLeds samples was used to compare their internal quantum efficiencies at room temperature. It was found that the efficiency decreased slightly with increasing QW thickness and increasing luminescence peak wavelength. This is considered to be the result of the reduced radiative transition rate associated with the increased carrier separation.
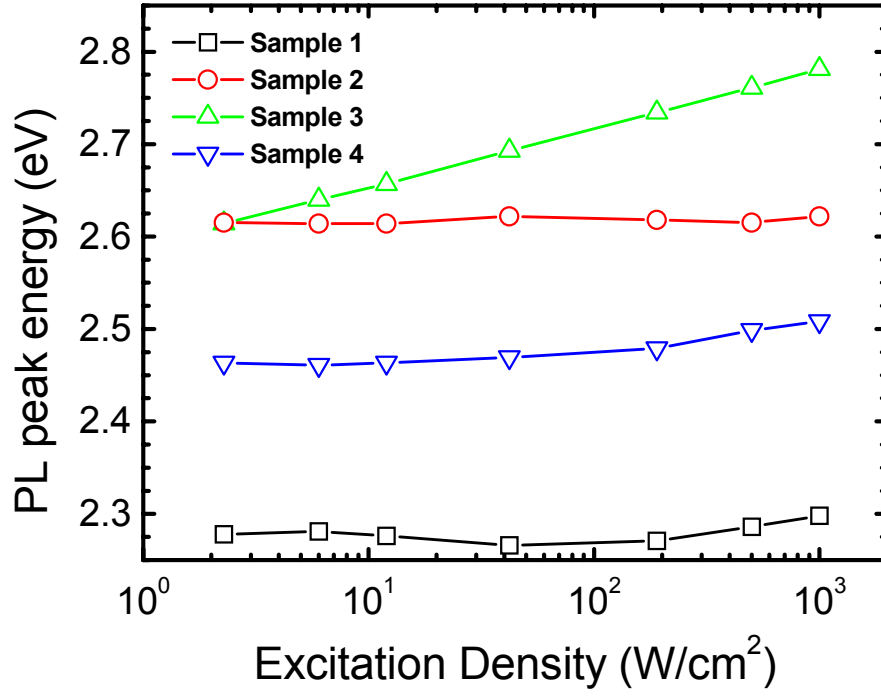
Figure 1: Photoluminescence peak energy as a function of excitation density for samples 1-4 at 300K.
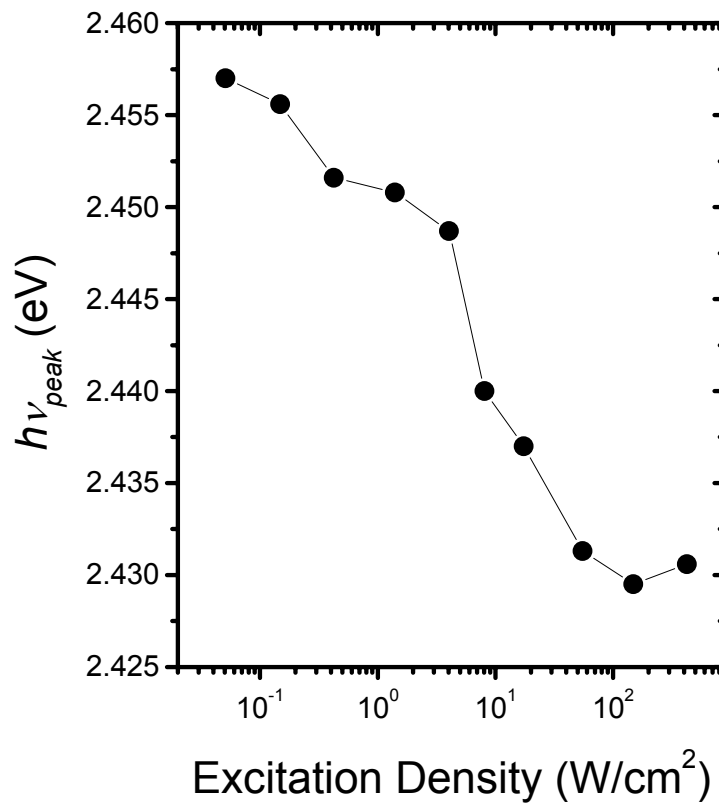
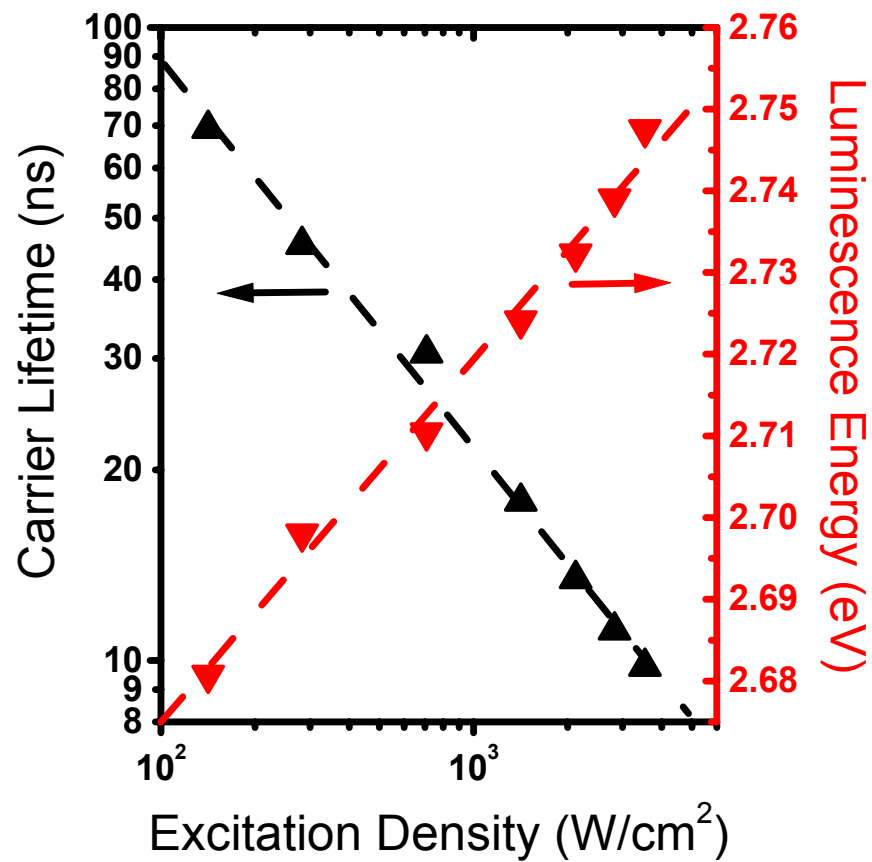Figure 2: Luminescence peak energy as a function of excitation density for sample

LumiLeds 3.

Figure 3: TRPL experiment on sample 3 as a function of excitation density. The carrier lifetime (up-triangle) and luminescence peak energy (down-triangle) are plotted as a function of excitation density.
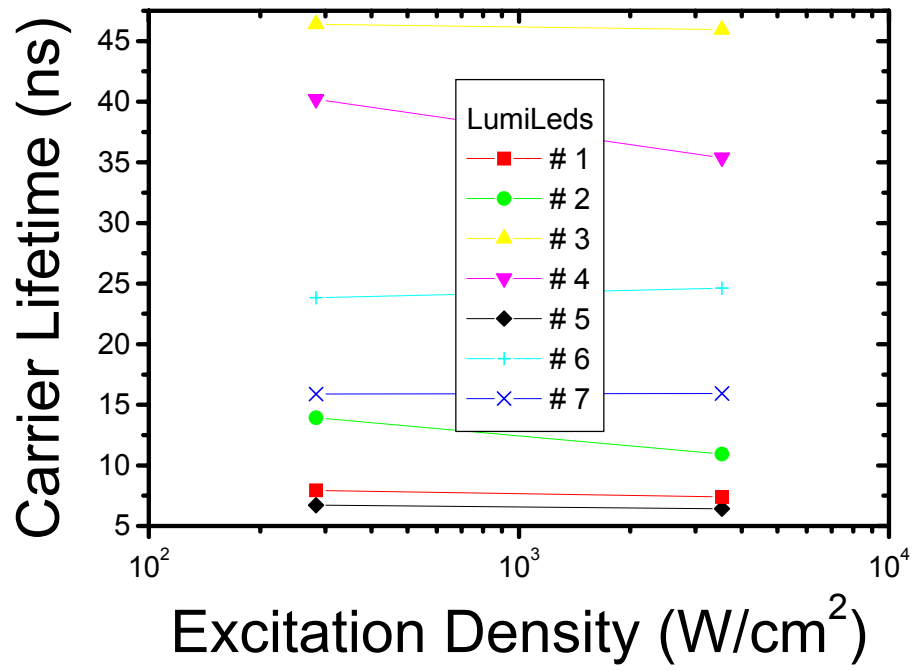
Figure 4: Carrier lifetime as a function of excitation density for MOCVD grown LED QW structures obtained from LumiLeds.
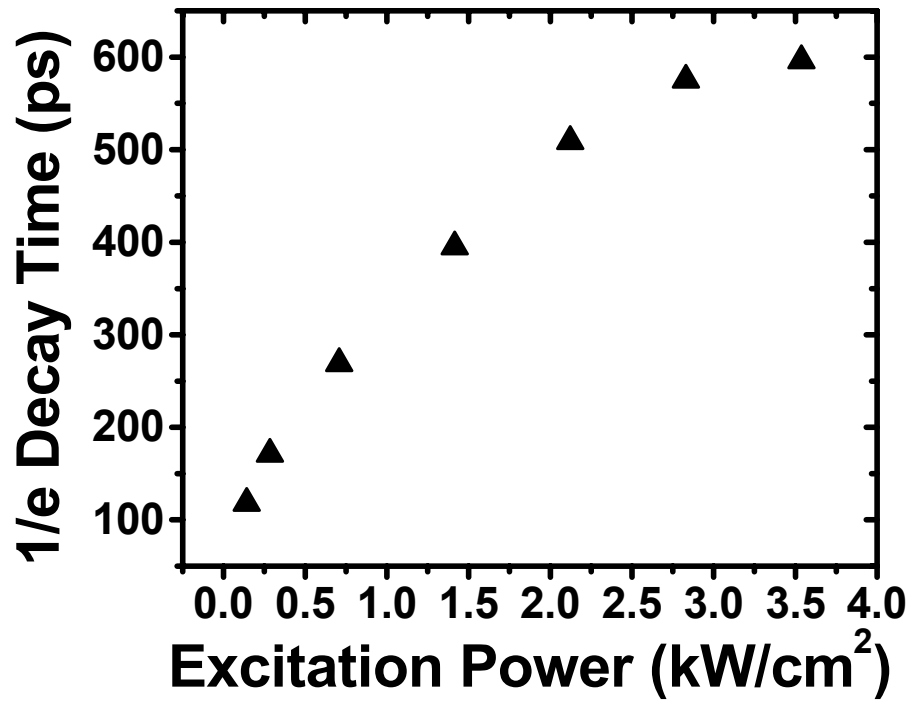
Figure 5: Luminescence decay time as a function of excitation density for an InGaN QW structure (Akasaki sample).
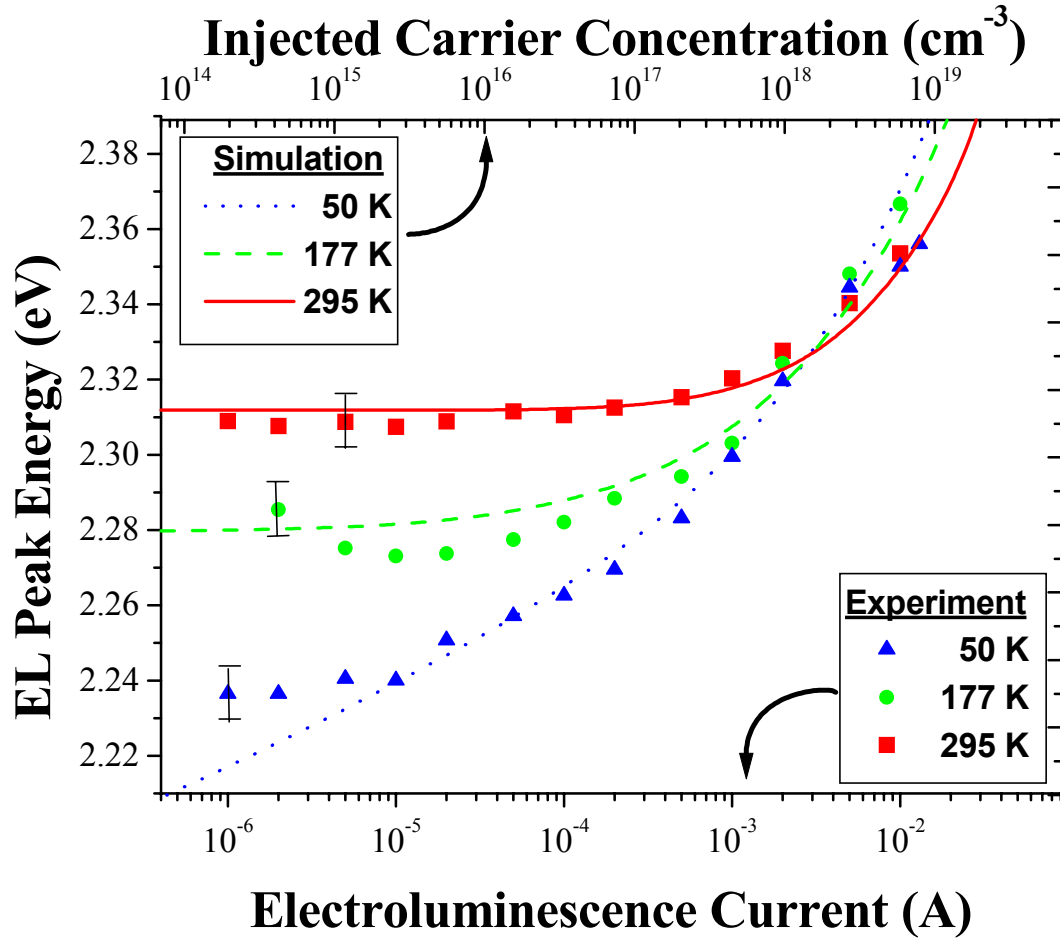
Figure 6: EL peak energy as a function of the EL current for sample 1 at 50, 177 and 300 K. The results of the band tails simulation are also shown as lines.
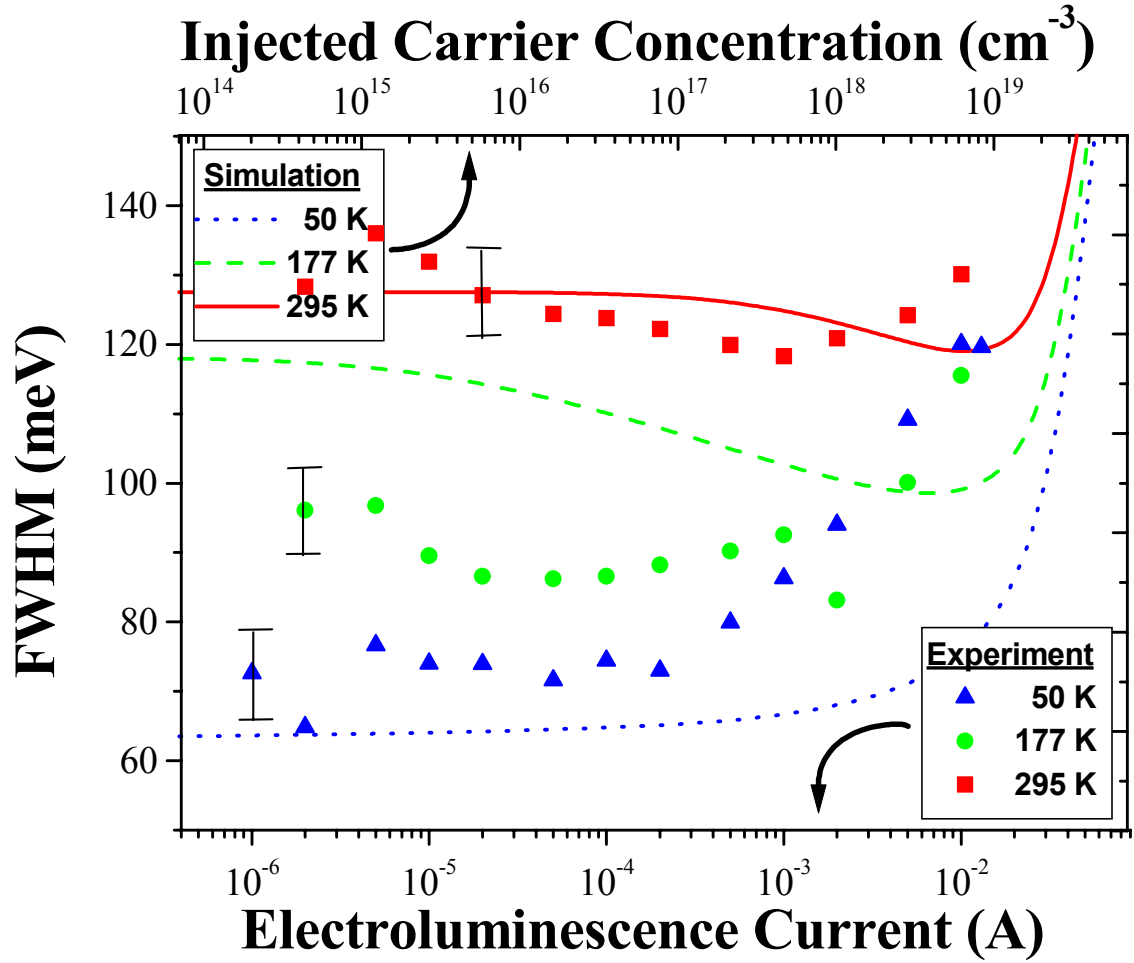
Figure 7: Linewidth of the EL spectra as a function of EL current for sample 1 at 50, 177 and 300 K. The results of the band tails simulation are also shown as lines.
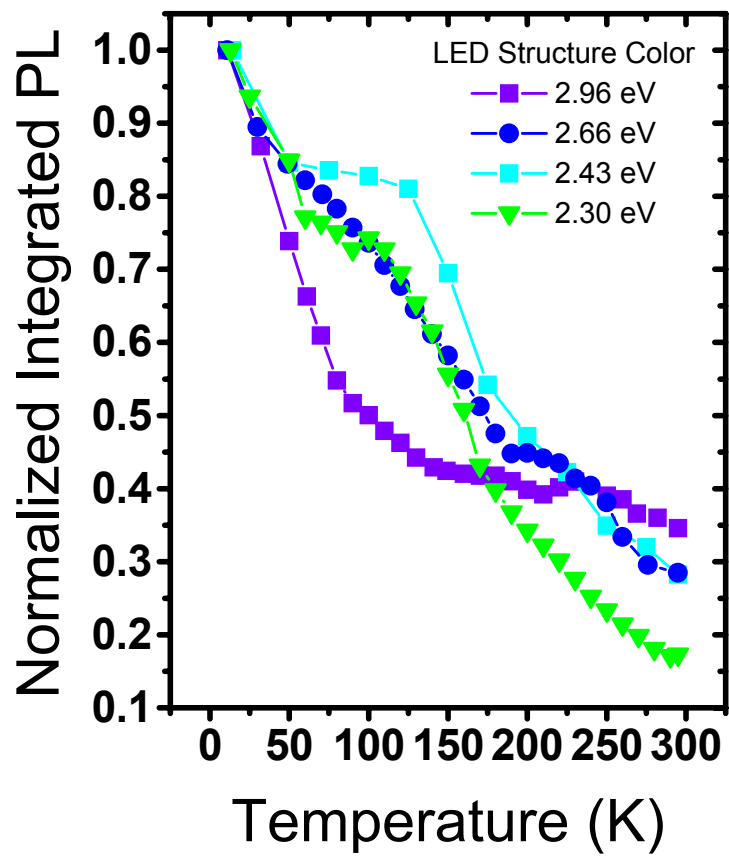
Figure 8: Normalized PL integrated intensity as a function of temperature for the color series.
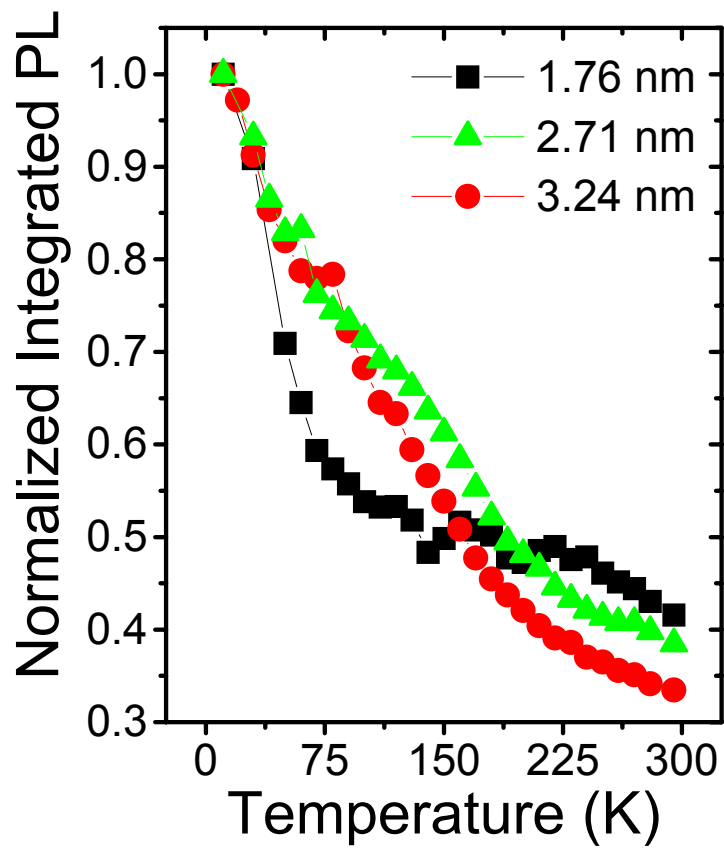
Figure 9: Normalized PL integrated intensity as a function of temperature for the color

series.
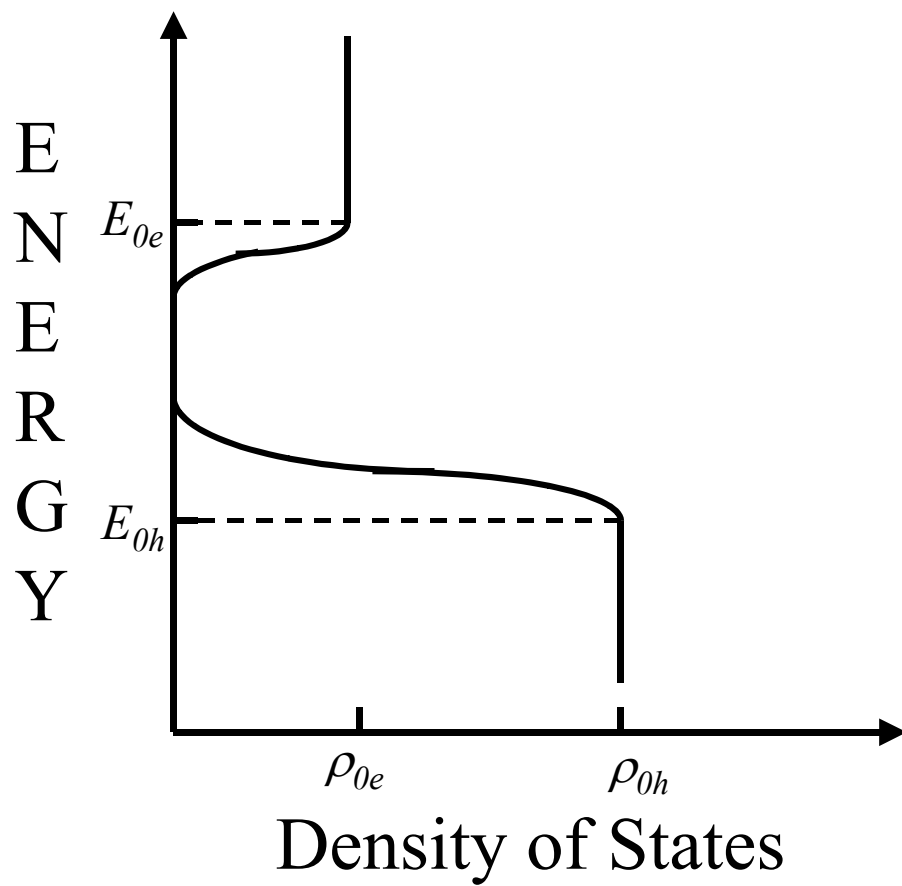
Figure 10: Schematic of the density of states distribution in energy for a quantum well in the band tails model. Not drawn to scale.

4.7 References

[1] T. Takeuchi, S. Sota, M. Katsuragawa, M. Komori, H. Takeuchi, H. Amano and I. Akasaki, Jpn. J. Appl. Phys **36**, L382 (1997).

[2] A. Hangleiter, J. Seo Im, H. Kollmer, S. Heppel, J. Off, Ferdinand Scholz, MRS Internet J. Nitride Semicond. Res. 3, 15 (1998).

[3] J. C. Inkson, J. Phys. C **9**, 1177 (1976).

[4] P.G. Eliseev, P. Perlin, Lee Jinhyun and M. Osinski, Appl. Phys. Lett. **71**, 569 (1997).

[5] N. A. Shapiro, P. Perlin, C. Kisielowski, L. S. Mattos, J. W. Yang and E. R. Weber, MRS Internet J. Nitride Semicond. **5**, 1 (2000).

Chapter 5: Biaxial Strain

In Chapter 4, we showed the value of studying the luminescence as a function of the excitation density and temperature. In this chapter we study the luminescence as a function of biaxial strain. The strain changes the lattice parameter of the crystal, which in turn changes the energy gap. In addition, the strain changes the relative positions of the nitrogen and group-III metal, resulting in a change of the polarization and hence the electric field in the QW. Thus, studying the luminescence as a function of biaxial strain is a promising method to study the effects of the built-in electric field on the radiative transition in these structures.

5.1 Results

5.1.1 GaN epilayer

A HVPE GaN layer grown on sapphire was measured first, in order to provide a reference for the InGaN results. The total thickness of this sample was 377 μm and the diameter of the aperture was 3.449 mm. Figure 1 shows the PL peak energy as a function of applied pressure. The peak redshifts in a linear fashion as the pressure is increased and then returns to its original position as the pressure is released. No significant hysteresis is observed.

This sample was also studied by Raman spectroscopy as a function of applied strain. An Ar^+ laser (λ=515 nm) was used as a source of excitation. The scattered radiation was analyzed by the same spectrometer used for the PL. A backscattering geometry was used to detect the E_2 phonon mode. The Raman peak position is plotted as a function of applied pressure in Figure 2. The peak shifts to lower wavenumbers

(energy) in a linear fashion as the pressure is increased and then returns to its original position as the pressure is released. No significant hysteresis is observed.

5.1.2 InGaN QW structures

Many InGaN QW structures were studied for this work, and the results vary dramatically from one sample to another. The luminescence from these structures redshifts, blueshifts, or shows no significant shift at all with the application of biaxial strain, depending on the sample. In this section we show the results of only two samples, one showing a redshift, and the other a blueshift. These results will be used for general interpretation and model development. In the next chapter we will show the results of systematic biaxial strain studies on InGaN QW structures, and we will use the model developed in this chapter to interpret that data.

The samples chosen for this section are the Akasaki sample and LumiLeds #3. The results of the experiment on the sample obtained from Akasaki, using the 3.449-mm radius holder, are shown in Fig. 3. As in the GaN sample, the PL peak position is observed to decrease linearly with pressure, and then to return to its original position. However, the shift of the luminescence with pressure is significantly weaker than that of the GaN epilayer.

The same holder was used for the experiment on LumiLeds #3. Figure 4 shows the results of this experiment. Here, the PL peak energy *increases* linearly with the applied pressure and then decreases linearly as the cell is depressurized. No hysteresis is observed. Figure 5 shows the PL spectra for the measurements carried out at 0 and 69 bar. Though small compared to the large width of the peak, the blueshift can be observed.

This shift is in the opposite direction to that expected by theoretical calculations for the change of the energy gap.

5.2 Effects of Strain

5.2.1 Energy gap

When a crystal is strained, its electronic band structure changes. In particular, the minimum of the conduction band and the maximum of the valence band shift in energy. Obviously, this change should affect the energy of radiative recombination, assuming that the radiative transition involves the electronic bands in the crystal.

Theoretical models for wurtzite electronic band structures with strain effects have been reported based on the $k \cdot p$ method[1,2,3]. At the band edges (k=0), the shift of electronic bands associated with the valence band was found to be,

$$E_0^{HH} = F_0 , \tag{5.1}$$

$$E_0^{LH} = \frac{G_0 + \lambda_\varepsilon}{2} + \sqrt{\left(\frac{G_0 - \lambda_\varepsilon}{2}\right)^2 + \Delta^2} , \tag{5.2}$$

$$E_0^{CH} = \frac{G_0 + \lambda_\varepsilon}{2} - \sqrt{\left(\frac{G_0 - \lambda_\varepsilon}{2}\right)^2 + \Delta^2} , \tag{5.3}$$

Where

$$F_0 = \Delta_1 + \Delta_2 + \lambda_\varepsilon + \theta_\varepsilon , \tag{5.4}$$

$$G_0 = \Delta_1 - \Delta_2 + \lambda_\varepsilon + \theta_\varepsilon , \tag{5.5}$$

$$\lambda_\varepsilon = D_1 \varepsilon_{zz} + D_2 (\varepsilon_{xx} + \varepsilon_{yy}) , \tag{5.6}$$

$$\theta_\varepsilon = D_3 \varepsilon_{zz} + D_4 (\varepsilon_{xx} + \varepsilon_{yy}) , \tag{5.7}$$

Where E_0^{HH}, E_0^{LH}, and E_0^{CH} are the heavy hole, light hole and crystal-field split hole

valence bands. D_i's are the deformation potentials for wurtzite crystals, ε_i's are the strain

elements, Δ_1 is the crystal-field splitting induced by the hexagonal symmetry of the

wurtzite structure, and Δ_2 is the energy splitting due to the spin-orbit interaction. For the

conduction band, the band edge energy is given by

$$E_0^C = \Delta_1 + \Delta_2 + E_{g0} + P_{c\varepsilon}, \tag{5.8}$$

$$P_{c\varepsilon} = a_{cz}\varepsilon_{zz} + a_{ct}(\varepsilon_{xx} + \varepsilon_{yy}). \tag{5.9}$$

where E_{g0} is the strain free energy gap and a_{cz} and a_{ct} are the conduction band

deformation potentials. Subtracting equation (5.1) from (5.8) gives the energy gap as a

function of strain:

$$E_g = E_0^C - E_0^{HH} = E_{g0} + (a_{cz} - D_1 - D_3)\varepsilon_{zz} + (a_{ct} - D_2 - D_4)(\varepsilon_{xx} + \varepsilon_{yy}). \tag{5.10}$$

Literature values for these deformation potentials for GaN are given in Table 1.1. Figure

6 shows the expected change in the energy gap of GaN as a function of biaxial strain of

the type produced in our experiment. A tensile strain results in a reduction of the energy

gap.

5.1.2 Change in the electric field

The equation used to calculated the electric field in the quantum well was derived in

Chapter 1:

$$E_w = \frac{L_b(P_b - P_w)}{\varepsilon_0\varepsilon_b L_w + \varepsilon_0\varepsilon_w L_b}, \tag{1.6}$$

where L_w (L_b) is the well (barrier) thickness, P_w (P_b) is the zero-field polarization in the

well (barrier), ε_0 is the permittivity of free space, and ε_w (ε_b) is the well (barrier) dielectric

constant. The zero-field polarization is the sum of the spontaneous and piezoelectric

polarizations, as discussed in Chapter 1. The piezoelectric polarization is usually given

by

$$P_{pz} = e_{31}(\varepsilon_{xx} + \varepsilon_{yy}) + e_{33}\varepsilon_{zz} \tag{5.11}$$

where e_{ij} are the electromechanical coefficients. Bernardini and Fiorentini have recently

shown that the spontaneous and piezoelectric polarization of the III-N system are

nonlinear functions of concentration.[4,5] We therefore use the following relationships for

the polarizations in this material system[5]:

$$P_{InGaN}^{sp} = -0.042x - 0.034(1 - x) + 0.038x(1 - x) \tag{5.12}$$

$$P_{GaN}^{pz} = -0.918\varepsilon_{\perp} + 9.541\varepsilon_{\perp}^2 \tag{5.13}$$

$$P_{InN}^{pz} = -1.373\varepsilon_{\perp} + 7.559\varepsilon_{\perp}^2 \tag{5.14}$$

$$P_{InGaN}^{pz} = xP_{InN}^{pz}(\varepsilon_{\perp}) + (1 - x)P_{GaN}^{pz}(\varepsilon_{\perp}) \tag{5.15}$$

where x is the indium fraction, and $\varepsilon_{\perp}$ is the biaxial strain ($\varepsilon_{\perp} = \varepsilon_{xx} = \varepsilon_{yy}$) in the layer. The

biaxial strain in the layer is the sum of the built-in strain $\varepsilon_{\perp}(x)$ and the pressure-induced

strain $\varepsilon_{\perp}(p)$. The pressure-induced strain can be calculated from the pressure in the cell,

using the aperture diameter, sample thickness, and the mechanical constants of the

substrate, as shown in Chapter 3. To calculate the built-in strain, we assume that the

InGaN QW layer is pseudomorphically grown on the GaN layer and that no relaxation

occurs (since the layer is only a few nm thick). The built-in strain induced by the lattice

mismatch can be found from,

$$\varepsilon_{\perp}(x) = \frac{a_{GaN} - a_{InGaN}(x)}{a_{InGaN}(x)} \tag{5.16}$$

where,

$$a_{InGaN}(x) = a_{InN}x + a_{GaN}(1-x), \tag{5.17}$$

where a_{GaN} and a_{InN} are the lattice constants of GaN and InN, respectively. For

consistency, we use the relation provided by the same work[5],

$$a_{InGaN}(x) = 0.31986 + 0.03862x, \tag{5.18}$$

which is in reasonable agreement with the values found in Table 1.1.

Figure 7 shows the theoretical electric field as a function of pressure for the

LumiLeds #3 sample. Note that the magnitude of the electric field is quite large – over 2

MV/cm – which is not unusual at all in InGaN QW structures. The overall field is

reduced by roughly 1-2% due to the application of the tensile biaxial strain with the

pressure cell. The change of electric field produced in the device is relatively small

because the strain applied by the biaxial strain device is much smaller than that produced

by the lattice mismatch.

Figure 8 suggests how a reduction of the electric field in the well is likely to

influence the radiative transition, under the carrier separation model. The reduction of the

electric field causes a reduction in the potential drop separating the electrons and holes.

As a result, the redshift associated with the carrier separation model is reduced, and a

blueshift should be generated.

5.3 Discussion

5.3.1 GaN epilayer

Using equation (5.10) together with equations (2.1-3) allows the calculation of the

expected shift of the energy gap for the HVPE GaN layer, as a function of the cell

pressure in the biaxial strain device. The results of this calculation are plotted in Fig. 1 for

comparison with the experimental data. The redshift of the luminescence of HVPE GaN

sample agrees with the expected shrinkage of the energy gap with tensile strain. It should

be noted that the calculation does not yield the absolute position of the line shown in the

figure, but only its slope. The absolute position is set to be equal to the initial PL peak

energy for zero pressure. There is a reasonable agreement between the theoretical

calculation and the experimental results. The difference between the slopes (~13%) is not

very significant when considering the uncertainty in the values for the elastic compliance

constants and deformation potentials used for the calculation.[6,7]

The shift of the E_2 Phonon mode can be calculated by using an equation similar to

that of the change in the energy gap,

$$\Delta\Omega_\lambda^{E2} = 2a_\lambda^{E2}\varepsilon_{xx} + b_\lambda^{E2}\varepsilon_{zz} \tag{5.19}$$

where a_λ^{E2} and b_λ^{E2} are the deformation potentials for the E_2 phonon mode.[8] Since we

can calculate the expected strain using equations (2.1-3), we can calculate the expected

shift of the Raman line as a function of pressure. The results of this calculation, using the

E_2 phonon mode deformation potentials from Table 1.1, are shown in Fig. 2. Here we

also find a reasonable fit between the experimental and theoretical results. Here again,

the difference between the slopes (~16%) is not unacceptable when considering the

uncertainty in the constants used for the calculation.

However, one should consider possible explanations for why both the PL and

Raman results consistently suggest that the strain in the HVPE GaN layer is somewhat

(10-20%) smaller than theory predicts. One explanation may be that the strain produced

by the bending of the substrate is not fully transferred to the epilayer. This explanation is

consisted with recent results obtained by Kim et al.[9] It was found that the luminescence

pressure coefficient ($dh\nu_p/dp$) depended on the growth condition of the buffer layer. The explanation offered for this phenomenon is that the buffer layer may be softer (reduced elastic constants) than the main GaN layer due to a highly defective crystal structure. Thus, it will act as a strain buffer between the substrate and the epilayer, and it will reduce the PL or Raman pressure coefficient. Our experience with these and other samples suggests that it is not uncommon for as much as 50% of the applied strain to be thus buffered.

5.3.2 InGaN QW structures

The results of the experiment on the sample obtained from Akasaki, using the 3.449-mm radius holder, are shown in Fig. 3. As in the GaN sample, the PL peak position is observed to decrease linearly with pressure. However, the decrease of the PL peak energy with pressure is significantly weaker than that of the GaN epilayer. A calculation of the shift of the energy gap with strain was done for this case also. Since the necessary material constants are not known for InGaN, those of GaN were used. The calculation (also shown in Fig. 3) reveals that the measured decrease of the PL peak position is significantly reduced compared with the behavior expected for a normal band-to-band recombination mechanism.

Several explanations are possible for the decrease of the slope observed in MQW sample 1. First of all, it is possible that the material constants of InGaN are significantly different from those of GaN even at relatively small x values, so that the calculation significantly overestimates ΔE_g. In addition, a strong confinement of carriers, such as in narrow quantum wells or "quantum dots," reduces the shift of the energy gap with

strain.[10] Finally, it is possible that the previously mentioned strain-buffering behavior of the buffer layer is unusually effective in this structure.

However, none of the above explanations can account for the fact that we have observed an *increase* in the PL peak energy of LumiLeds #3 (Figure 4). In an effort to understand this phenomenon, we must take into account the effect of the built-in electric field in the quantum well and use the carrier separation model to describe the radiative transition in this sample.[11]

According to the carrier separation model, the transition energy is reduced due to the separation of the carriers across the potential drop induced by the strong electric field in the well. Neglecting screening by the free carriers, the potential drop across the well is $\sim E_w*L_w$.[12] In the simplest approximation, the change in the radiative transition energy as a function of pressure can be approximated as

$$\frac{dh\nu_p}{dp} \approx \frac{dE_g}{dp} - q \cdot L_w \times \frac{dE_w}{dp}.$$ (5.20)

Calculations based on this model are shown in Fig. 9, where the slopes representing dE_g/dp, $L_w \times dE_w/dp$, and $dh\nu_p/dp$ are plotted next to the experimental data for comparison. Clearly, the $L_w \times dE_w/dp$ term does act to produce a "blueshift" of the luminescence, but the reduction of the energy gap, dE_g/dp, is calculated to yield an even stronger redshift, thus yielding a negative pressure coefficient ($dh\nu_p/dp$).

This is not in good agreement with the experimental results, which yields a positive pressure coefficient. However, there is no other evident explanation for the observed *blueshift* of the luminescence under *tensile* strain. To remain in the confines of this rather simple model, possible sources of error must be considered. The two likely

sources of discrepancy are the energy gap pressure coefficient (dE_g/dp) and the electric field pressure coefficient (dE_w/dp).

While there is a significant level of uncertainty about the deformation potentials (dE_g/dp) found in the literature, none exists that is so small as to explain the discrepancy observed in Fig. 9 (i.e., one that will produce a significant blueshift). The observation of reduced redshift for GaN in this work is most likely due to a reduced actual strain applied (as compared to the calculated strain) to the layer, possibly due to strain buffering in the buffer layer. This reduced strain would therefore reduce dE_w/dp just as much as it did dE_g/dp and the effect on $dh\nu_p/dp$ would be canceled out.

Thus we are left with one possible culprit – the electric field-pressure coefficient, dE_w/dp. One possible error might be in the method used for calculating the electric field. It has been proposed that a macroscopic potential drop develops across the MQW region due to the piezoelectric effect. This additional potential drop, which should be opposite in direction to that of the QW, would further reduce the electric field in the QW. When taking this effect into account, it is possible to reproduce, and even significantly exceed the experimental blueshift. However, for such a macroscopic potential drop to exist, the mobile carriers must be restrained from moving across the MQW region, allowing for a Fermi level-offset between the two sides.

To test this hypothesis, a similar LED InGaN QW structure from LumiLeds with contacts to the n- and p-layers was obtained. Then the potential difference between the contacts was measured as a function of biaxial strain. A change in potential drop across the contacts would signify that a real offset in the Fermi levels is being established across the active layer. None was observed. In addition, PL as a function of biaxial strain was

measured both with the contacts open and with the contacts shorted. In both cases a similar blueshift was observed. Thus the blueshift is shown to be independent of any strain induced macroscopic potential across the MQW region.

The last resort, therefore, is to question the electromechanical coefficients used for equation (1.6). The pressure coefficient of the electric field, dE_w/dp, is directly proportional to the difference between the electromechanical coefficients of the barrier layers (GaN) and well layers (InGaN). That is,

$$\frac{dE_w}{dp} \propto \left(\frac{dP_b}{dp} - \frac{dP_w}{dp} \right) \propto \left(e_{i,j}^b - e_{i,j}^w \right). \tag{5.21}$$

While these coefficients have been established experimentally for GaN, all that there is for InN are theoretical calculations. Since these calculated values generally suggest only a small difference between GaN and InN, the pressure coefficient of the electric field in the quantum well is small. However, if the theoretical calculation of InN is off by only a factor of two, the difference between the electromechanical coefficients and the pressure coefficient of the electric field will increase by about a factor of 5.

Indeed, recently there have been several reports suggesting that while the experimental dE_w/dp in AlGaN/GaN QW structures follows the theoretical prediction, there is a very large discrepancy in the case of InGaN/GaN QW structures.[13,14] Vaschenko et. al.[14] in particular concluded that the only way to reproduce the experimentally observed pressure dependence of the electric field is by considering a strong dependence of the piezoelectric constants on strain. While we have included a nonlinear term for the piezoelectric polarization calculated by Fiorentini, it is still significantly too small to explain our results and those by others who investigate the pressure dependence of the electric field in InGaN QW structures. The stronger strain

dependence calculated by Shimada et. al. also falls short of reproducing experimental results.[14, 15] Since the as-grown InGaN QW already contains very significant strains, the true electromechanical constants of the InGaN QW in our samples may already be quite different than those calculated in literature. This is the most likely reason for the discrepancy between the model and the experimental results.

5.4 Summary

The luminescence of HVPE GaN and InGaN QW structures was measured as a function of biaxial strain. The GaN luminescence redshifted in a way consistent with the expected shrinkage of the energy gap. This, together with a Raman shift consistent with theory, gives us a measure of confidence in our ability to induce a predictable amount of tensile biaxial strain in epitaxial layers. At the same time, we see evidence that the amount of strain induced in the epitaxial layer can be reduced by factors such as a mechanically weak buffer layer.

The InGaN QW structures can exhibit either a redshift or a blueshift as a function of tensile biaxial strain. We attribute the observed blueshift to a decrease in the electric field as a function of tensile strain coupled to the carrier separation transition model. Under this model, the luminescence is redshifted by a potential drop across the QW that can be reduced by the reduction of the electric field. However, detailed calculations revealed a significant discrepancy between theory and our experimental observations.

We considered several causes for the discrepancy such as reduced deformation potentials and the existence of a macroscopic potential across the QW structure. However, a detailed investigation leads us to conclude that the source for the discrepancy lies in the values used for the electromechanical coefficients of InGaN (InN). These

values were derived from theoretical calculations and have not been established

experimentally. In addition, recent experimental results reported in literature cast serious
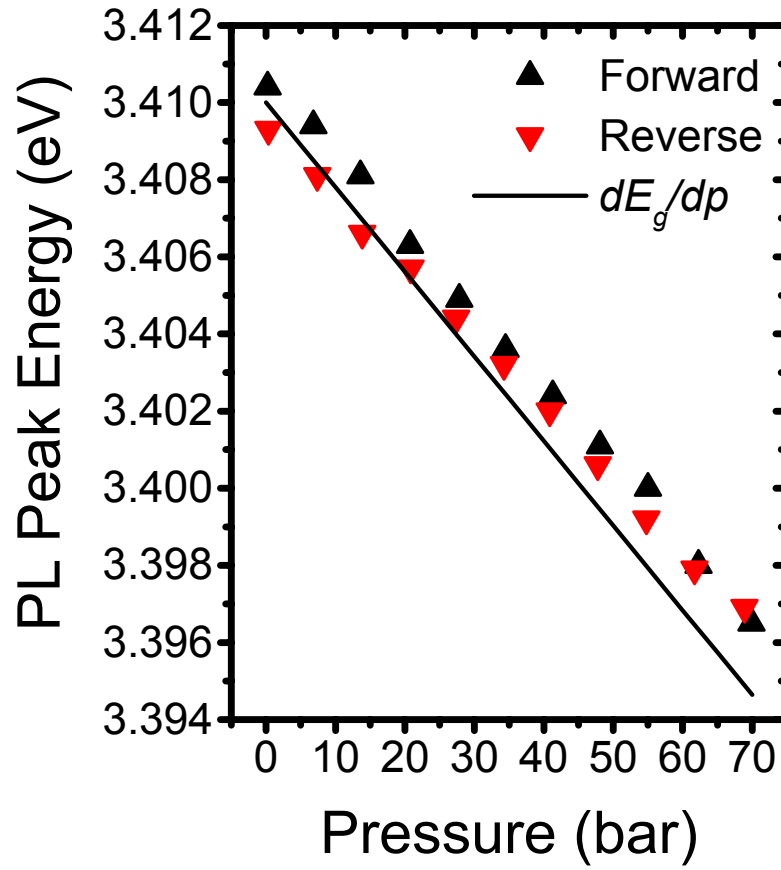
doubt over their accuracy.[14,15]

Figure 1: PL peak energy as a function of pressure for an HVPE grown GaN epilayer on Sapphire. The slope calculated using Equations (5.10) and (2.1-3) is shown for comparison.
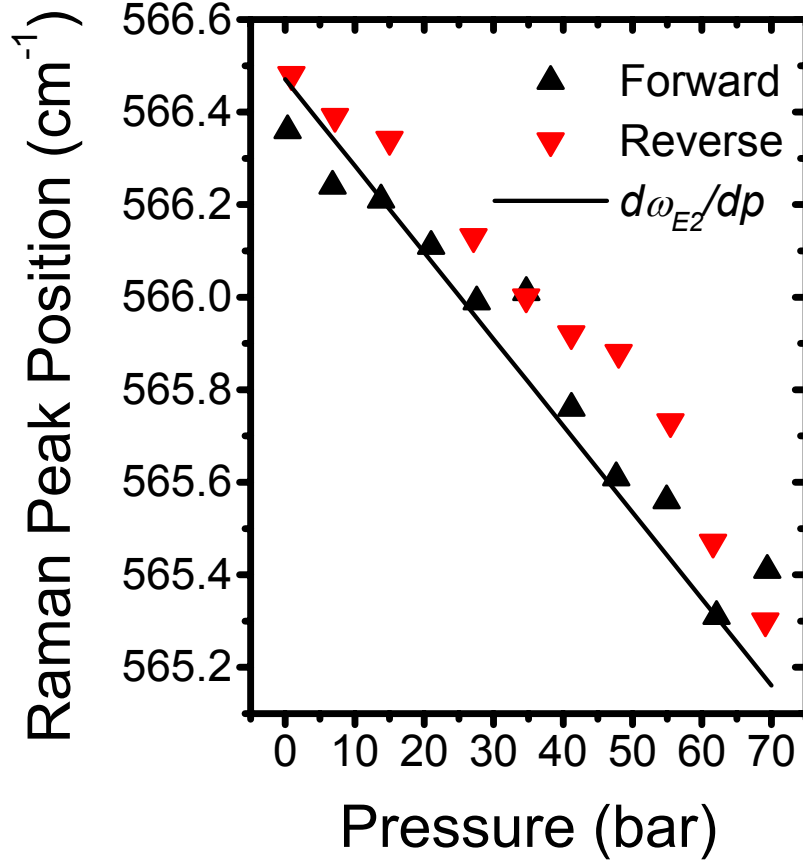
Figure 2: Raman peak position as a function of pressure for an HVPE grown GaN epilayer on Sapphire. The slope calculated using Equations (5.19) and (2.1-3) is shown for comparison.
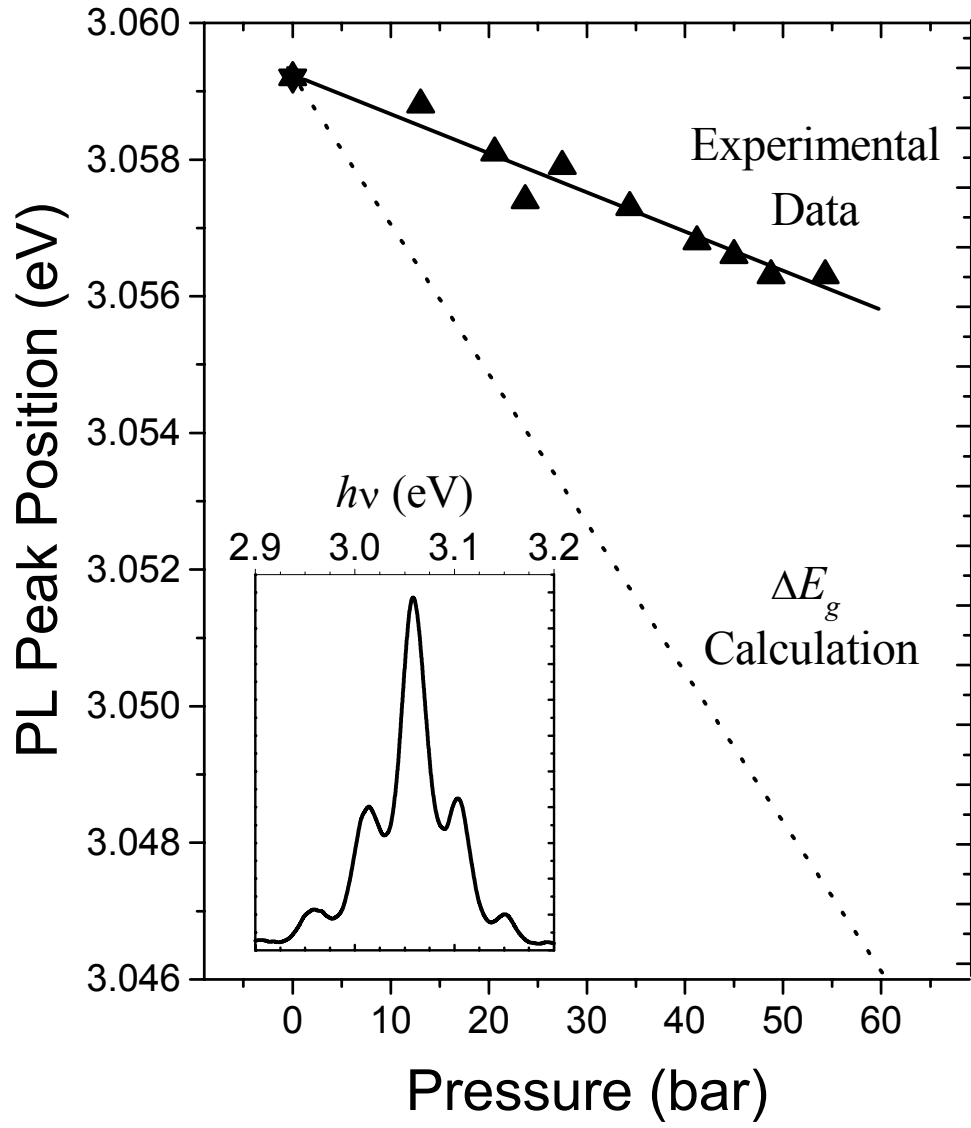
Figure 3: PL peak energy as a function of the cell pressure in the biaxial strain device for Akasaki's sample. The spectra were measured while the pressure was increased (✳), and after the release of the pressure (☐). The solid line is a linear fit to the experimental data, and the dotted line gives the calculated shift of the energy gap. The insert shows the PL spectrum for a pressure of 0 bar.
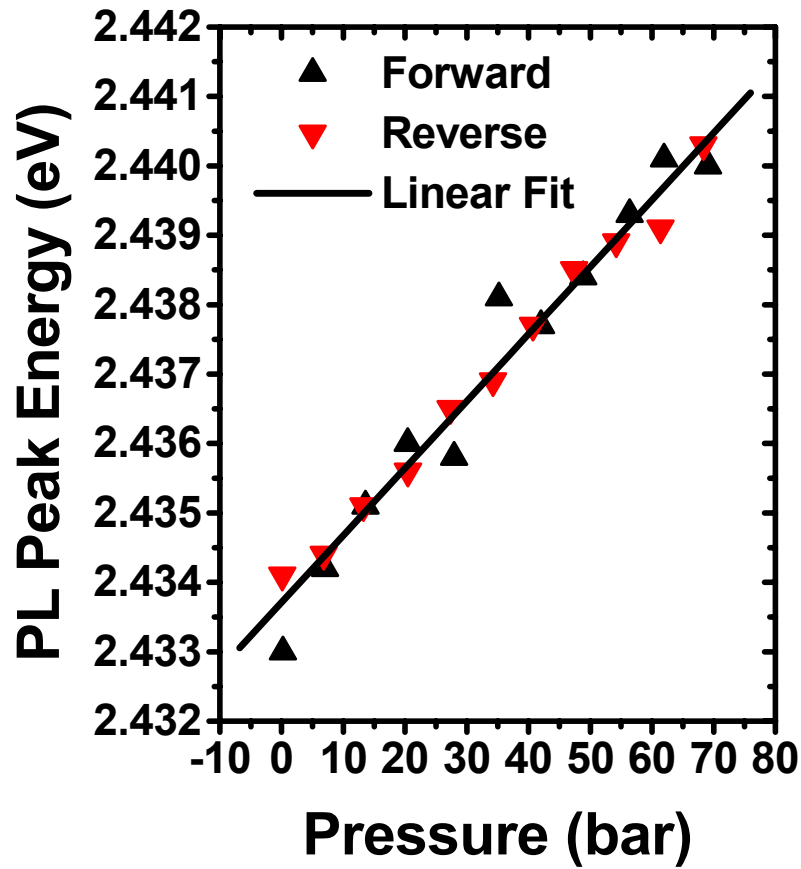
Figure 4: PL peak energy of LumiLeds #3 as a function of the cell pressure in the biaxial strain device. ⬆ represent spectra measured as the pressure was increasing, while ⬇ represent those measured during the depressurization. The dashed line represents a linear fit of the combined data.
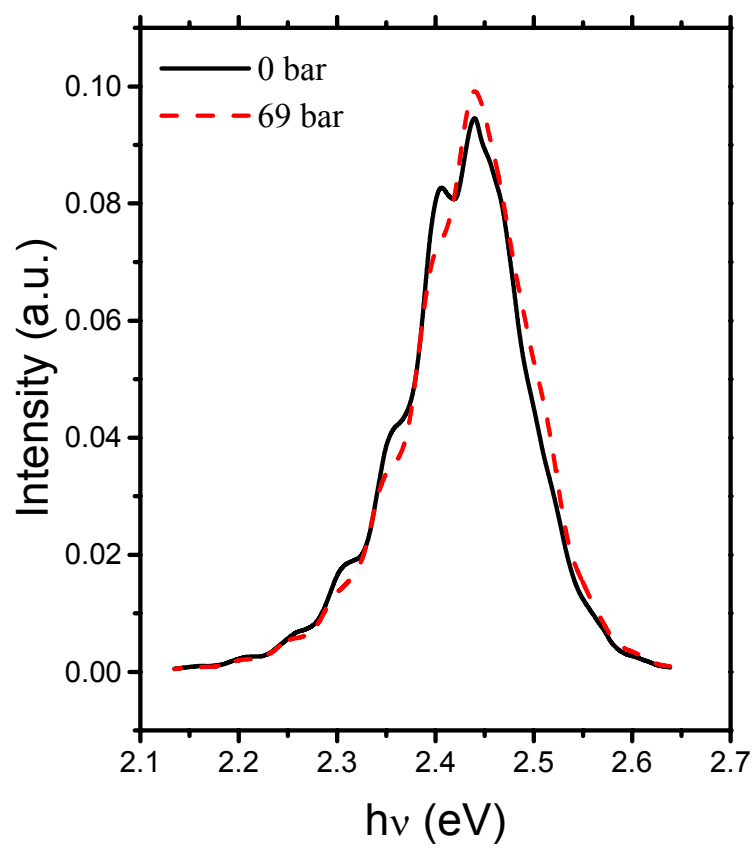
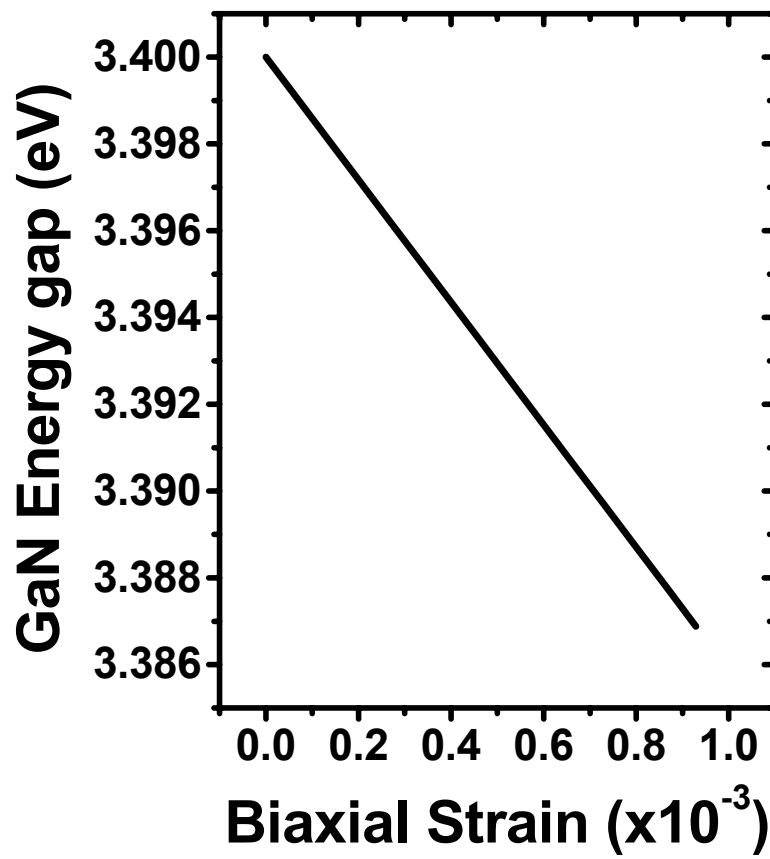Figure 5: PL spectra of LumiLeds #3 at pressures of 0 (solid) and 69 (dash) bar.

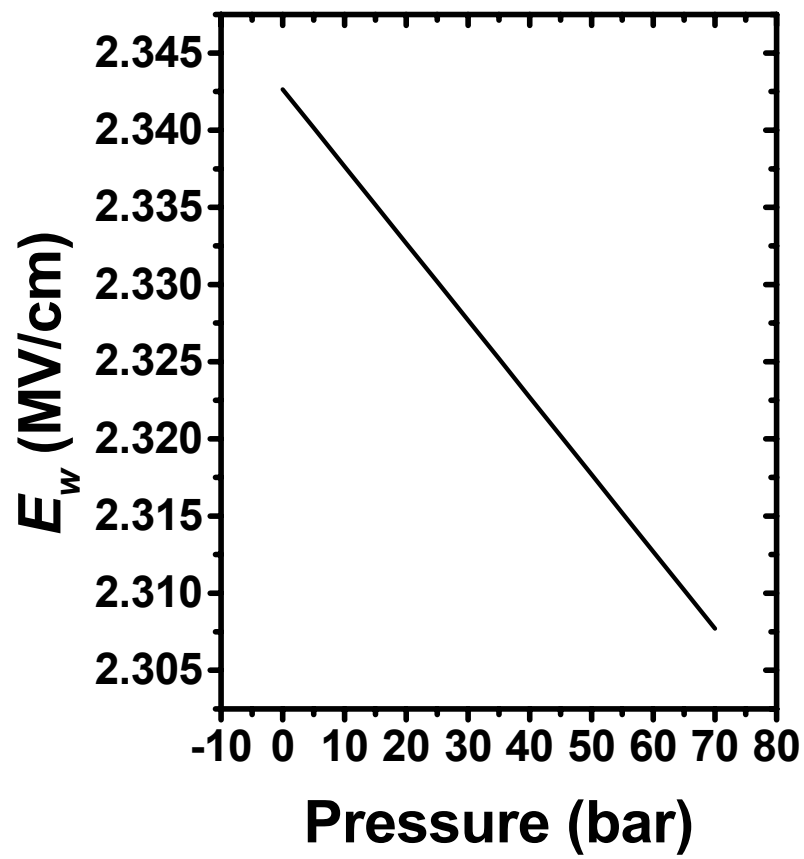Figure 6: GaN Energy gap as a function of biaxial strain.

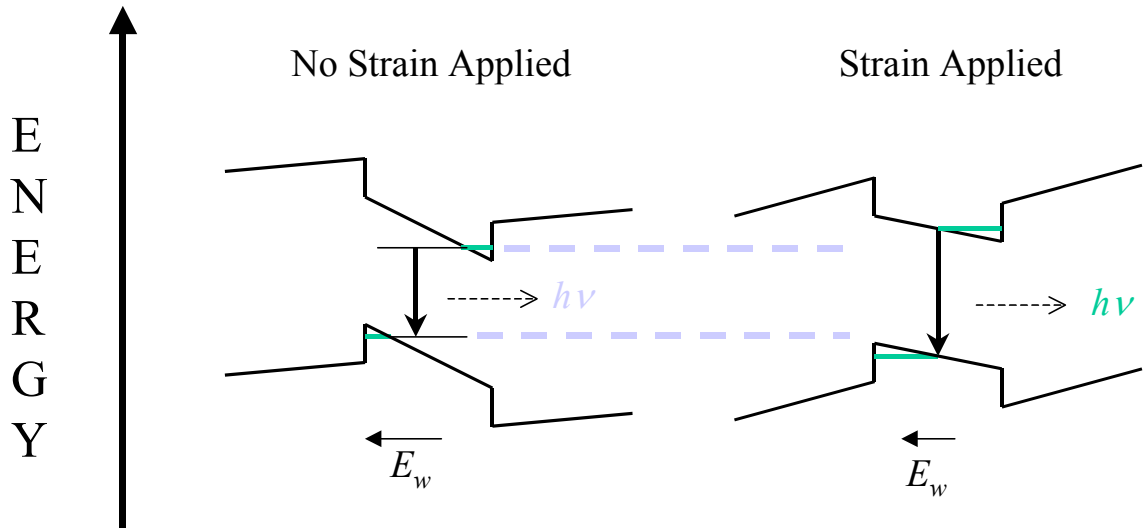Figure 7: Calculated electric field in the well as a function of pressure for the LumiLeds #3 sample.

Figure 8: Sketch explaining the experimentally observed blueshift in InGaN QW structures. The applied tensile biaxial strain reduces the magnitude of the electric field in the QW, thus reducing the potential drop across the QW. As a result, the redshift associated with the carrier separation model is reduced, and a blueshift is generated.
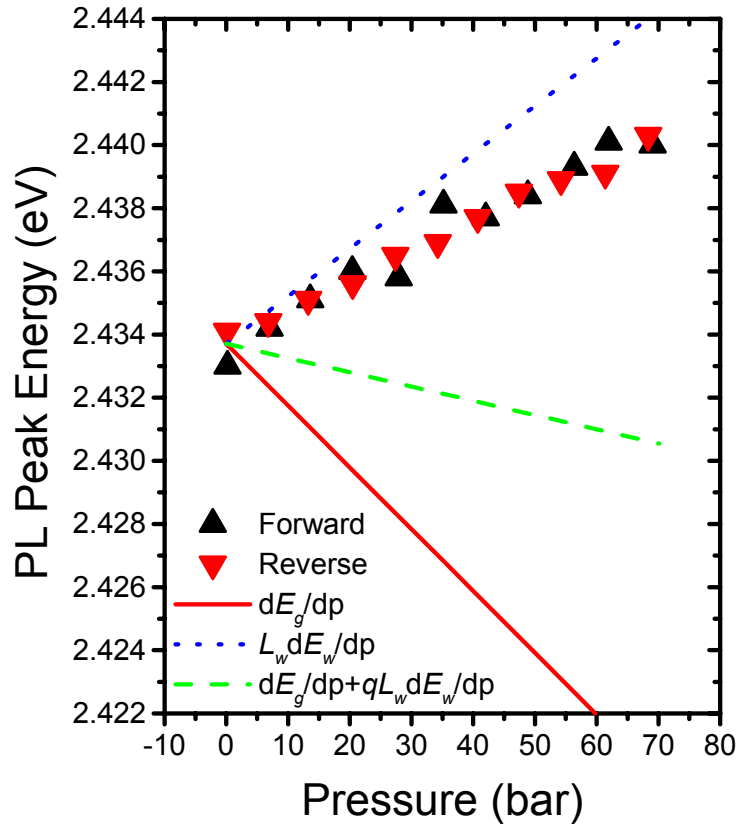
Figure 9: Comparison between experimental energy-shift of the luminescence the theoretical shift. The solid line represents the expected shift of the energy gap, the dotted line represents the energy shift associated with the change in the electric field of the quantum well, and the dashed line represents the summation of the two effects.

5.6 References

[1] G.L. Bir and G.E. Pikus, *Symmetry and Strain-Induced Effects in Semiconductor* (Wiley, New York, 1974).

[2] M. Suzuki, T. Uenoyama and A. Yanase, Phys. Rev. B **52**, 8132 (1995).

[3] Y.M. Sirenko, J.B. Jewon, K.W. Kim, M.A. Littlejohn and M.A. Stroscio, Phys. Rev. B **53**, 1997 (1996).

[4] F. Bernardini, and V. Fiorentini, Phys. Rev. B **64**, 085207 (2001)

[5] V. Fiorentini, F. Bernardini, and O. Ambacher, Appl. Phys. Lett. **80**, 1024 (2002)

[6] C. Kisielowski, Semiconductors and Semimetals **57**, 275 (1999).

[7] I. Vurgagtman, J. R. Meyerm, L. R. Ram-Mohan, J. Appl. Phys. **89**, 5815 (2001)

[8] F. Demangeot, J. Frandon, M. A. Renucci, O. Briot, B. Gil, and R. L. Aulombard, Solid State Commun. **100**, 207 (1996).

[9] Y. Kim, N. A. Shapiro, H. Feick, R. Armitage, E. R. Weber, Y. Yang, and F. Cerrina, Appl. Phys. Lett. **78**, 895 (2001).

[10] W. Paul, Semiconductors and Semimetals **54**, 1 (1998).

[11] T. Takeuchi, S. Sota, M. Komori, M. Katsuragawa, H. Takeuchi, H. Amano, and I. Akasaki, Jpn. J. Appl. Phys. **36**, L382 (1997).

[12] It is worth pointing out that in the pure *quantum-confinement Stark effect* (QCSE), the transition energy scales with the square of the electric field. However, in this case the electric field is so strong that the confinement is between the barrier on one side and the slanted energy gap on the other (as is depicted in Fig. 8). This situation is better described the *Franz-Keldysh effect*, where the Density of States "tunnels" into the

forbidden gap region. In this tunneling scenario, the transition energy has a linear dependence on the electric field. (See for example "The Physics of Low-Dimensional Semiconductors" by J. H. Davis, Cambridge University Press, 1998, p.258) Since the overall change in the electric field is small, the change in the confinement energy of the "triangular well" is neglected in this approximation.

[13] P. Perlin, I. Gorczyca, T. Suski. P. Wisniewski, S. Lepkowski, N. E. Christensen, A. Svane, M. Hansen, S. P. DenBaars, B. Damilano, N. Grandjean, and J. Massies, Phys Rev. B **64**, 115319 (2001).

[14] G. Vaschenko, D. Patel, C. S. Menoni, N. F. Gardner, J. Sum, W. Goetz, C. N. Tome, and B. Clausen, Phys. Rev. B **64**, 241308 (2001).

[15] K. Shimada, T. Sota, K. Suzuki, and H. Okumura, Jpn. J. Appl. Phys. **37**, L1421 (1998).

Chapter 6: Systematic biaxial strain studies

A question that remains unanswered is the discrepancy between the two InGaN samples that were discussed in the previous chapter. The two have roughly the same QW thickness (~3nm) and not very different indium concentrations (12 & 15.9%) and yet one showed a redshift of the luminescence with applied pressure and the other showed a blueshift. Could it be that the less than 4% difference in indium between the two produces such a large change in dE_w/dp or is another term responsible for this difference? In this chapter, the effective carrier separation parameter (L_r) is introduced to explain this and results obtained with other InGaN QW samples.

6.1 Results

6.1.1 Luminescence energy

In order to find a relationship between the luminescence pressure coefficient ($dh\nu_p/dp$) and other device characteristics, systematic studies of InGaN QW structures were carried out. The luminescence pressure coefficients for L_w-series (LumiLeds 5-7) are shown in Figure 1 as a function of well thickness. These samples are identical in all parameters except for the QW thickness because only the QW growth time was varied during growth. The results show an increasing luminescence pressure coefficient with QW thickness. Figure 2 shows the results for the *x*-series (UCSB 1-3) as a function of indium concentration. These samples should be identical except for the indium content in the QW because only the indium flux was changed during the growth. The results show an increase of the luminescence pressure coefficient with increasing indium content. Figure 3 shows the results for the *color*-series (LumiLeds 1-4) as a function of peak

luminescence energy. There is a general, though not completely consistent, increase of the luminescence pressure coefficient with decreasing LED luminescence energy. For all of the above measurements, the 3.449mm-radius aperture sample-holder was used.

6.1.2 Carrier lifetime

In addition to measuring PL, the TRPL as a function of biaxial strain was also measured for select samples. The carrier lifetimes and luminescence energies as determined by TRPL for the L_w-series are shown in Figure 4. The carrier lifetimes increase exponentially and the luminescence energies decrease linearly with the well thickness. Figure 5 shows the carrier lifetime of Lumileds sample 5 as a function of pressure in the biaxial strain device, using the 3.175mm-radius aperture sample-holder. The lifetime decreases with increasing pressure and then increases back to its original value as the pressure is released. No hysteresis is observed. The slope of this shift is regarded as the "carrier lifetime-pressure coefficient."

LumiLeds samples 6 and 7 were also characterized, using this same method and settings. Both samples showed a similar decrease of lifetime with applied strain. The carrier lifetime-pressure coefficient of the L_w-series (LumiLeds 5-7) is shown in Figure 6. We see a trend of increasing pressure coefficient with increasing QW thickness. However, it should be noted that the "relative" change of the lifetime is roughly the same in all samples (~4-6%). That is, the reduction in lifetime is roughly proportional to the original lifetime of the sample.

6.2 Effective electron-hole separation

Instead of assuming that the carrier separation is equal to the quantum well thickness, one should consider the case of reduced carrier separation. In the case of a perfectly homogenous well, with abrupt interfaces and no carrier screening, there may indeed be an effective carrier separation equal to L_w.[1] However, in samples with a high density of doping-induced carriers, the electric field will be significantly screened and as a result, the carrier separation will be reduced effectively.[2] In addition, indium-rich nano-clusters may generate potential minima in the center of the quantum well that inhibit carrier separation.[3] Finally, as shown in the HR-TEM results in Chapter 2, the interfaces are not perfectly abrupt, especially for the case of narrow QWs with high indium concentration. As a result, the carrier separation limit imposed by the barrier is likely to extend some distance into the so-called QW region.

The luminescence pressure coefficient should therefore be described by,

$$\frac{dh\nu_p}{dp} \approx \frac{dE_g}{dp} - q \cdot L_r \times \frac{dE_w}{dp},$$ (6.1)

where L_r is introduced as the effective electron-hole (e-h) separation parameter. Eq. (6.1) is the effective definition of L_r for the purpose of this work. Roughly speaking, L_r represents the spatial distance between the electron and hole that are involved in the radiative transition. Since the electrons and holes are in quantized states, one can think of this as being the distance between the intersections of the quantized states and the energy gap, as is suggested by the sketch in Fig. 5.8. L_r is expected to have values somewhere between 0 and L_w, depending on the strength of the electric field and the microstructure of the QW.

By using equation (6.1), the experimentally observed pressure coefficient

$(dh\,\nu_p/dp)$ can be used together with the theoretical energy gap and electric field pressure

coefficients $(dE_w/dp, dE_g/dp)$ to calculate L_r. Figure 7a shows the resulting L_r as a

function of quantum well thickness, L_w, for a large number of InGaN QW structures. The

dashed black line represents a linear fit of the scattered data, and the solid line represents

$L_r = L_w$. A trend of increasing L_r with L_w can be observed. However, it is obvious that

there are some problems with these results, since L_r is consistently larger than L_w.

How can this inconsistency be accounted for? There are two factors in Eq. (6.1)

that could stand closer inspection. As mentioned in section 5.3.1, the calculated dE_g/dp is

usually larger than the experimentally observed redshift of the luminescence. This

behaviour is attributed to buffer layer related strain buffering. Since in PL experiments

on InGaN QW structures a GaN-related peak is often observed, this peak can be used to

calibrate the strain that is produced in the layer. Using this peak as a calibration, it was

found that the actual strain produced in these samples was usually about 35-50% smaller

than that calculated from the strain equations in Chapter 2. Therefore, the strain

calculated by Eqs. (2.1-3) is multiplied by a correction factor of 0.58 to reflect the real

strain induced by a given pressure. This factor is the "strain correction factor" (SCF).

Figure 7b shows the strain-calibrated L_r values as a function of QW thickness. A

significant improvement in the *trend* is shown, but the L_r values are still significantly too

large.

As discussed in Section 5.3.2, the theoretical electric field-pressure coefficient

(dE_w/dp) appears to be significantly smaller than experimental results suggest. The most

likely source of error is the inaccurate electromechanical coefficients of InGaN.[4,5,6,7]

That is, the actual difference between the electromechanical coefficients of GaN and InGaN appears to be much larger than that calculated by Bernardini.[4,5] To correct for this, the theoretical difference between the electromechanical coefficients of GaN and InGaN is multiplied by the "electromechanical correction factor" (ECF). The ECF increases the calculated electric field-pressure coefficient (dE_w/dp). It is set to ensure that for no sample is the effective carrier separation (L_r) larger than the QW thickness (L_w). An ECF of ~ 4.0 is found to be necessary in order to achieve $L_r = L_w$ for the sample with the largest L_r/L_w in Fig. 7b (UCSB 3). It should be noted that this is the minimum necessary correction factor, as even this sample may have L_r smaller than L_w.

Figure 8 shows these "piezo-corrected" L_r values as a function of QW thickness. As was designed by the choice of the ECF, no sample now exhibits $L_r > L_w$ (solid line). For discussion purposes, the circle, square, dashed circle, and dashed square mark Sample 3, LumiLeds #2, LumiLeds #3, and the Akasaki sample, respectively. While these L_r values may not be exact, they allow comparison between one sample and another. For example, this analysis yields L_r values of 0.83nm and 1.83nm for the Akasaki and LumiLeds #3 samples, respectively, even though both have L_w ~ 3nm. Thus, the reason the first exhibits a redshift and the second a blueshift is at least partly due to a difference in L_r between the two, not only the difference in dE_w/dp. This observation fits with the fact that Akasaki's sample had heavily doped barriers ($\sim 5*10^{18} cm^{-3}$). The free carriers generated from this doping could screen the electric field, reducing the effective carrier separation, L_r.[2]

Another notable feature of Fig. 8 is that the trend implies that for very narrow QWs (< 1.0-1.5nm) no carrier separation is to be expected. This is reasonable because

for such narrow QWs the barriers do not allow significant carrier separation, and the confinement energy may be larger than the electric field induced potential drop. With L_r ~ 4.75nm, Sample 3 exhibits the largest effective carrier separation. This may partly explain why this sample shows the highest sensitivity to carrier screening in Chapter 4. While the exact values for L_r are very sensitive to the value of the ECF, the relative values and the above trend are not, as can be seen by a comparison of Figs. 7b and 8.

What does this ECF of ~ 4.0 actually mean? It means that the effective difference between the electromechanical coefficients of GaN and InGaN (InN) needs to be about four times larger than that offered by the theoretical calculations of Fiorentini and Bernardini[4,5], in order to produce an agreement with the experimental results. While this large deviation from theoretical calculations may seem surprising, it is not inconsistent with other results reported in literature.[6,7,8] Also, while the difference is increased by a factor of four, the actual electromechanical coefficients of InN need only increase by about a factor of two. While even this may seem like a large error, it should be remembered that until recently it was widely believed that the energy gap of InN was around 2.0 eV, while now it has been strongly confirmed to be only about 0.8 eV (a factor of 2.5 smaller!).[9,10]

6.3 Discussion

6.3.1 Luminescence energy

Figure 1 shows that the luminescence pressure-coefficient ($dh\,v_p/dp$) increases with increasing QW thickness. This would be the natural expectation. In the presence of a strong electric field, the barriers to the quantum well limit the extent of separation of

the carriers. Therefore as the quantum well thickness increases, the carrier separation increases. The analysis discussed in section 2 yields L_r values of 1.07, 2.14, and 1.99 nm for LumiLeds 5-7, respectively. These values correspond to relative separation parameters (L_r/L_w) of 0.61, 0.66, and 0.73, respectively.

This conclusion is in general agreement with the luminescence energy measured for these samples using TR-PL (Fig. 4). The luminescence energy decreases linearly with the increasing potential drop between the electrons and holes. Extrapolating the luminescence energy data to zero well width yields transition energy of 3.18 eV. Using the separation related potential drop of $\sim E_w*L_r$, and the calculated value of the electric field for these structures $\sim$1.6 MV/cm, we can calculate $L_r/L_w \sim$ of 0.81, 0.85, and 0.82 for these samples, respectively. While far from a perfect agreement, we note that the separation parameters agree within $\sim$20%, even using these rather simple and very different methods of evaluation.

From Fig. 3, it is seen that the luminescence pressure coefficient increases with increasing indium content. This trend is not so much the result of a varying L_r as a function of indium concentration as much as it is the result of a varying dE_w/dp. According to Equation (5.14), increasing the indium content should increase dE_w/dp due to the increased difference between the electromechanical coefficients of the well and barrier layers. Waltereit et. al. used these results to calculate new electromechanical coefficients for InN. [8]

However, his approach requires assuming that $L_r = L_w$ for all samples. As discussed in section 2, there are reasons to believe that L_r can be smaller from L_w due to heavy doping, interface diffusion, and possible indium inhomogeneity. In addition, as is

shown in Fig. 3, there are cases where a sample with higher indium content and the same QW thickness can exhibit a smaller luminescence pressure coefficient (compare LumiLeds #2 and #3). The analysis of section 2 yields L_r values of 2.81, 3.01, and 4.22 nm for UCSB #1-3, respectively. These values correspond to relative separation parameters (L_r/L_w) of 0.67, 0.72, and 1.00, respectively. This observation is consistent with the trend observed in the HR-TEM results of Chapter 2 of increased indium segregation and broadened interface for higher indium content QWs. Both of the above factors would tend to decrease the effective carrier separation.

From Fig. 4, it is seen that as the QW is designed to emit luminescence at longer wavelengths, the luminescence-pressure coefficients also increase. This is consistent with the results for the L_w-series and x-series because longer wavelength emissions require larger QWs and/or greater indium content, as can also be seen from Table 2.1. The one exception to this trend is that LumiLeds #2 ($h\nu_p\sim2.66$ eV) has a larger luminescence-pressure coefficient than LumiLeds #3 ($h\nu_p\sim2.43$ eV). However, LumiLeds #3 has a higher indium concentration and so is more likely to contain indium inhomogeneities or broadened interfaces that would reduce the effective carrier separation. In fact, our model calculations yield $L_r\sim2.75$nm for LumiLeds #2 and only $L_r\sim1.83$nm for LumiLeds #3, even though both have L_w=3.02nm.

It is interesting to note that the greatest internal quantum efficiencies tend to be reached for LEDs designed to emit around blue-green (500 nm)[11], where this work finds evidence for significant carrier separation and large carrier lifetimes. This suggests that the carrier separation is not strongly deleterious to the operation of these devices, even though we would expect that the reduced oscillator strength of the transition would

reduce the internal quantum efficiency. This might be due to the fact that the non-radiative lifetime is equally reduced by the carrier separation. It is possible that while the carriers are separated along the direction of the electric field, they are localized in the perpendicular direction such that they are protected from non-radiative centers associated with the high density of threading dislocations in the structure.

6.3.2 Carrier lifetime

Figure 4 shows that the carrier lifetimes of LumiLeds 5-7 increase with increasing QW thickness. This is consistent with previous reports in literature.[12] As the QW thickness increases, the carriers are permitted greater separation within the QW region. As a result, the e-h wavefunction overlap is reduced, and the carrier lifetime is increased. Since the recombination effectively requires the tunnelling of electrons across this separation, the carrier lifetime should increase approximately exponentially[2,13] with the carrier separation. Therefore, we use the relationship,

$$\tau \approx \tau_0 e^{L_r / L_0}, \tag{6.2}$$

to fit the experimental data, where L_0 is introduced as a normalization parameter. L_0 contains in it such information that also affects the transition rate (i.e. wavefunction shape). From a fit to the experimental data, using $L_r = 0.75 L_w$, a zero-separation lifetime (τ_0) of 2.5ns and L_0 of 1.05nm are obtained. The value $\tau_0 = 2.5$ns is in general agreement with similar findings by Massies et al.[14]

Figure 5 shows that the carrier lifetime decreases with applied pressure. From Eq. (6.2) this indicates a decrease in the carrier separation and/or a broadening of the wavefunction. This is not surprising when we remember that the application of pressure reduces the electric field in the QW by as much as ~ 6% (using ECF of ~ 4.0 with Fig.

5.7). Since the electric field is the driving force for the carrier separation, one would expect the effective carrier separation to be reduced, hence reducing the carrier lifetime.

Figure 6 shows an exponentially increasing carrier lifetime-pressure coefficient ($d\tau/dp$) with increasing QW thickness. The reason for this will become apparent with the following analysis. Taking the pressure derivative of equation (6.2) yields,

$$\frac{d\tau}{dp} = \tau \cdot \frac{d\left(L_r / L_0\right)}{dE_w} \cdot \frac{dE_w}{dp},$$ (6.3)

where one may consider $d(L_r/ L_0)/dE_w$ to represent the polarizability of the carriers in the QW. It is the response of the relative electron-hole distribution to the electric field. In first approximation, the parameters on the right-hand side of equation (3) (dE_w/dp, $d(L_r/ L_0)/dE_w$) may be expected to be relatively constant in these samples. Thus, since the lifetime increases exponentially with the QW thickness, one should observe an exponential increase in the lifetime pressure coefficient, as it is in fact observed in Fig. 6.

Figure 8 shows the resulting $d(L_r/ L_0)/dE_w$, which can be obtained by dividing the carrier lifetime-pressure coefficient by the lifetime and the individually calculated dE_w/dp terms (taking substrate thickness into account). The polarizability decreases weakly with increasing L_w. The reason for this behavior is not immediately obvious and requires further exploration. It is even possible that the polarizability is more a function of L_r than of L_w, since L_r also varies in these samples.

6.4 Summary

The effective carrier separation parameter, L_r, was introduced in order to interpret the luminescence and carrier lifetime pressure coefficients in InGaN QW structures. To enable a reasonable analysis, the results had to be corrected for strain relaxation and

inaccurate electromechanical coefficients. The necessary ECF of 4.0 shows a large deviation from the theoretically calculated electromechanical coefficients. This analysis reveals that the reason why one sample exhibits a redshift and the other a blueshift is at least partly due to difference in effective carrier separation.

Systematic studies show that the luminescence-pressure coefficient generally increases with QW thickness, indium concentration, and peak emission wavelength. Detailed analysis showed that L_r generally increases with QW thickness, but can decrease with indium concentration, possibly due to indium inhomogeneity or reduced effective interface abruptness. In addition, L_r can decrease significantly due to high doping in the sample.

The carrier lifetime decreases with applied tensile biaxial strain. This behavior is attributed to a decrease in the effective carrier separation or wavefunction broadening in the quantum well. A systematic study as a function of quantum well thickness revealed an exponential relationship between the lifetime-pressure coefficient and the quantum well thickness. This behavior is adequately explained as stemming from the exponential relationship between the overall lifetime and carrier separation. A slight reduction in "polarizability" with increasing QW thickness requires further investigation.
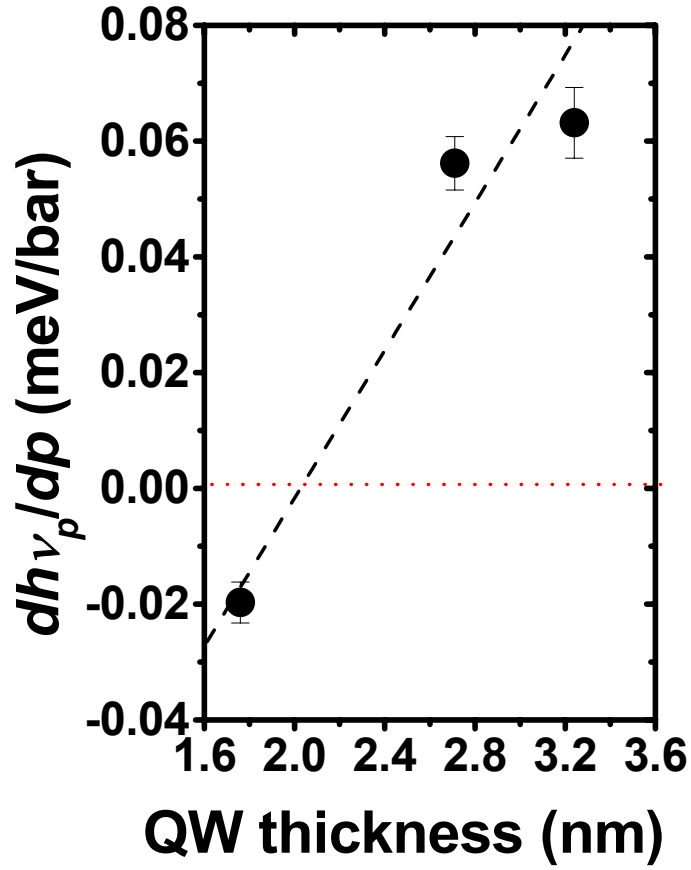
Figure 1: Luminescence pressure coefficient vs. well thickness for LumiLeds samples 5-7. The dashed line is a linear fit of the data, and the dotted line marks the transition from a redshift to a blueshift of the luminescence with the application of biaxial strain.
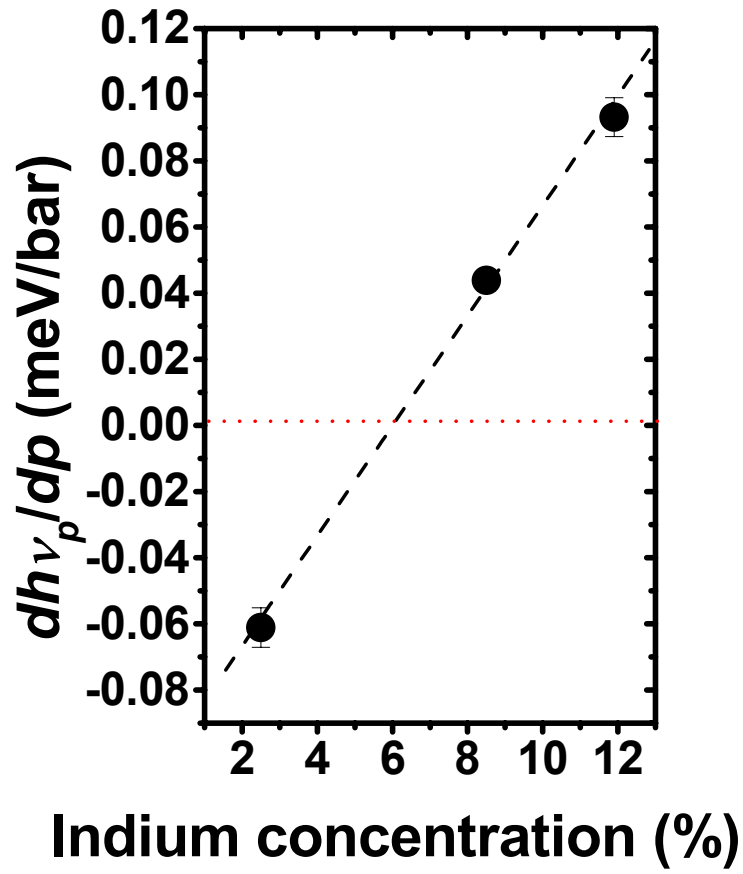
Figure 2: Luminescence pressure coefficient vs. indium concentration for UCSB samples 1-3. The dashed line is a linear fit of the data, and the dotted line marks the transition from a redshift to a blueshift of the luminescence with the application of biaxial strain.
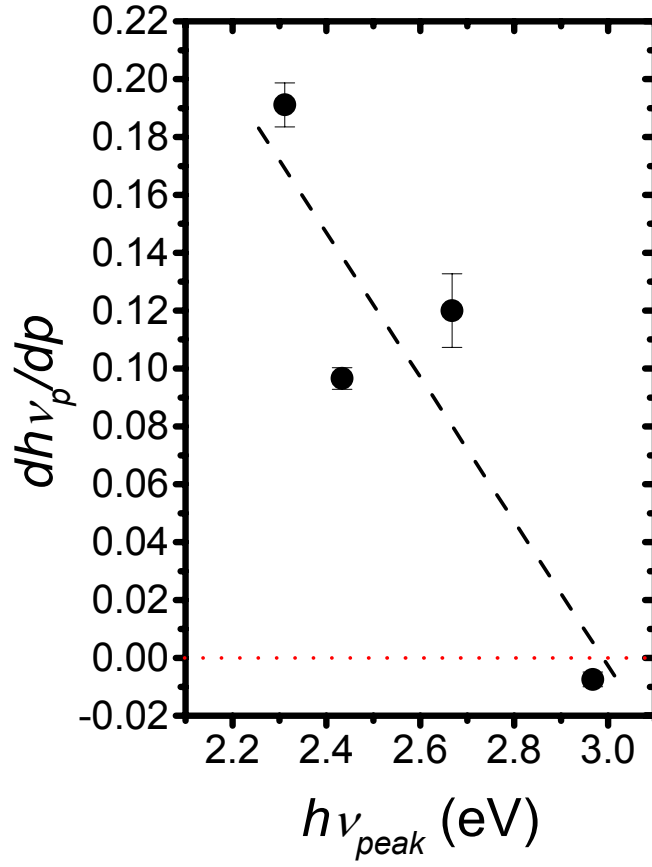
Figure 3: Luminescence pressure coefficient vs. emission energy for LumiLeds samples 1-4. The dashed line is a linear fit of the data, and the dotted line marks the transition from a redshift to a blueshift of the luminescence with the application of biaxial strain.
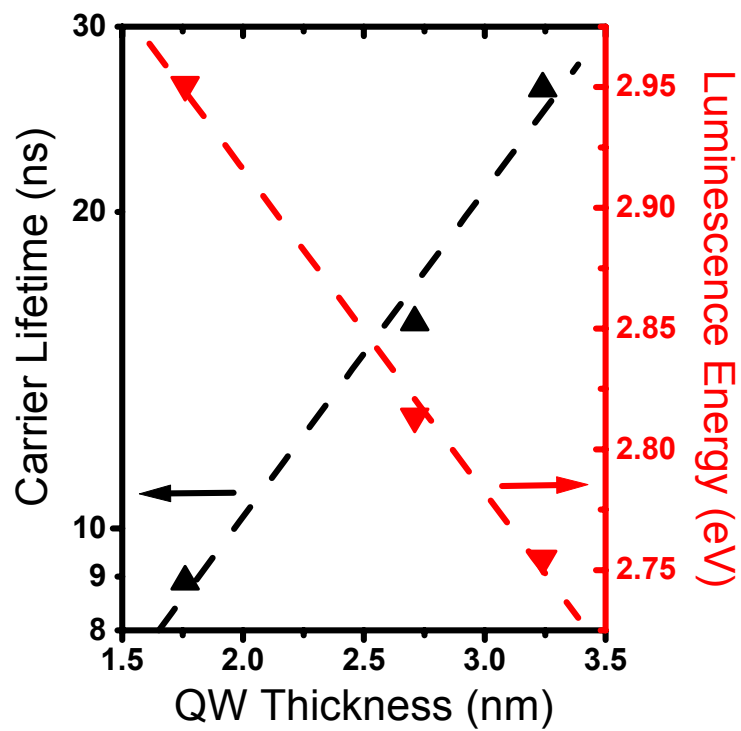
Figure 4: Carrier lifetime (up-triangles) and luminescence energy (down-triangles) vs.
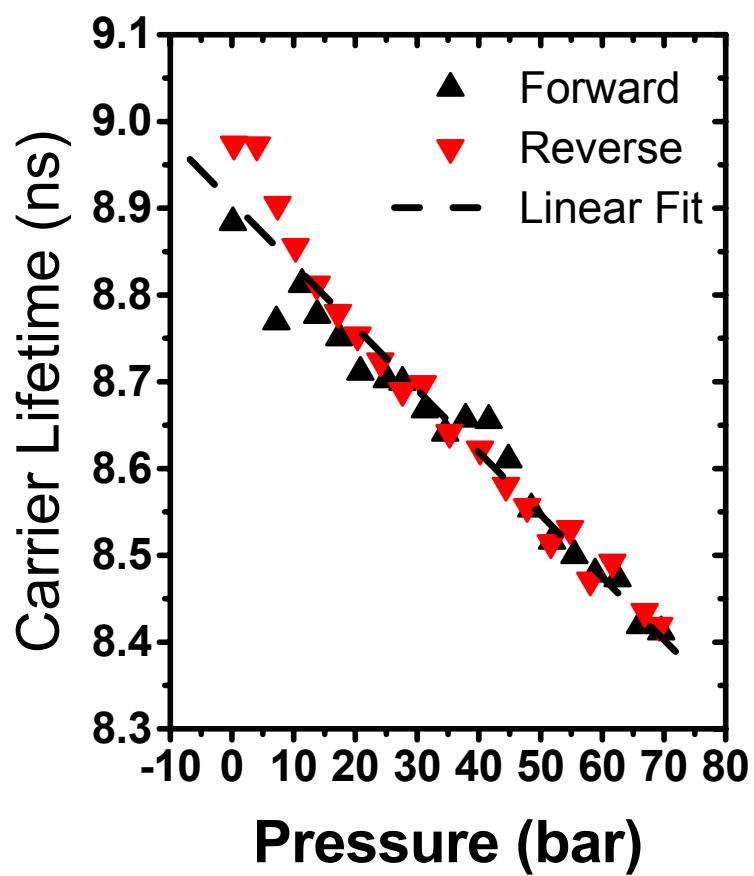
QW thickness for LumiLeds samples 5-7.

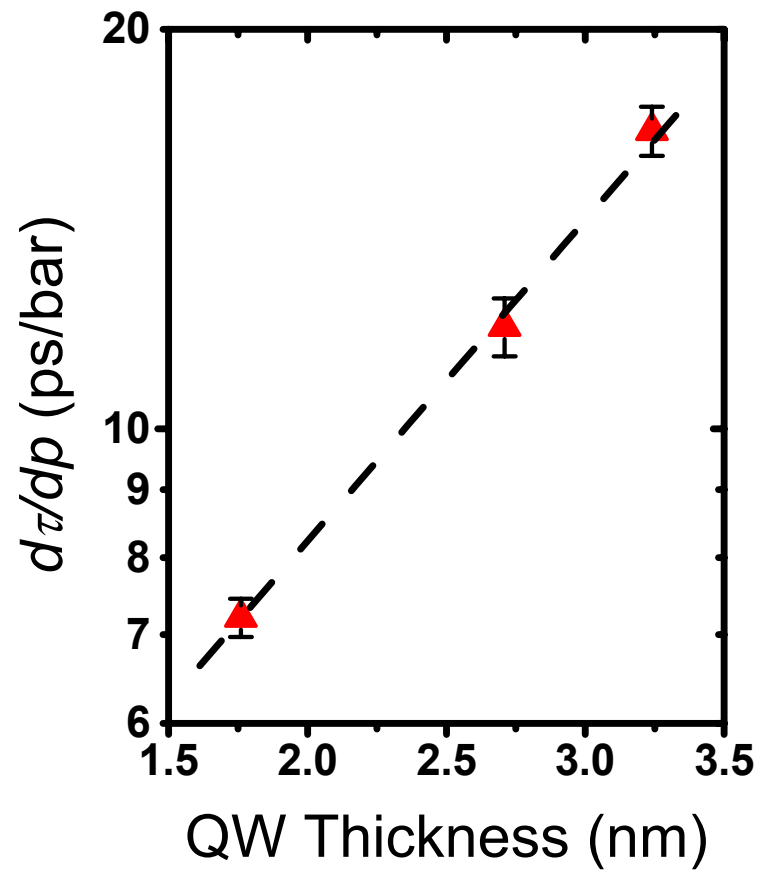Figure 5: Carrier lifetime of LumiLeds sample 5 as a function of pressure in the biaxial strain device.

Figure 6: Carrier lifetime pressure coefficient as a function of the QW thickness for LumiLeds samples 5-7.
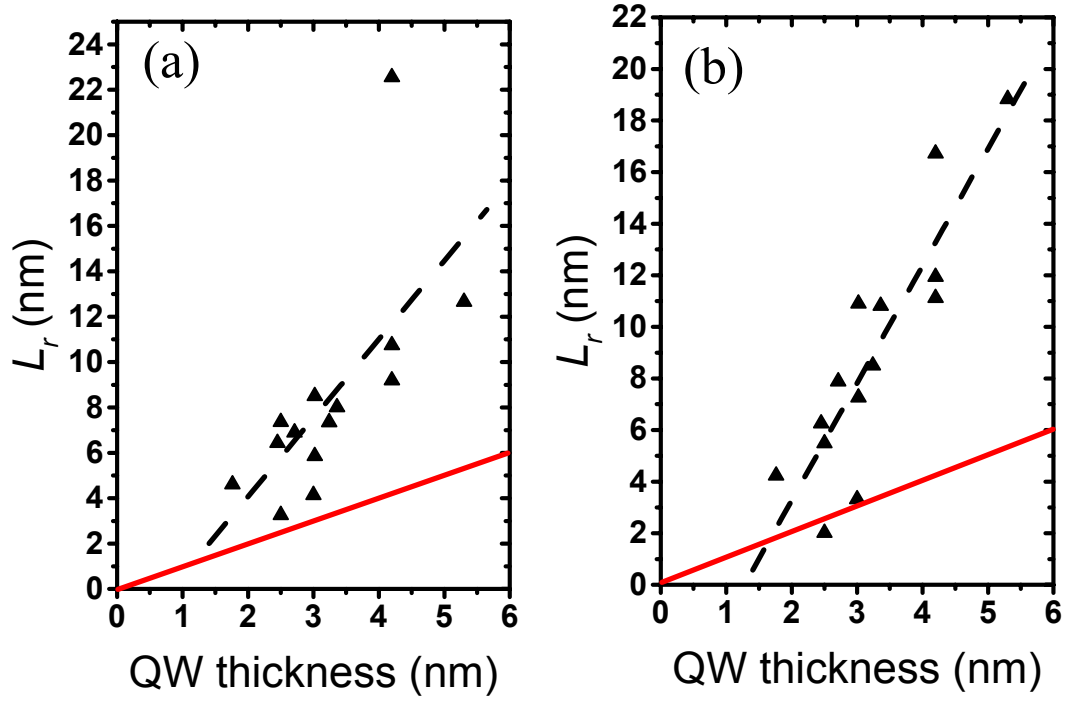
Figure 7: (a) Effective carrier separation, L_r, as calculated by equation (6.1), as a function of QW thickness. Every data point marks the value obtained for a different InGaN QW structure. The dashed line represents a best linear fit of the data, whereas the solid line represents the $L_r = L_w$. (b) Correction produced by strain calibration, using a 0.58 strain factor to obtain actual strain produced in the QW structure.
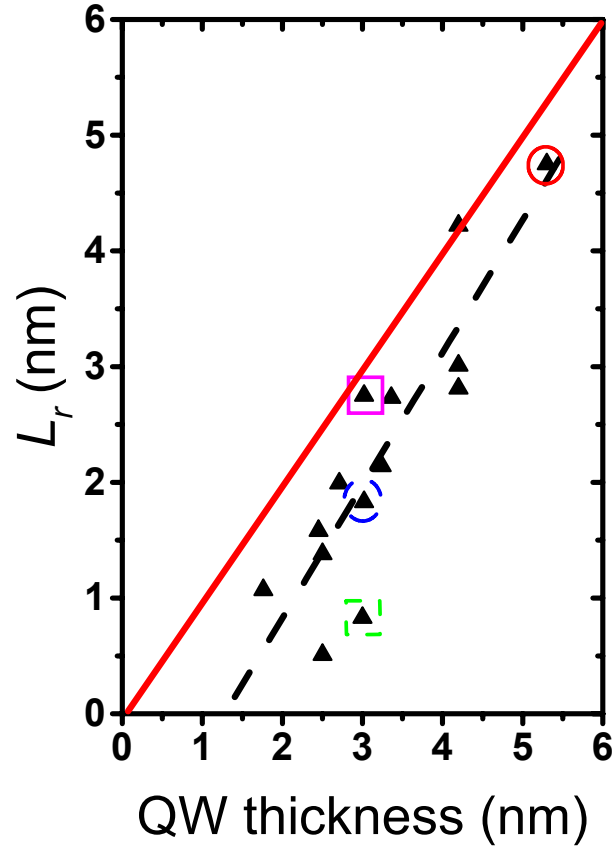
Figure 8: Effective carrier separation, L_r, modified by an "electromechanical correction factor" (ECF) of 4.0. The dashed line represents a best linear fit of the data, whereas the solid line represents the $L_r = L_w$. The circle, square, dashed circle, and dashed square mark Sample 3, LumiLeds #2, LumiLeds #3, and the Akasaki sample, respectively.
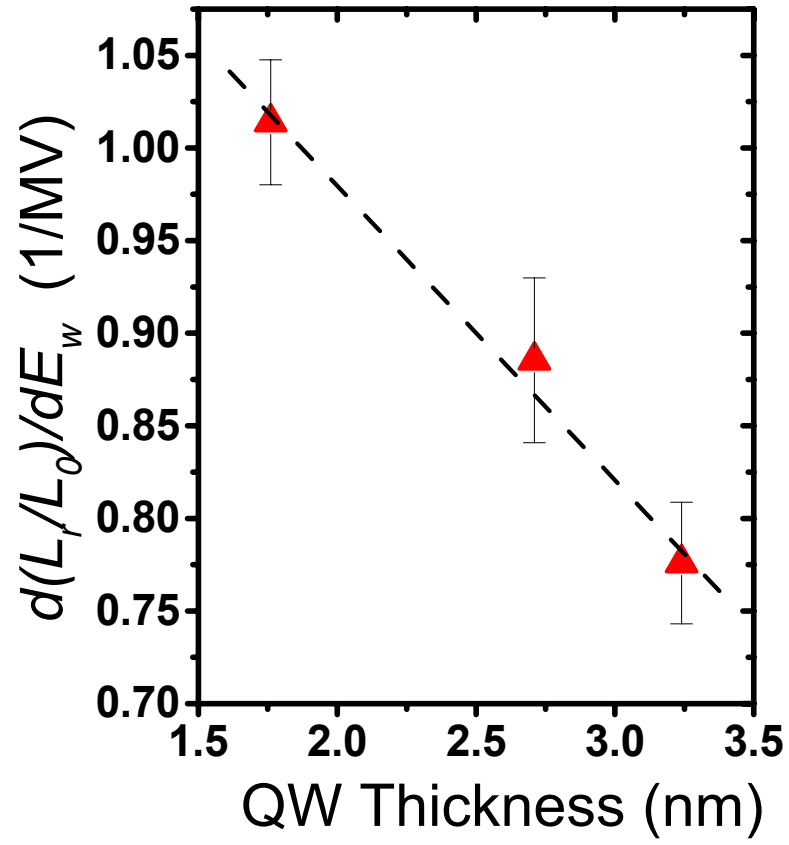
Figure 9: "Polarizability" as a function of the QW thickness for LumiLeds samples 5-7.

6.6 References

[1] O. Mayrock, H.-J. Wunsche, and F. Henneberger, Phys. Rev. B **62**, 16870 (2000).

[2] V. Fiorentini, F. Bernardini, F. D. Sala, A. D. Carlo, and P. Lugli, Phys. Rev. B **60**, 8849 (1999).

[3] L.-W. Wang, Phys. Rev. B. **63**, 245107 (2001).

[4] F. Bernardini, and V. Fiorentini, Phys. Rev. B **64**, 085207 (2001)

[5] V. Fiorentini, F. Bernardini, and O. Ambacher, Appl. Phys. Lett. **80**, 1024 (2002)

[6] G. Vaschenko, D. Patel, C. S. Menoni, N. F. Gardner, J. Sum, W. Goetz, C. N. Tome, and B. Clausen, Phys. Rev. B **64**, 241308 (2001).

[7] K. Shimada, T. Sota, K. Suzuki, and H. Okumura, Jpn. J. Appl. Phys. **37**, L1421 (1998).

[8] P. Waltereit, M. D. Craven, S. P. DenBaars, and J. S. Speck, to be published.

[9] V. Yu. Davydov, A. A. Klochikhin, R. P. Seisyan and V. V. Emtsev, et. al., Phys. Stat. Sol. (**b**), **229**, R1 (2002)

[10] J. Wu, W. Walukiewicz, K.M. Yu, J.W. Ager III, E.E. Haller, Hai Lu, William J. Schaff, Yoshiki Saito and Yasushi Nanishi, Appl. Phys. Lett., ID 015222APL, in press.

[11] T. Mukai, M. Yamada, and S. Nakamura, Jpn. J. Appl. Phys. **38**, 3976 (1999).

[12] A. Hangleiter, J. Seo Im, H. Kollmer, S. Heppel, J. Off, Ferdinand Scholz, MRS Internet J. Nitride Semicond. Res. **3**, 15 (1998).

[13] E. Berkowicz, D. Gershoni, G. Bahir, E. Lakin, D. Shilo, E. Zolotoyabko, A. C. Abare, S. P. Denbaars, and L. A. Coldren, Phys. Rev. B **61**, 10994 (2000).

[14] P. Lefebvre, A Morel, M. Gallart, T. Taliercio, J. Allegre, B. Gil, H. Mathew, B. Damilano, N. Grandjean, and J. Massies, Appl. Phys. Lett. **78**, 1252 (2001).

Chapter 7: Conclusions

7.1 Conclusions

In past years, during which the group III-arsenide material system was chiefly used for opto-electronic devices, all that one needed to know in order to predict the radiative transition was the alloy composition and QW thickness. The group III-nitride material system, however, presents significant complications. The low symmetry of the III-nitride crystals allows the presence of polarization fields that induce a spatial separation between the electrons and holes that are involved in the radiative transition. In addition, the poor solubility of InN in GaN can result in an inhomogenous alloy composition that tends to localize the carriers in regions of high indium content. These phenomena can have great impact on the nature of the radiative transition in InGaN QW structures, affecting both the transition energy and the carrier lifetime.

At the onset of this work, it was thought that one transition type (carrier separation vs. carrier localization) would dominate over the other in a given sample. However, as this work progressed, it became apparent that the situation is more complicated. The true radiative transition appears to be some sort of a hybrid of the two proposed models. That is, the presence of the electric field does tend to draw electrons and holes to opposite sides of the QW. However, indium-rich nano-clusters draw the electrons and holes toward energy-gap minima. Thus, the situation is such that the electron and holes are indeed separated to some extent across the QW, but they are localized in the plane of the QW due to the indium inhomogeneities. The extent of the

separation and localization depends on the microstructure of the QW and doping in the active region.

The scale of the inhomogeneity is so small (a few nm) that not many techniques can explore it. In fact, only HR-TEM has been able to get a handle on the nature of these so-called nano-clusters. The presence of the electric field in the QW is even more difficult to measure directly. Discerning the nature of the radiative transition is therefore left to luminescence type experiments, where the luminescence is measured as a function of excitation density, temperature, and strain.

The temperature-dependent studies did reveal inhomogeneity in the luminescence centers but were not able to pinpoint their source (concentration vs. thickness fluctuations). They did however reveal a small decline in radiative efficiency with increasing carrier separation. The excitation-dependent studies did reveal evidence for carrier separation in a specific case but were not able to quantify it. In addition, the usefulness of this technique decreases with increased doping in the active region, since the doping-induced carriers may screen any effect of the externally excited carriers.

The strain-dependent studies also revealed evidence for carrier separation. However, these studies could not be used to quantify the extent of separation, and they were not hindered by the presence of doping-induced carriers. These studies revealed that the carrier separation increases with increasing QW thickness but decreases with increasing indium content and heavy doping in the active region. The decrease of carrier separation with indium content is probably due to increased indium segregation and interface broadening. The decrease with heavy doping is probably due to carrier screening of the electric field. Thus, to avoid the reduced quantum efficiency that is

associated with carrier separation, it is important to design structures with high indium content in the QWs and high doping of the active region.

7.2 Future work

Studying the luminescence as a function of strain yields the most specific information about the carrier separation in a given structure. Thus, it is this method that should be developed and used in future studies. Since there is a level of uncertainty in the magnitude of strain transferred to the epilayer from the substrate, it is necessary to use some calibration technique, such as Raman Spectroscopy, to determine the exact strain applied. Also, it is crucial to establish the true value of the electromechanical constants of InGaN layers in order to get the true value for the electric field-pressure coefficient, and allow a more accurate determination of the effective carrier separation, L_r.

While some systematic studies have been performed as a function of QW thickness and indium content, these studies should be expanded. In particular, the study as a function of indium content should be extended to samples with higher indium content, where phase segregation is expected to become more significant. These should further reduce the effective carrier separation in the QW. In addition, a systematic study of structures with varying degree of doping should be conducted. This will show whether the doping induced carriers screen the electric field and reduce the effective carrier separation. Systematic studies, as a function of growth parameters, such as substrate temperature, should also be carried out. Varying growth parameters may change the indium distribution in the layer, thus changing the carrier separation. Alongside the luminescence studies, HR-TEM characterization is necessary to distinguish between such effects as indium clustering and interface diffusion.

Finally, the theoretical models need to be improved and developed. While in this work the shift of the energy gap was assumed to be the same as that for the bulk material, it is likely that for very thin wells, confinement effects would reduce this shift. This miscalculation could result in an exaggerated value for the effective carrier separation in thinner wells. In addition, instead of calculating the effective carrier separation, it should be possible to calculate the actual wavefunctions of the electrons and holes in this structure. However, this will require a more thorough knowledge of the indium distribution in the QW. The analysis of the lifetime-pressure coefficient is at an especially early stage of development. The carrier "polarizability," when properly understood, may provide insight into the factors that determine the extent of carrier separation in these structures. That is, it may reveal the existence of "barriers," such as potential minima related to indium-rich nano-clusters, hindering the response of electron and hole wavefunctions to the electric field.